

Faculty of Physics and Astronomy

University of Heidelberg

Diploma thesis
in Physics

submitted by
Johannes Albrecht
born in Heidelberg

October 2005

**Calibration of the
Electromagnetic Calorimeter
of the *BABAR* Experiment Using
 $e^+e^- \rightarrow \mu^+\mu^-\gamma$
Data**

*This diploma thesis has been carried out by Johannes Albrecht at the
Physikalisches Institut Heidelberg
under supervision of
Prof. Dr. Ulrich Uwer*

Kurzfassung

Das elektromagnetische Kalorimeter des *BABAR* Detektors war bisher nur bis zu Photonenergien von 1.5 GeV kalibriert. Oberhalb dieser Grenze wurde die Energie von Photonen mit einer Monte Carlo Simulation bestimmt.

In dieser Arbeit werden Streuereignisse des Typs $e^+e^- \rightarrow \mu^+\mu^-\gamma$ benutzt um erstmals eine Kalibration für den hochenergie Bereich des Kalorimeters durchzuführen. Dies ist möglich, da die Energie und Richtung der Photonen vollständig durch die Energie und den Impuls der beiden Muonen bestimmt werden. Die systematischen Unsicherheiten der Kalibration betragen 0.3%. Die Energieauflösung des Kalorimeters wird für den Energiebereich zwischen 2 und 7 GeV bestimmt und mit der Monte Carlo Simulation verglichen.

Erstmals wird mit diesen Photonen ebenfalls die Rekonstruktion der Photonrichtung analysiert. Eine systematische Abweichung der rekonstruierten Photonrichtung von der wahren Richtung von bis zu 4 mrad wird beobachtet. In der Monte Carlo Simulation wird sogar eine noch grössere Abweichung (bis zu 10 mrad) bestimmt. Eine Korrektur der Abweichungen wurde entwickelt und getestet.

Abstract

In the past, the electromagnetic calorimeter of the *BABAR* detector was calibrated only up to photon energies of 1.5 GeV. Above this energy, the energy determination for a photon cluster was using results from a Monte Carlo simulation.

In this thesis, photons from events of the type $e^+e^- \rightarrow \mu^+\mu^-\gamma$ are used to perform a calibration for the first time in the high energy range. This is possible since the energy and direction of these photons is fully determined by the four momenta of the two muons. The systematic uncertainty of the energy scale is estimated to be 0.3%. The energy resolution of the electromagnetic calorimeter is determined in the range between 2 and 7 GeV and compared to the prediction of the Monte Carlo simulation.

In addition, the photons are used to study for the first time the reconstruction of the photon direction. A systematic deviation of the reconstructed photon direction from the estimate of the true direction of up to 4 mrad is found. In the Monte Carlo simulation, an even larger deviation (up to 10 mrad) is observed. A scheme to correct for these deviations is developed and tested.

Contents

1	Introduction	7
2	Theory	9
2.1	Initial and Final State Radiation	9
2.2	Interactions of Particles with Matter	10
2.2.1	Charged Particles	11
2.2.2	Neutral Particles	11
2.2.3	Electromagnetic Showers	13
3	The BaBar Experiment	15
3.1	The PEP-II Collider	15
3.2	The BaBar Detector	16
3.2.1	Silicon Vertex Tracker	16
3.2.2	Drift Chamber	18
3.2.3	Cherenkov Detector	19
3.2.4	Magnet Coil and IFR	20
3.3	The Electromagnetic Calorimeter	20
3.3.1	Purpose and Layout	20
3.3.2	Geometry	21
3.3.3	Reconstruction of Clusters and Bumps	22
3.4	Energy Calibration of the Calorimeter	23
3.4.1	Cluster Calibration	25
4	Event Selection and Kinematic Fit	27
4.1	Data Sample	27
4.1.1	Data Events	27
4.1.2	Simulated Events	28
4.2	Event Selection	28
4.3	Phase Space	29
4.3.1	Phase Space Reweighting	29
4.4	Agreement Between Data and Simulation	32
4.5	Truth Matching in the Simulation	33
4.6	Peak Fit Procedure	34

4.7	Photon Energy Estimate	35
4.7.1	Input Variables	36
4.7.2	Four Vector Estimate	37
4.7.3	Kinematic Fit	38
4.7.4	Fit Quality	39
4.8	Summary	43
5	Photon Energy Measurement	45
5.1	Calorimeter Energy Response	45
5.2	Cluster Energy Calibration	47
5.2.1	Calibration Algorithm	47
5.2.2	Simulation	48
5.2.3	Data	55
5.2.4	Test of the Calibration	59
5.3	Systematic Studies of the Calibration	62
5.3.1	Shape of the Distributions in Data and Simulation	62
5.3.2	Charged Particle Measurement	64
5.3.3	Uncertainty in Beam Spot	65
5.3.4	Peak Fit Procedure	65
5.3.5	Summary of Systematic Uncertainties	66
5.4	Energy Resolution	67
5.5	Summary	69
6	Photon Position Reconstruction	71
6.1	Position Reconstruction Algorithm	71
6.1.1	Position Estimate Using the Kinematic Fit	74
6.2	Position Reconstruction on Module Level	74
6.2.1	Reconstructed Angles in Data and Simulation	74
6.2.2	Position Resolution	76
6.3	Position Measurement Inside Single Crystals	81
6.3.1	Qualitative Discussion	81
6.3.2	Quantitative Discussion	82
6.4	Correction of the Sub-Crystal Deviation	87
6.4.1	Systematic Study Using Fit Information	88
6.4.2	Correction of the Sub Crystal Deviations	93
6.5	Summary	96
7	Calibration with Minimal Ionizing Muons	97
7.1	Single Crystal Calibration	97
7.2	Cluster Calibration with MIPs	101
7.3	Results	103
7.4	Summary	103
8	Conclusion and Outlook	105

<i>CONTENTS</i>	7
A Detailed Selection Criteria	111
B Distributions to Measure the Angular Resolution	113
C χ^2 Distributions	115
D Crystal Light Yield	117

Chapter 1

Introduction

The SLAC B-Factory program, *i.e.* the *BABAR* experiment and the PEP-II collider [1], was designed to explore the full spectrum of physics accessible with B-mesons and τ -leptons. Initially, the emphasis was on the discovery of CP violation [2] in the B-meson system. With the very large integrated luminosity, approximately 300 fb^{-1} up to October 2005, processes with very small cross sections become accessible. This allows over-constrained tests of the Cabbibo-Kobayashi-Maskawa (CKM) Unitarity Triangle [3] and searches for physics beyond the standard model via loop decays.

In a typical B-decay, 5.5 photons are produced on average, mostly originating from neutral pion decays. In order to fully reconstruct the B-decay, the energy and the position of the neutral particles have to be measured. This is done in the electromagnetic calorimeter (EMC) [1]. An expected photon energy spectrum for generic B-decays is shown in Fig. 1.1 (a). In the center-of-mass (c.m.) system, energies of up to 1 GeV are observed.

Some of the rare decays mentioned above involve high energetic photons in the final state. Examples are $B \rightarrow \pi^0\pi^0$ [4], which is needed to determine the angle α of the CKM Unitarity Triangle, or the electroweak Penguin decay $b \rightarrow s\gamma$ [5], which is one of the most promising candidates for searches for physics beyond the standard model. The photon energy spectra for both decays are shown in Fig. 1.1 (b) and (c) respectively. Energies of up to 4 GeV in the c.m. frame are expected.

The cesium iodide calorimeter of the *BABAR* detector was designed to detect electromagnetically interacting particles, provide electron identification and information about neutral hadrons. However, the electromagnetic calorimeter is currently not calibrated for energies higher than 1.5 GeV. Above this threshold, the calibration relies on information obtained from Monte Carlo simulations.

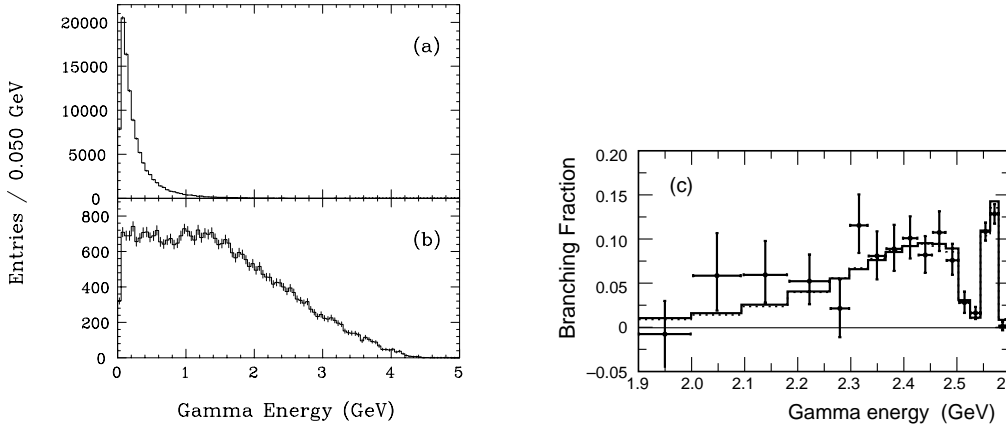


Figure 1.1: Expected *c.m.* photon energy spectra in (a) generic *B*-decays, (b) $B \rightarrow \pi^0\pi^0$ [6], and (c) expected and measured photon energy spectrum of $b \rightarrow s \gamma$ [5]. Energies up to 4 GeV in the *c.m.* frame are expected.

In this thesis, radiative muon pair events of the type

$$e^+e^- \rightarrow \mu^+\mu^-\gamma \quad (1.1)$$

are studied. In those events, the photon energy can be calculated from the muon measurements, *i.e.* without any information from the calorimeter. This photon estimate is used to calibrate the energy and position measurement of the calorimeter and to study the resolution of the energy and position measurement. Finally, the minimum ionizing signal of muons can be used to analyze and calibrate the EMC.

In the first part of this thesis, a cluster energy calibration for high energies is presented using radiative muon pairs. It is possible to calibrate the calorimeter with these events for energies between 400 MeV and 7 GeV. This calibration can be combined with the existing low energy calibration of the *BABAR* EMC which is performed with decays of neutral pions into two photons for energies between 70 MeV and 1.5 GeV.

The resolution of the reconstructed π^0 invariant mass is dominated by the photon energy resolution for low photon energies ($E_\gamma \lesssim 0.7$ GeV) and by the angular resolution for higher energies ($E_\gamma \gtrsim 0.7$ GeV). The π^0 energy calibration assumes a correct angular measurement of the photons. Therefore, the angular reconstruction for photons is discussed in the second part of this thesis.

Chapter 2

Theory

In this thesis, hard photons radiated in the initial or final state are used to calibrate the calorimeter. The process $e^+e^- \rightarrow \mu^+\mu^-\gamma$ can be calculated to a high precision in QED. After presenting the cross section and radiation probability of these photons, the basic mechanisms of energy deposition of charged and neutral particles is discussed.

2.1 Initial and Final State Radiation

In principle, two different processes contribute in first order to the radiation of hard photons in the data sample $e^+e^- \rightarrow \mu^+\mu^-\gamma$. The photon can be radiated in the initial state (ISR) by the beam electron or positron or it can be radiated in the final state (FSR) by one of the muons. The Feynman graphs for both processes are shown in Fig. 2.1.

Experimentally, both processes can not be distinguished. Theoretically, they are different since the muon mass is approximately 200 times the electron mass. However, for hard radiated photons at a collider with an energy of 10.58 GeV

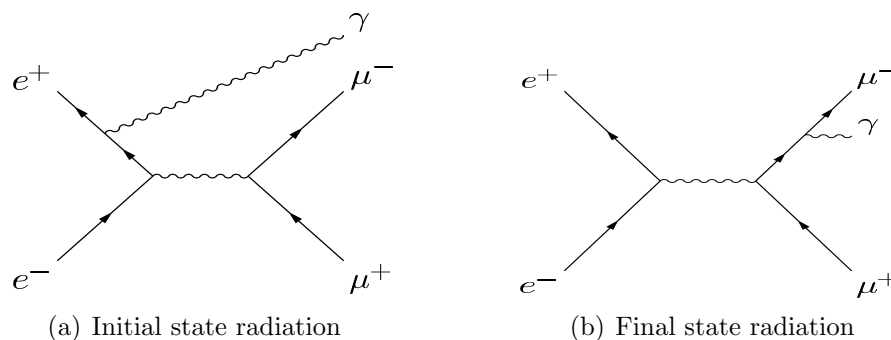


Figure 2.1: Feynman diagram for the radiation of a photon in the initial or final state.

in the c.m. system, lepton masses can be neglected. Thus, ISR and FSR have identical cross sections. The calculation of the cross section will be performed for ISR photons.

Hard initial state photons are radiated at all angles to the collision axis. The ISR cross section $\sigma(s)$, is obtained to first order as

$$\frac{d\sigma(s, x, \theta)}{dx} = W(s, x, \theta) \cdot \sigma_{e^+e^- \rightarrow \mu^+\mu^-}(s(1-x)), \quad (2.1)$$

where $x = 2E_\gamma/\sqrt{s}$, E_γ is the c.m. energy of the photon and \sqrt{s} is the total c.m. energy. The probability of photon emission is described by the function $W(s, x, \theta)$, which in first order is

$$W(s, x, \theta) = \frac{\alpha}{\pi x} \left(\frac{2 - 2x - x^2}{\sin^2\theta} - \frac{x^2}{2} \right), \quad (2.2)$$

where α is the fine structure constant and θ the ISR photon emission angle in the c.m. system [7]. The first order calculation of $W(s, x, \theta)$ has an infrared divergency assuming massless fermions. It is valid for $\theta \gg 0$. More precise equations taking next order processes into account are free from divergencies. They can be found in [8].

ISR photons are emitted predominantly at small angles relative to the beam axis. About 10% of the photons have c.m. polar angles in the range of the acceptance of the *BABAR* detector.

The cross section of $e^+e^- \rightarrow \mu^+\mu^-$ is given by

$$\sigma_{e^+e^- \rightarrow \mu^+\mu^-}(s) = \frac{4\pi\alpha^2}{3s}. \quad (2.3)$$

This cross section is only valid at energies where lepton masses are negligible. Numerically, the cross section of $e^+e^- \rightarrow \mu^+\mu^-$ is 86.8 nb/s (GeV^2). If the muon mass cannot be neglected, a helicity correction has to be applied. However, it lies between 0.95 and 1.0 for $s > 10 m_\mu^2$ [9].

The first order calculations presented here for cross section and radiation probability show an infrared divergency for the photon and a divergency to small photon angles.

2.2 Interactions of Particles with Matter

In this section, the interactions of charged and neutral particles with matter are discussed. As events of the type $e^+e^- \rightarrow \mu^+\mu^-\gamma$ are studied in this thesis, the section on energy deposition of charged particles will focus on muons and the section on interaction of neutral particles will focus on photons.

2.2.1 Charged Particles

Except for highly relativistic particles (for muons well above energies of 10 GeV), the main contribution to energy loss in matter are ionization and atomic excitation. The Bethe-Bloch formula [10] gives the average energy loss as

$$-\frac{dE}{dx} = 4\pi \frac{z^2 \alpha^2}{\beta^2} \frac{Z\rho}{Am_N m_e} \left(\frac{1}{2} \ln \frac{2m_e \beta^2 \gamma^2 T_{max}}{I^2} - \beta^2 - \frac{\delta}{2} \right), \quad (2.4)$$

where m_e , m_N , α are the electron and nucleon masses and the fine structure constant. The incoming particle properties are the charge z , the velocity β and the gamma factor γ . Z , A , ρ and I are the charge and atomic number of the atoms of the medium, the density and average ionization potential for the medium. The factor δ denotes the density effect. It is a correction due to medium polarization. T_{max} denotes the maximal energy transfer in a single collision. For an incident particle of mass M , and momentum $M\beta\gamma c$, kinematics give

$$T_{max} = \frac{2m_e c^2 \beta^2 \gamma^2}{1 + 2\gamma m_e/M + (m_e/M)^2}. \quad (2.5)$$

The ionization energy loss decreases with $1/\beta^2$ for increasing velocities until it reaches a minimum for $\beta\gamma \sim 4$. The particle is then called *minimum ionizing*. Afterwards, it starts to rise logarithmically until it reaches a constant value (*Fermi plateau*).

Fig. 2.2 shows the energy loss by muons incident on copper over nine orders of magnitude of the muon momentum. In this thesis, muons with an energy of 0.4 to 10 GeV are studied. This corresponds to a dE/dx value near the minimum. The typical value of energy losses by minimum ionizing particles are around 2 MeV/(g/cm²). In the *BABAR* calorimeter which consists of CsI(Tl), this value corresponds to 6.6 MeV/cm or ~ 200 MeV per crystal.

2.2.2 Neutral Particles

The interaction of neutral particles in matter are fundamentally different from the ones of charged particles. The main interactions of photons are discussed in the following.

Photoelectric Effect

The photoelectric effect involves the absorption of a photon by an atomic electron which then gets emitted by the atom. The cross section for this process depends on the energy of the incident photon, it is the largest when the photon energy approaches the binding energies of the atomic electrons. The photoelectric cross section rises with Z^5 (Z being the atomic number of the medium) and is proportional to $1/E^3$.

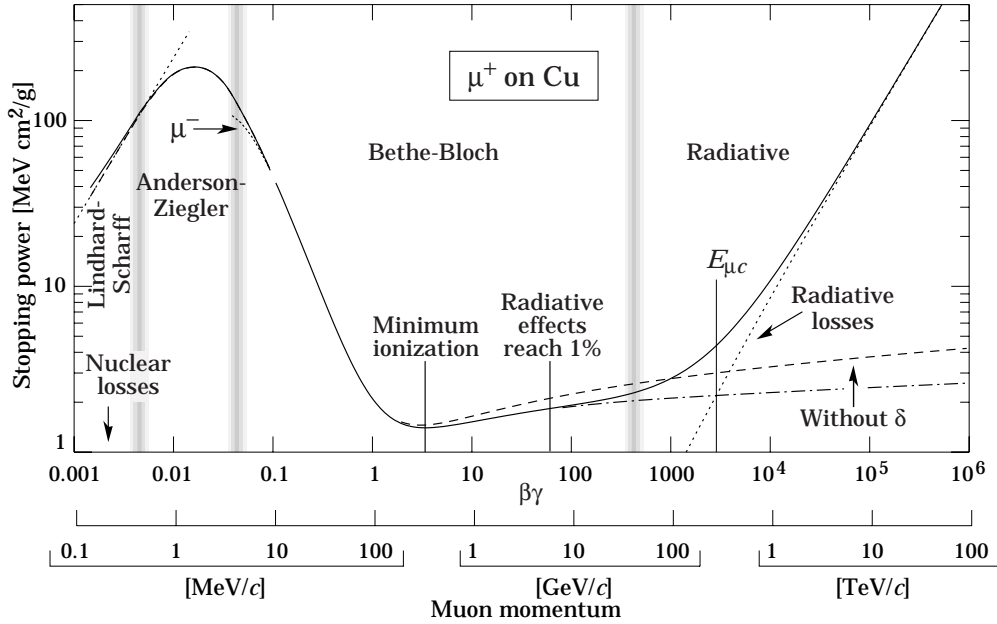


Figure 2.2: Stopping power ($=\langle -dE/dx \rangle$) for positive muons in copper as a function of $\beta\gamma = p/Mc$. Solid curves indicate the total stopping power. Vertical bands indicate the boundaries between different approximations [10].

Compton Scattering

Compton scattering is the scattering of photons on free electrons. As the binding energy of electrons is small compared to that of passing near relativistic particles, this process is relevant in most particle detectors. The cross section of Compton scattering is proportional to $1/E$. Closely related to the Compton scattering are the Rayleigh scattering which can be neglected at high energies.

Pair Production

The process of pair production involves the transformation of a photon into an electron positron pair. In order to conserve momentum, the presence of a nucleus as third body is necessary. Theoretically, pair production is connected to bremsstrahlung by a simple substitution rule.

Pair production is the dominant interaction process for high energy photons (above roughly 10 MeV). The characteristic amount of material traversed is called a radiation length X_0 . It is defined as $\frac{7}{9}$ of the mean free path for pair production by a high energetic photon. This definition is due to the close connection to bremsstrahlung: The radiation length X_0 is as well defined for an electron of energy E as $-(dE/dx)_{brems} = E / X_0$.

2.2.3 Electromagnetic Showers

A high energetic photon in matter initiates an electromagnetic cascade as pair production and bremsstrahlung generate more electrons and photons at lower energies. Fig. 2.3 shows a schematic view of an electromagnetic shower.

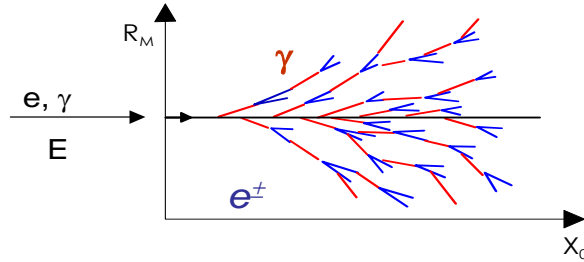


Figure 2.3: Schematic view of an electromagnetic shower. The Electrons are marked with blue lines, the photons in red [11].

Secondary particles produced in the electromagnetic processes are again mainly e^+ , e^- and γ and most of the energy is consumed in particle production. The cascade develops through repeated similar interactions. The maximum number of particles, the shower maximum, is reached when the average energy per particle becomes low enough to stop further multiplication. From this point, the shower decays slowly through ionization losses for electrons or Compton scattering for photons. This change is characterized by the critical energy ϵ in the absorber material. ϵ is the electron energy for which the energy loss by radiation equals the collision and ionization losses. It can be approximated as

$$\epsilon \approx 550 \text{ MeV}/Z , \quad (2.6)$$

where Z is the atomic number of the medium.

The electromagnetic shower, to a good approximation, scales longitudinally with the radiation length and laterally with the Moliere radius. The Moliere radius is parameterized as

$$R_M = 0.0265 X_0 (Z + 1.2) . \quad (2.7)$$

A cylinder with radius $3R_M$ contains 99% of the energy of a shower. Experimental results on the shower shape have been parameterized in the following way [12]: The shower maximum is given as

$$t_{max} \approx \log(E/\epsilon) - a \quad [\text{in units of } X_0], \quad (2.8)$$

where E is the energy of the incident particle and $a = 1.0$ for e^+ and e^- and $a = 0.5$ for photons. The shower depth for 95% containment is

$$t_{95\%} \approx t_{max} + 0.08Z + 9.6 , \quad (2.9)$$

where $t_{95\%}$ is given in units of the radiation length. The numerical values for the quantities discussed for the *BABAR* CsI(Tl) calorimeter are given in table 2.1. The crystals of the calorimeter are 16 - 17.5 X_0 long. It is seen that the shower maximum is for all energies in the first half of the crystal. The distance with 95% of the shower energy included is always outside the crystals.

Quantity	Value
X_0	1.85 cm
R_M	3.8 cm
ϵ	6.71 MeV
$t_{max}(0.4 \text{ GeV})$	3.6 X_0
$t_{95\%}(0.4 \text{ GeV})$	19.8 X_0
$t_{max}(1 \text{ GeV})$	4.5 X_0
$t_{95\%}(1 \text{ GeV})$	20.7 X_0
$t_{max}(7 \text{ GeV})$	6.5 X_0
$t_{95\%}(7 \text{ GeV})$	22.7 X_0

Table 2.1: *Characteristic quantities for electromagnetic showers for the BABAR calorimeter as discussed in the text. The values are evaluated at typical energies occurring in this thesis.*

Chapter 3

The BaBar Experiment

The primary goal of the *BaBar* detector is the precise measurement of CP violation, but the multi functional design of the detector allows a large number of measurement in the B-meson and in related systems.

The accelerator PEP-II [1], described in the first section of this chapter, is asymmetric e^+e^- collider operating at the $\Upsilon(4S)$ resonance. Together with the *BaBar* detector, described in the second part of this chapter, it is called a *B-meson factory* since the $\Upsilon(4S)$ decays to more than 96% into B-mesons. The electromagnetic calorimeter, which is studied in this thesis, is described in the third section of this chapter.

The experimental facilities are located within the Stanford Linear Accelerator Center (SLAC) at Menlo Park near San Francisco, CA, USA.

3.1 The PEP-II Collider

The PEP-II collider operates at energies of 10.58 GeV in the center-of-momentum (c.m.) frame. These energies lie within the $\Upsilon(4S)$ resonance.

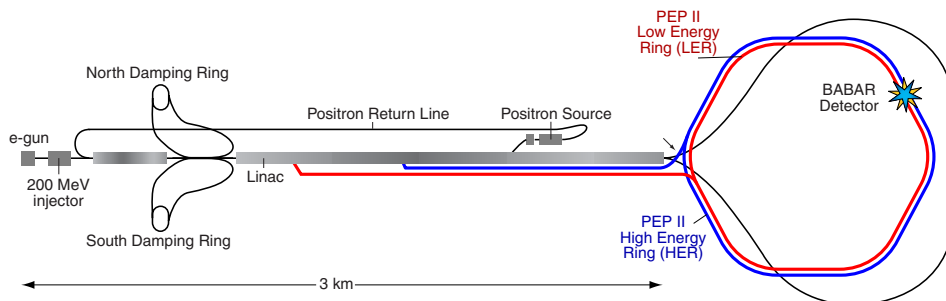


Figure 3.1: *Linear accelerator and PEP-II storage ring. The BaBar detector is located in the upper right of the storage ring.*

The main feature of PEP-II compared to other e^+e^- colliders is the asymmetry. Electrons are accelerated in the *High Energy Ring* (HER) to energies of ~ 9 GeV, positrons in the *Low Energy Ring* (LER) to energies of ~ 3.1 GeV. This results in a c.m. system with a boost of $\beta\gamma=0.56$. This boost is important for the measurement of time dependent CP violation [4].

Fig. 3.1 shows a schematic view of the facility. The typical branching ratios are of the order of 10^{-4} to 10^{-6} . Thus, the collider needs to provide a very high luminosity. Up to October 2005, an integrated luminosity of about 300 fb^{-1} of data was taken.

The bunches collide head-on at the interaction point (IP). For each machine run, the event vertices are averaged to determine the averaged beam position, the *beam spot*. The uncertainties in the *beam spot* are of the order of a few μm in the transverse plane and $100 \mu\text{m}$ along the collision axis.

3.2 The BaBar Detector

A short description of the *BABAR* detector is given. A more detailed discussion of the detector and its components can be found in [1].

Fig. 3.2 shows a longitudinal view of the *BABAR* detector. The detector is designed according to the boosted c.m. system. The interaction point is not at the geometrical center of the detector. It is shifted towards the backward direction which is defined by the outgoing low energy beam (left hand side in Fig. 3.2).

The components of the *BABAR* detector are arranged radially. The tracking consists of a silicon vertex detector (SVT) and a drift chamber (DCH). The SVT is located close to the beam pipe surrounded by the second tracking device, the DCH. The next component is the Detector of Internally Reflected Cherenkov Light (DIRC) which is mainly used to identify pions and kaons. Its photon detection system is located at the backward end of the BaBar detector. The Electromagnetic Calorimeter (EMC) is a crystal calorimeter with a forward end-cap. It is the last sub-detector within the super-conducting magnet coil which provides a 1.5 T magnetic field. The Instrumented Flux Return (IFR) is the outermost component.

3.2.1 Silicon Vertex Tracker

The silicon vertex tracker (SVT), as shown in Fig. 3.3, is a part of the tracking devices of the detector. It is built from cylindrical layers of double sided silicon micro strip detectors.

The SVT covers the polar angle region from 20° to 150° . The three inner layers are critical for the measurement of the secondary vertices for the B-meson decays. The two outer layers are important for the pattern recognition and the low p_t tracking. The arrangement of the strip sensors along the beam direction as

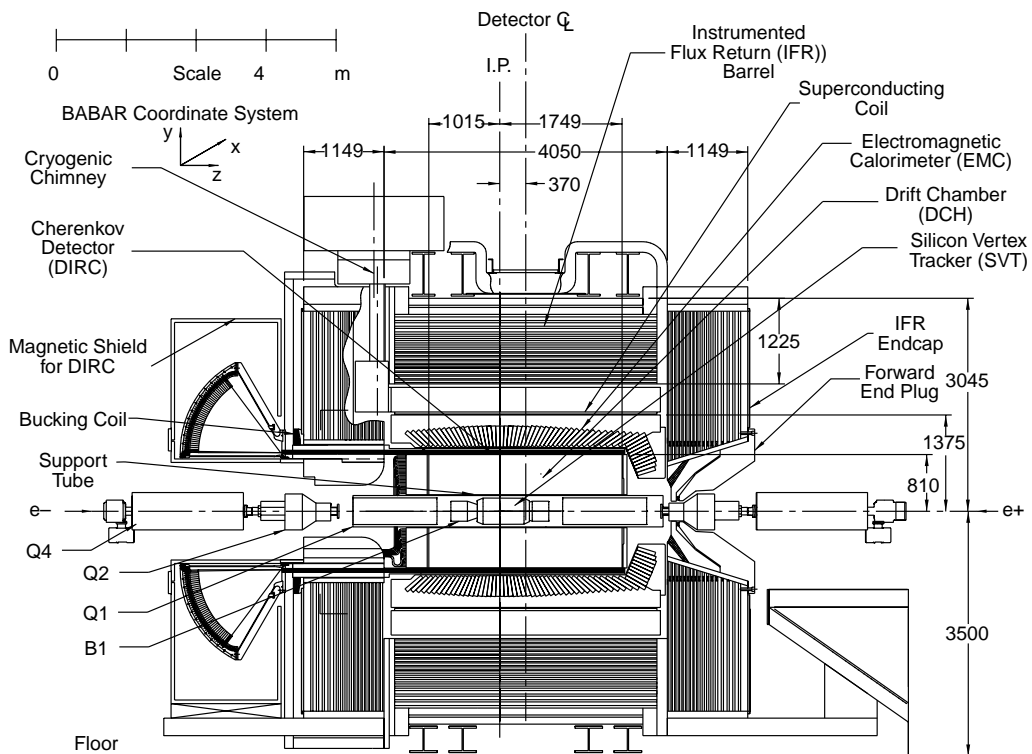


Figure 3.2: Schematic view of the longitudinal axis of the BABAR detector. The 9 GeV electron beam enters from the left, the 3.1 GeV positron beam from the right.

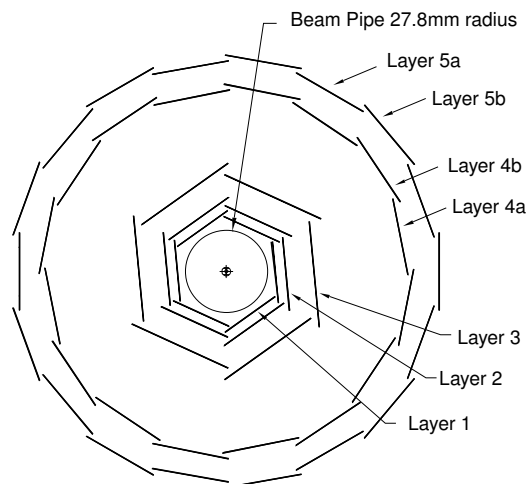


Figure 3.3: Front view of the silicon vertex tracker. The six-fold symmetry of the three inner layers is seen.

well as perpendicular to it allows the spatial measurement of the track directions and angles with a high resolution.

The SVT is especially optimized for excellent vertex resolution and reaches a precision of approximately $70 \mu\text{m}$ for a fully reconstructed B-meson decay.

3.2.2 Drift Chamber

The drift chamber (DCH) measures the tracks of charged particles and their momenta. Additionally, the specific energy loss by ionization can be determined and contributes up to momenta of $700 \text{ MeV}/c$ to the particle identification. A side view is shown in Fig. 3.4.

The DCH is a multi-wire chamber with an inner radius of 26.6 cm and an outer radius of 80.9 cm . Its length is 280 cm . The DCH is composed of 40 layers with small hexagonal cells. In 24 of the layers, the wires are placed at small angles with respect to the z-axis. This provides longitudinal position information. The $20 \mu\text{m}$ -thick sense wires consist of gold plated tungsten-rhenium. The drift gas is a mixture of helium and iso-butane in a ratio of $80 : 20$.

The reconstruction of tracks is done with a Kalman filter which considers data from the SVT and the DCH as well as the detector material and magnetic field. The precision reached in momentum reconstruction is

$$\sigma(p_t/p_t) = (0.13 \pm 0.001)\% + (0.45 \pm 0.003)\%, \quad (3.1)$$

where p_t is the transverse momentum. The average resolution for single tracks is given as $125 \mu\text{m}$.

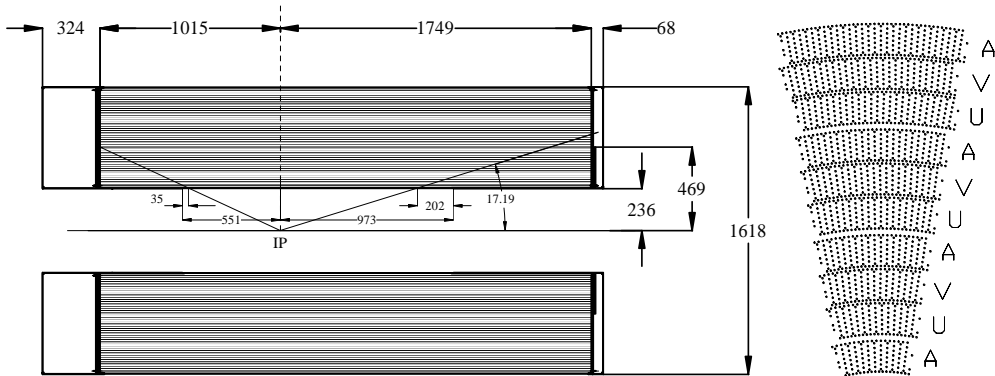


Figure 3.4: Schematic view of the drift chamber. The center of the chamber has an offset of 370 mm from the IP. The pattern of axial (A) and stereo (U,V) layers is shown in the right hand side.

3.2.3 Cherenkov Detector

The detector for internally reflected Cherenkov light (DIRC), shown in Fig. 3.5 is the most important particle identification device of the *BABAR* detector. It is used to separate pions and kaons from B-meson decays. The π/K separation is possible up to momenta of 4 GeV with a significance of 2.5σ .

The active detector material of the DIRC is constructed of 144 bars of fused silica arranged in bar boxes in a polygonal barrel. The DIRC bars are used both as radiators and as light pipes (see left hand side of Fig. 3.5). Charged particles which traverse the DIRC-bars emit Cherenkov light in the angle θ_C with respect to the direction of the particle track,

$$\cos\theta_C = \frac{1}{\beta n} = \frac{\sqrt{1 + (m/p)^2}}{n}, \quad (3.2)$$

where m and p are mass and momentum of the particle respectively. $n=1.453$ is the refractive index of the synthetic quartz medium. The photons are reflected many times until they reach the *stand off box*, a tank of purified water. 10572 photo-multiplier-tubes (PMT) cover the inside of the surface of the standoff box, where fractions of the Cherenkov rings are projected. They are shown for simulated events in the right hand side of Fig. 3.5. A number of discrete ambiguities is introduced through this system, whereas amount of material in-front of the calorimeter is minimized (to about $0.2X_0$ for the DIRC). The ambiguities can be resolved with additional information of the photon arrival time and sophisticated pattern recognition algorithms.

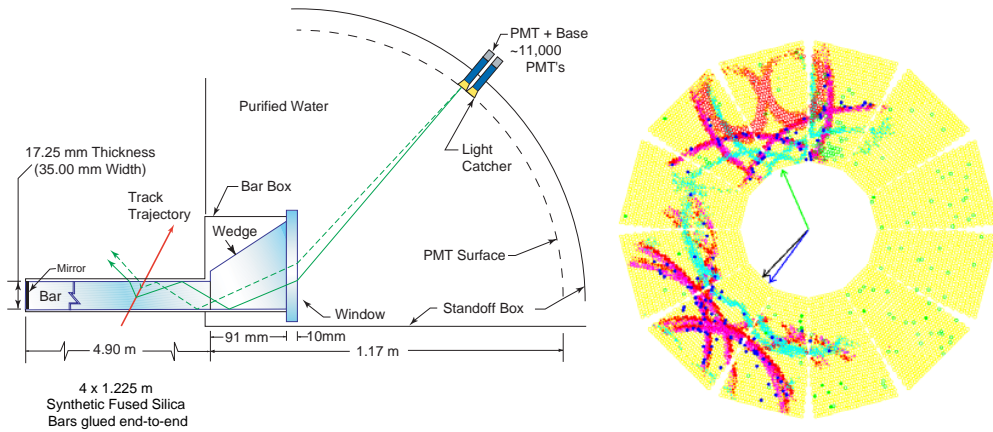


Figure 3.5: *Left hand side: Working principle of the DIRC. The Cherenkov light is internally reflected until it gets detected in the water-filled readout reservoir. Right hand side: Fractions of Cherenkov rings as registered by the PMT.*

3.2.4 Magnet Coil and IFR

All sub detector components are inside a toroidal super conducting magnet coil to allow momentum measurement from track curvature. The *BABAR* magnet creates a 1.5 T magnetic field parallel to the beam axis.

Outside the solenoid is the instrumented flux return (ISR). It consists of three major parts, the barrel sector and forward and backward enddoors. At the barrel region, 21 active resistive plate chambers (RPC) are installed, 18 in the enddoors. The IFR is designed to identify muons and neutral hadrons, *e.g.* K_L^0 .

3.3 The Electromagnetic Calorimeter

3.3.1 Purpose and Layout

The electromagnetic calorimeter (EMC) is designed to measure the energy, the position and the transverse shape of showers with excellent efficiency. It is designed to detect electrons and photons over the energy range of 20 MeV to 9 GeV with high resolution. This allows the detection of photons from π^0 and η decays as well as from QED and radiative processes. Besides that, the EMC contributes via E/p measurements to the electron identification for flavor tagging of neutral B-mesons and via the shower shape analysis to the identification of neutral hadrons. Furthermore, the EMC has to be compatible with the 1.5 T field of the solenoid and operate reliably over the anticipated 10-year lifetime of the experiment.

To achieve these goals, a hermetic, total absorption calorimeter composed of thallium doped cesium iodite crystals (CsI(Tl)) was chosen. The main advantages are a very high light yield and good radiation hardness. This permits the use of silicon photodiodes which operate reliably in magnetic fields for the read-out of the scintillation light. Another advantage of CsI(Tl) crystals is the small Moliere Radius ($R_M = 3.8$ cm) and the short radiation length ($X_0 = 1.85$ cm) which allows a compact detector design for the measurement of fully contained showers.

The energy resolution of a calorimeter as a function of energy can be parameterized to consist of two parts which are added quadratically: A constant part to which electronics nonlinearities and non-uniformities are contributing as well as calibration errors. The second, energy dependent part has a statistical nature since the basic processes in an electromagnetic shower are statistical processes as fluctuations in photon statistics, electronic noise and beam generated background. In crystal calorimeters, the energy dependent part of the resolution is assumed to be proportional to $1/\sqrt[4]{E}$ due to photon statistics [31]. The target energy resolution of the *BABAR* EMC was

$$\frac{\sigma_E}{E} = \frac{1\%}{\sqrt[4]{E(\text{GeV})}} \oplus 1.2\% \quad (3.3)$$

where both terms are added in quadrature.

The angular resolution is determined by the transverse crystal size and the average distance to the interaction point. The target was to achieve

$$\sigma_\theta = \sigma_\phi = \left(\frac{3}{\sqrt{E(\text{GeV})}} + 2 \right) \text{ mrad} \quad (3.4)$$

at 90° incident angle to the beam direction.

3.3.2 Geometry

The EMC consists of a cylindrical barrel and a conical forward endcap. It has full coverage in azimuth and extends in polar angle from 15.8° to 141.8° corresponding to a solid angle coverage of 90% in the c.m. system. The barrel part consists of 5760 crystals which are ordered cylindrical around the beam axis. The radial distance from the interaction point to the crystal front face is 92 cm. Along the polar angle, the barrel is divided in 48 crystal rings. A longitudinal view along the polar angle is shown in Fig. 3.6. Along the azimuthal angle, 120 crystals are segmented. Each crystal is wrapped in an aluminum and a mylar foil. Thus, between two crystals is about 130 μm of dead material. The crystals are ordered into *modules* of $7 \cdot 3$ ($\theta \cdot \phi$) crystals. Those modules are wrapped with carbon fiber tubes, in-between two modules is on average 1.3 mm of material. The modules are bonded to an aluminum strong-back that is mounted on the external support. By supporting the modules at the back, the material in front of the EMC is kept to a minimum. A schematic view of the cylindrical barrel and the assembly of a

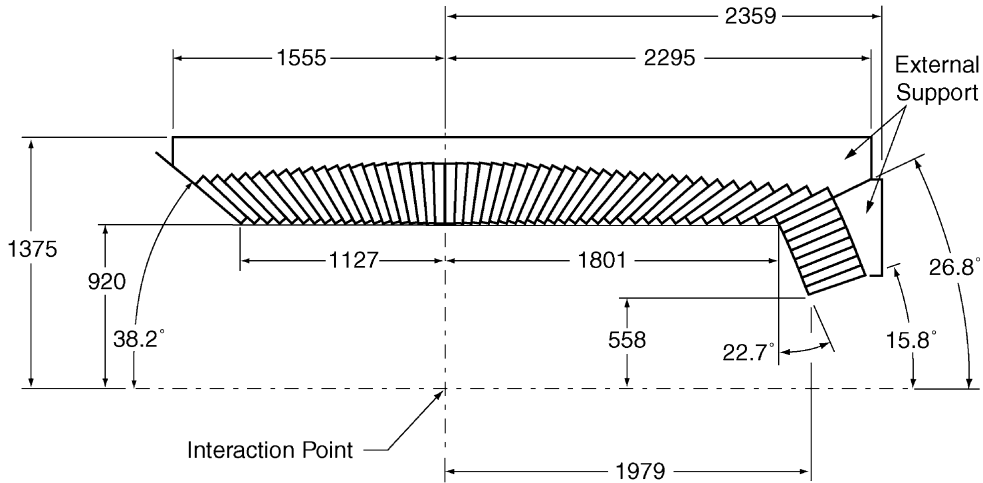


Figure 3.6: Longitudinal view of the calorimeter. Only the top half is shown. The numbering of the crystals goes from $I_\theta=1$ (in the very right) to $I_\theta=56$ in the left end of the EMC.

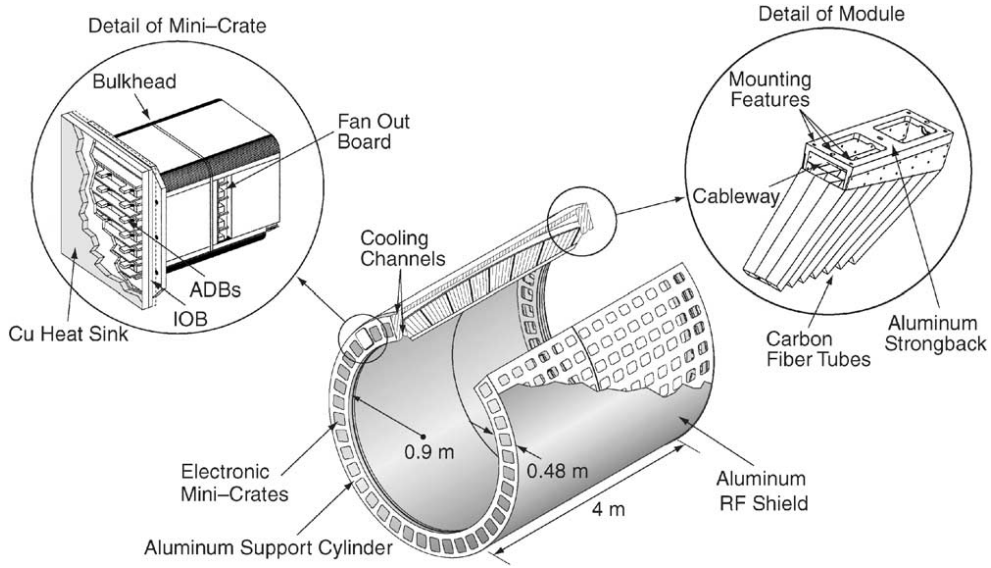


Figure 3.7: *The cylindrical barrel part of the EMC is shown. In the upper right, a module with $3 \cdot 7$ crystals is shown.*

module is shown in Fig. 3.7.

The endcap covers the forward area of the calorimeter. It consists of 820 crystals which are ordered circularly. The eight rings in the polar angle consist of 80 (the innermost two rings), 100 (the next three rings) and 120 (outer three rings) crystals respectively.

All crystals point with their front face to the interaction point. In order to minimize losses in-between the crystals, a small non-projectivity is added in the polar angle. The average size of this non-projectivity is 1.4 mrad.

The crystals are numbered with an index I_θ which in the polar angle,

$$1 \leq I_\theta \leq 56 \quad (3.5)$$

where $I_\theta = 1$ is the very forward part of the endcap, the barrel part begins with $I_\theta = 9$ and the very backward part of the barrel is $I_\theta = 56$. In the azimuthal angle,

$$0 \leq I_\phi \leq 79/99/119 \text{ depending on } I_\theta. \quad (3.6)$$

The material in-front of the EMC was minimized, depending on the polar angle $0.3 - 0.6X_0$ of dead material are between the interaction point and the EMC. In front of the first 3 rings in the endcap are about $3X_0$ of support structure.

3.3.3 Reconstruction of Clusters and Bumps

A particle which enters the EMC deposits, in general, energy in several crystals. Such a group of crystals is called a cluster. The following algorithm is used to reconstruct clusters from the information of individual crystals:

1. The crystal with the highest energy of the cluster is called the *seed*. It is required to have more than 5 MeV.
2. All adjacent crystals with energies above 1 MeV are added to the cluster.
3. The neighbors of each crystal with more than 3 MeV are added to the cluster if their energy exceeds 1 MeV
4. The cluster energy is defined as the sum of the energy of all associated crystals. The cluster energy is required to be more than 20 MeV in total for the cluster to be accepted.

If two particles enter the calorimeter close to each other, it is possible that the energy deposition takes place in one cluster with two local maxima. In this case the cluster is splitted according to the weights of its single crystal information into *bumps* with only one maximum each. The energy and the position of the *bump* is associated to one single particle.

3.4 Energy Calibration of the Calorimeter

The calibration of the *BABAR* calorimeter is performed in three steps:

1. Electronics Calibration,
The electronics calibration corrects the pedestal offsets, determines the overall gain and removes non-linearities.
2. Single Crystal Calibration,
In this calibration step, the measured pulse height in a single crystal is assigned to an energy. It also corrects variations in the light yield from crystal to crystal and over time. The time dependence is mainly due to radiation damage.
3. Cluster Calibration.
In the cluster energy calibration, energy losses which are not due to the features of a single crystal are corrected. These energy losses are due to interactions in front of the EMC, leakage behind the EMC and energy loss in dead material in-between the crystals.

The three steps of the energy calibration of the EMC are discussed in more detail in the following:

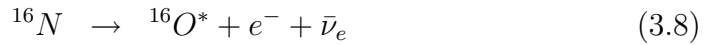
Electronics Calibration

The electronics calibration is performed by precision charge injection into the preamplifier input. Initially up to 12% non-linearity were observed. These non-linearities were traced to oscillations on the ADC cards that have since been corrected. Remaining non-linearities are of the order of 2%.

Single Crystal Calibration

The single crystal calibration is performed for two energies at opposite ends of the dynamic range, the two measurements are combined by a logarithmic interpolation (line calibrator). For low energies, a radiative source spectrum is used ($E_\gamma = 6.13$ MeV) whereas for high energies, electrons from Bhabha scattering are used ($E = 3 - 9$ GeV).

For the radioactive source calibration, irradiated Fluorinert gets pumped through thin walled aluminum pipes which are mounted right in front of the crystals of the EMC. The Fluorinert decays via a radioactive decay chain,



under emission of a monoenergetic photon with the energy of 6.13 MeV. Fig. 3.8 shows a typical source spectrum, the peak at 6.13 MeV and two associated escape peaks are seen [1].

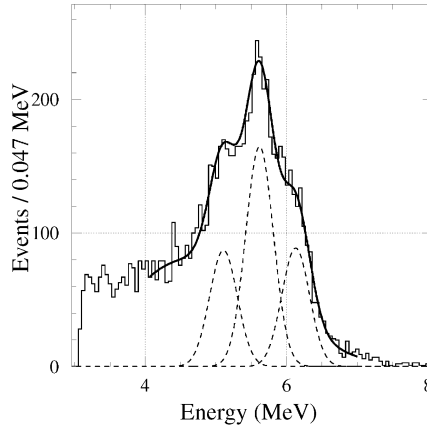


Figure 3.8: *Measured and fitted spectrum of the radioactive source. The dashed lines indicate the primary peak at 6.13 MeV (right hand side) and two escape peaks [1].*

The high energy single crystal calibration factors are determined from electrons from Bhabha scattering,

$$e^+e^- \rightarrow e^+e^-. \quad (3.10)$$

The deposited energy E_{dep}^k of a final state electron k is purely determined by the angle θ_{lab} between e^+ and e^- ,

$$E_{dep}^k(\theta) = \frac{E_{tot}^2 - \vec{P}_{tot}^2}{2(E_{tot} - |P_{tot}|\cos\theta_{lab})} \quad (3.11)$$

where E_{tot} and P_{tot} are the total energy and momentum in the laboratory system, respectively. The energy deposited in each individual crystal is compared to a prediction derived in a Monte Carlo simulation. This means that not only the single crystal calibration factor can be determined, but also slight differences between data and simulation of the crystals are taken out. A more detailed description of the sophisticated algorithm can be found in [32].

The crystal response with electronics calibration and single crystal calibration applied is called e_i . The raw cluster energy, E_{raw} , is defined as the sum of the single crystal calibrated energies e_i ,

$$E_{raw} = \sum_i e_i, \quad (3.12)$$

where i is enumerating all crystals in the respective cluster.

3.4.1 Cluster Calibration

The cluster energy calibration corrects for energy loss due to shower leakage, dead material in front of the calorimeter and in-between the crystals. The true energy of a photon can be expressed as

$$\text{photon energy} = \text{deposited energy} + \text{energy losses}. \quad (3.13)$$

The cluster calibration is obtained as a correction function $c(E, \theta)$ which depends on the polar angle θ and the energy,

$$E_{cal} = E_{raw} \cdot c(E, \theta), \quad (3.14)$$

where E_{cal} is the cluster calibrated energy, E_{raw} the raw energy as defined in Eq. 3.12 and $c(E, \theta)$ is the calibration function.

On Simulation

The processes of energy loss in dead material are included in the simulation. The generated energy describes therefore the single crystal energy e_i . The raw cluster energy is obtained from the generated single crystal energies. In order to have the cluster energy in the simulation at the right scale, the raw energy has to be corrected for these simulated energy losses. This is called *Monte Carlo calibration*. Since E_{true} is known from the generator, $c_{MC}(E, \theta)$ can easily be determined

$$c_{MC}(E, \theta) = \frac{E_{true}^{MC}}{E_{raw}^{MC}}. \quad (3.15)$$

On Data

For data, the situation is more complicated. It is necessary to find a physics process which provides photons with known energies. Currently, the only mechanism which is exploited is the decay $\pi^0 \rightarrow \gamma\gamma$. The reconstructed two photon mass is known to be

$$m_{\gamma\gamma} = \sqrt{2E_{\gamma,1}E_{\gamma,2}(1 - \cos\alpha)} = 135.0\text{MeV} \quad (3.16)$$

where E_γ is the photon energy and α the opening angle between the two photons. This process produces clusters with an energy up to 1.5 GeV in the laboratory frame [21]. At higher energies, the two photons are merged to one cluster and the reconstruction of neutral pions becomes difficult.

For energies above 1.5 GeV, the *BABAR* calorimeter is not calibrated with data from physics processes. Instead, one relies on the Monte Carlo simulation. In this thesis, the process $e^+e^- \rightarrow \mu^+\mu^-\gamma$ will be used to develop a cluster calibration for high energies.

Chapter 4

Event Selection and Kinematic Fit

In this thesis, photons from radiative dimuon events, $e^+e^- \rightarrow \mu^+\mu^-\gamma$, are used to analyze and calibrate the electromagnetic calorimeter of the *BABAR* detector. After a definition of the data sample and the Monte Carlo simulation data used, the selection criteria for a clean event sample are described and the agreement of the simulation with data is studied. Then, two methods to calculate the photon energy without calorimeter information are presented: a four vector calculation and a kinematic fit.

4.1 Data Sample

The data samples used in this thesis are briefly introduced in this section. The data was taken in the years 1999 - 2004 by the *BABAR* detector.

4.1.1 Data Events

In the *BABAR* experiment, data acquisition is separated into machine runs lasting about an hour and into run periods. Typically once a year there is a shutdown of the detector of a few months. A run period is the set of many machine runs without such a shutdown time in-between. The data taking from 1999 to 2004 was separated into 4 run periods, the fifth is currently in progress. During the processing of data, each event is tagged according to its possible physics potential. The events studied in this thesis are required to be classified as events containing dimuons with a high probability. This technique speeds up subsequent physics analyses of certain event topologies. A summary of the event numbers before applying selection criteria is given in table 4.1.

Run Period	Data	Simulation
1	$18 \cdot 10^6$ events	$14.5 \cdot 10^6$ events
2	$61.5 \cdot 10^6$ events	$43.5 \cdot 10^6$ events
3	$29 \cdot 10^6$ events	$10 \cdot 10^6$ events
4	$80 \cdot 10^6$ events	$60 \cdot 10^6$ events

Table 4.1: *Data samples available before selection: For data, the muon preselection is applied and the simulated events are the generated $e^+e^- \rightarrow \mu^+\mu^-\gamma$ events.*

4.1.2 Simulated Events

In this thesis, simulated events from the SP5 and production cycle are used¹. SP5 is the fifth revision of the *BABAR* Monte Carlo simulation using the KK2F event generator [15] and GEANT4 [16] for the detector simulation.

The Monte Carlo simulation takes detector and background conditions (measured during data taking) into account which change over time. This means that for each month of data acquisition roughly the same equivalent luminosity of simulated Monte Carlo events is generated.

4.2 Event Selection

A series of selection criteria are applied to select a clean sample of $e^+e^- \rightarrow \mu^+\mu^-\gamma$ events for data. Details of the criteria can be found in App. A. Additionally to the pre-selection which chooses with high probability events containing muons, the main steps are:

1. Track quality:
All tracks in the data sample are required to fulfill the requirements for a well measured track.
2. Number of tracks:
The number of tracks (as defined above) has to be 2.
3. Muon selection:
One of the two tracks needs to be identified as a muon.
4. Sum of track charges:
The sum of the charges of all tracks (as defined above) has to be 0.

¹The events simulated according to the detector conditions of the fourth run period are produced with SP6 simulation.

5. Radiation angle:

In order to separate the photon from the muon signal, it is required that the angle from the photon to the closest muon is more than 15° .

6. Three particle final state:

To ensure clean three particle dynamics, the system is constrained to contain only one high energetic photon with an energy larger than 50 MeV.

The only high energetic photon left in the data sample is assumed to be the photon radiated in initial or final state radiation.

4.3 Phase Space

The distribution of photons in the energy angular plane is shown in Fig. 4.1 (a) and (b) for simulation and data respectively. Both histograms are normalized to equal area, as all figures which compare data and simulation in this section. The projections to the axes are shown in (c) and (d). The barrel region is marked with a solid line in Fig. 4.1 (c). In the EMC barrel region, the data is reasonably well described by the simulation.

In Fig. 4.1 (d) the energy of the photon is shown. Deviations in the simulation describing the data are seen at energies below 1.5 GeV, at higher energies, the spectrum in data is very well described. Photons up to energies of 7 GeV are used in this thesis.

The distribution of muons in the energy angular plane is shown in Fig. 4.2. As expected from the boost, a correlation between the muon momentum and the polar angle is seen. High energetic muons are emitted predominantly in forward direction (small θ), lower energetic ones in backward direction (large θ).

4.3.1 Phase Space Reweighting

Discrepancies of the muon - photon population in the energy angular plane are seen in Fig. 4.1 and 4.2. Especially for muons, the discrepancy has an influence on the photon energy estimate discussed later. For calibration purposes, the agreement between data and simulation is essential. Possible differences in the muon distribution in the energy angular plane would affect the photon distribution which is used for calibration. To make sure not to depend on such differences, the two-dimensional distribution in the energy angular plane in the simulation is reweighted to the one in data. The reweighting is performed as follows:

1. The phase space is restricted to a common region in data and the simulation. Thus, only muons in the barrel part of the calorimeter (*i.e.* with a polar angle larger than 0.47 rad) and those with energies larger than 400 MeV are studied.

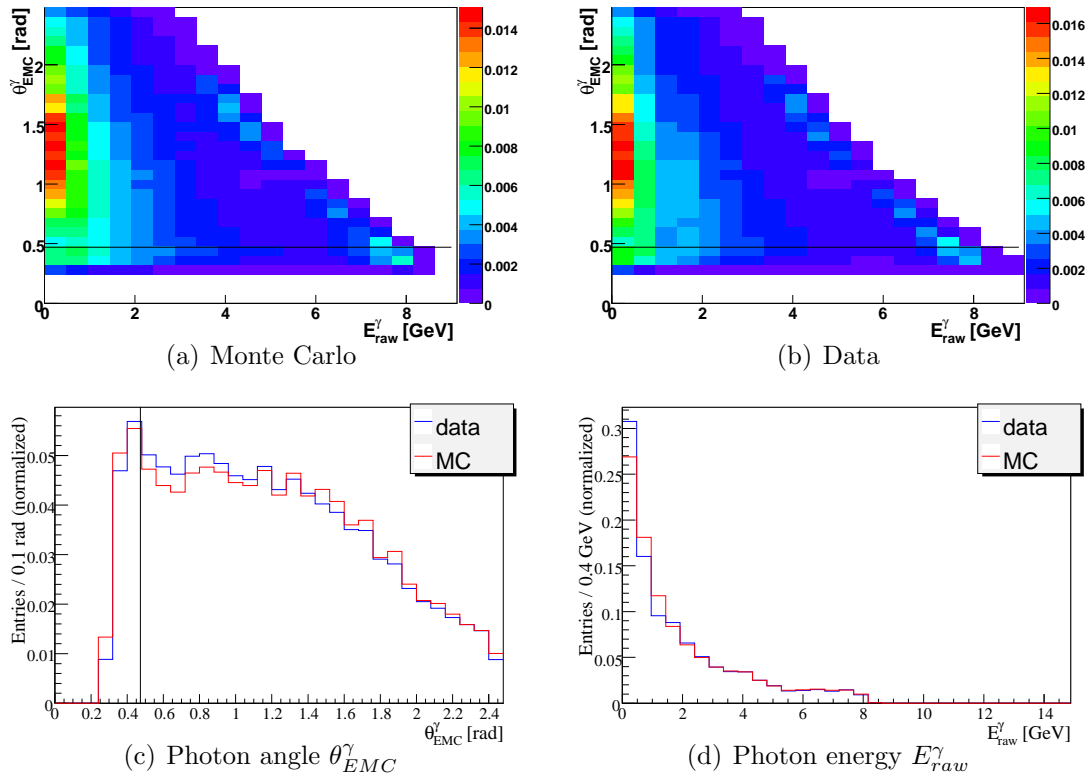


Figure 4.1: *Distribution of the selected photons: Polar angle versus energy for (a) simulation and (b) data. In (c) and (d) projections to the axes are shown.*

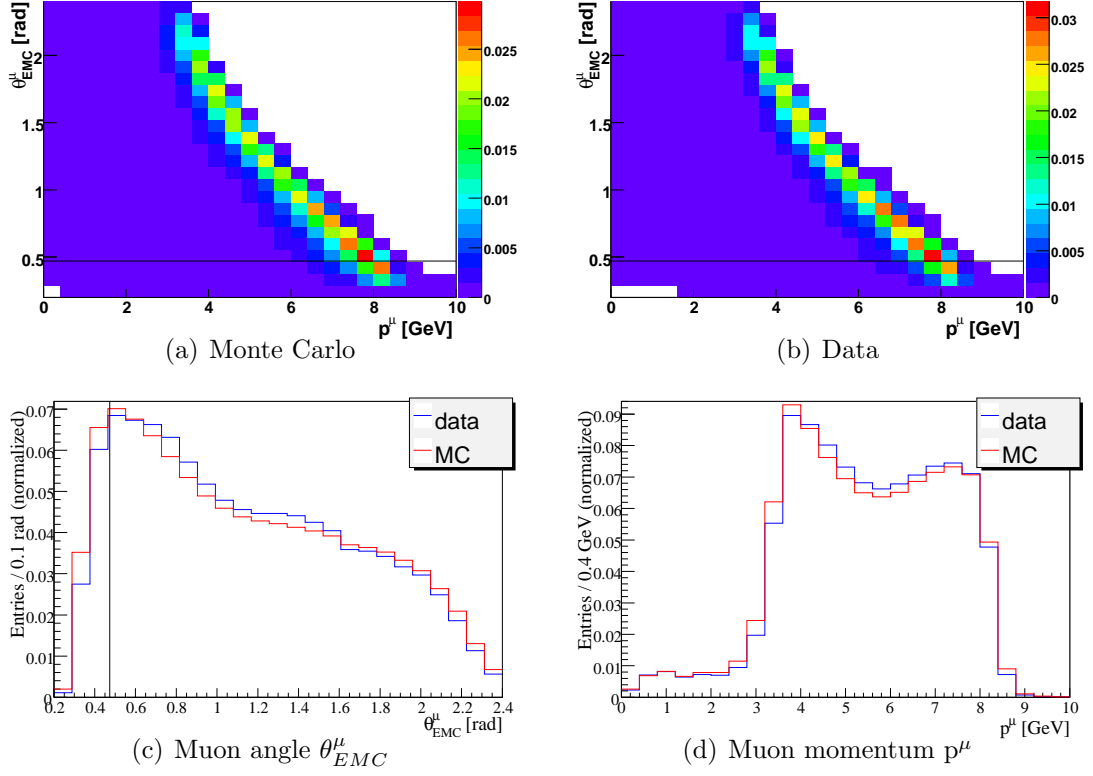


Figure 4.2: Distribution of muons in the energy angular plane for (a) simulation and (b) data. In (c) and (d) projections to the axes are shown.

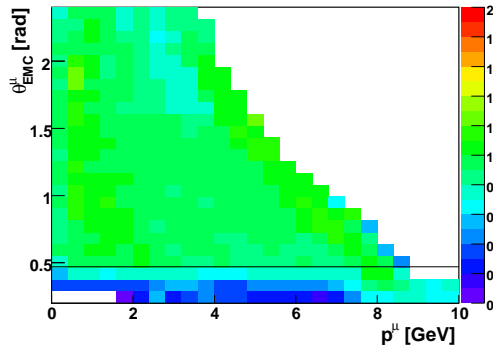


Figure 4.3: Weighting factors for the population of events in the energy angular plane. Only events with both muons in the barrel part of the EMC are used (indicated with a solid line).

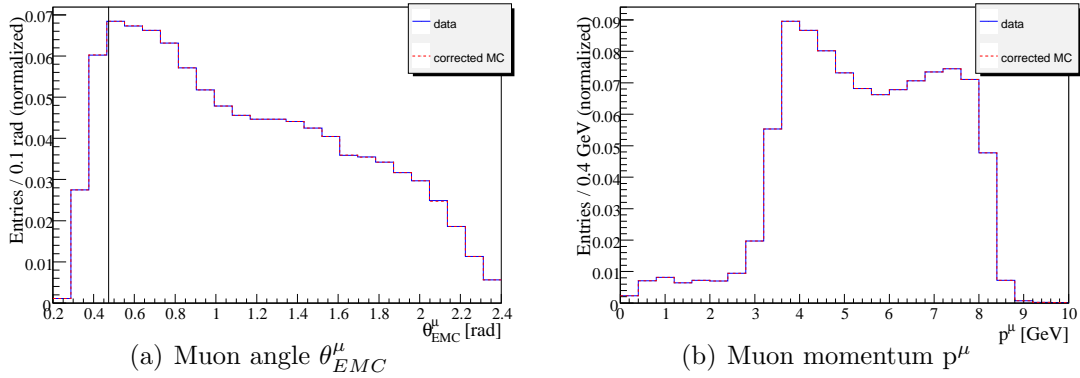


Figure 4.4: Comparison of data and simulation after the reweighting procedure for (a) the polar angle and (b) the momentum. The reweighting works as expected.

2. In the simulation, the population of muons in the energy angular plane in the common region is reweighted two-dimensionally to reproduce the distribution in data. The weighting factors vary between 0.7 and 1.3 per bin, being mostly between 0.9 and 1.1 per bin. They are shown in Fig. 4.3.

As shown in Fig. 4.4, the reweighting works as expected.

4.4 Agreement Between Data and Simulation

The quality of the Monte Carlo simulation describing the data after the reweighting procedure is tested with several distributions. The muon acollinearity is defined in the c.m. system as

$$\text{acollinearity} = \alpha - 180^{\circ} \quad (4.1)$$

where α is the angle between the two muons in the c.m. system. The acollinearity is analyzed since the radiation of a high energetic photon implies a large acollinearity of the muons. It is a test of the quality of the description of the photon radiation in the simulation. The acollinearity is shown in Fig. 4.5 (a). For acollinearities below 0.4 rad, deviations between data and simulation are seen. For acollinearities, the description of the data by the simulation is good.

The noise is studied in Fig. 4.5 (b) and (c). In the simulation, measured noise is mixed into simulated data. The energy spectrum of photons below 50 MeV can be found in Fig. 4.5 (b). The distribution is well described by the simulation, deviations are on the level of 0.2%. The requirement of the cluster finding algorithm (see section 3.3.3) that the total cluster energy is above 20 MeV can be seen. The drop before the cutoff is an artefact of the binning. The simulation describes the distribution well. Deviations are on the order of 10^{-2} to 10^{-4} . The number of photons below the cutoff of 50 MeV is shown in Fig. 4.5 (c). Considering the logarithmic scale, the simulation describes the data reasonably

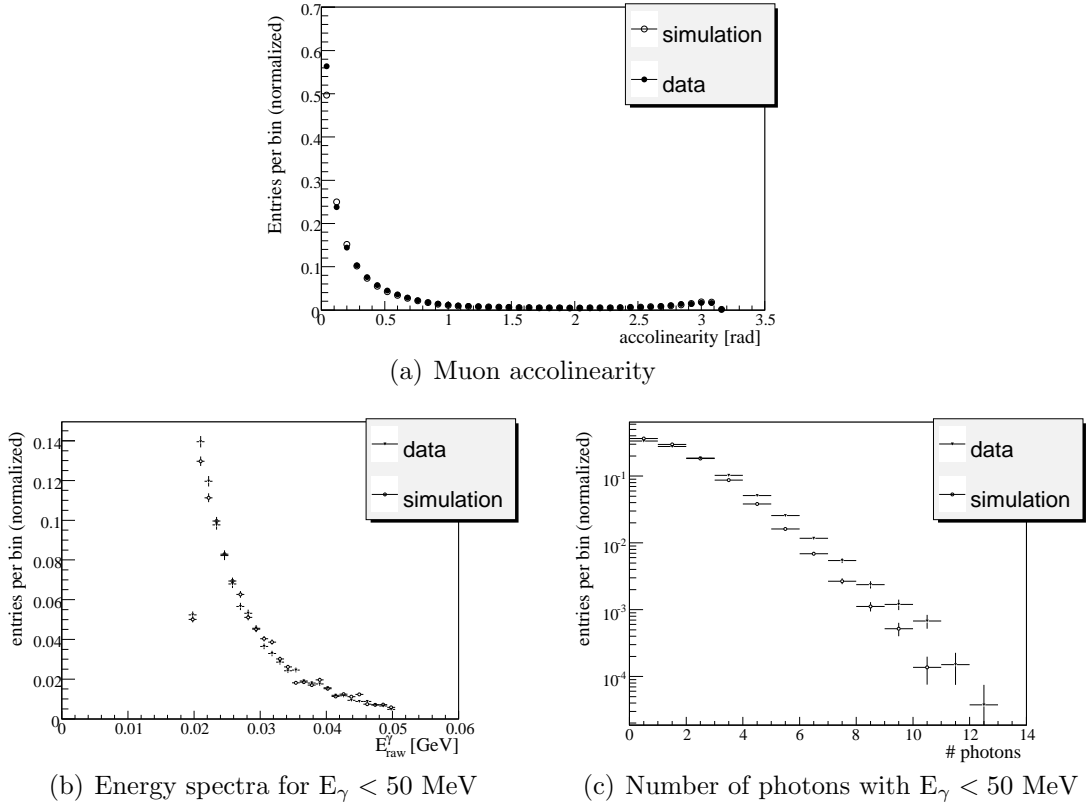


Figure 4.5: Comparison of data and simulated data: (a) Accolinearity of the muons in the c.m. system. (b) Energy spectrum of photons with $E_\gamma < 50$ MeV. (c) Number of photons with $E_\gamma < 50$ MeV. Please note the logarithmic scale in (c). All distributions are normalized to equal area (the normalization for (a) starts at the second entry).

well. In both the energy spectrum and the number of photons, the simulation provides a good description of the data.

4.5 Truth Matching in the Simulation

The process of truth matching for simulated events describes the association of a reconstructed object in the calorimeter to a generator level object in the Monte Carlo simulation.

For Charged Tracks

A track is reconstructed from hits in the SVT, the DCH and for muons in the IFR. In the simulation, these hits are created from generator level hits which are in turn created from generator level tracks (by the GEANT4 software). This means that a given reconstructed track may be constructed from hits which originate from

several different generator level tracks. The simulated track which contributed most hits to the reconstructed track is *truth-matched* to the track. This track will be referred to as *generated track* or *true track*.

For Neutral Clusters

A cluster is reconstructed from the energy deposited in one or more crystals in the EMC. In the simulation, this energy may originate from one or more generator level objects. The object which contributed most of the energy to a reconstructed cluster is called *truth matched* to the cluster. The generated object which is *truth matched* to the reconstructed photon is called the *generated photon* or the *true photon*.

4.6 Peak Fit Procedure

Throughout this thesis, the peak positions of the asymmetric distributions have to be determined in a stable, reproducible way. For calibration purposes, it is important to determine the peak position as precise as possible and without dependence on the fraction of events outside the central area of the distributions. Therefore, the peak position of a given distribution is determined by an iterative fitting procedure defined in this section.

The phenomenologically motivated *Novosibirsk Function* is used [22],

$$f(\mu) = C \exp \left[-\frac{1}{2} \left(\frac{\ln^2 \left(1 + \frac{\sinh(\tau\sqrt{\ln 4}) (\mu - \mu_0)}{\ln 4 \sigma} \right)}{\tau^2} + \tau^2 \right) \right], \quad (4.2)$$

where C is the normalization constant, μ the peak, σ the width and the parameter τ describes the size of the asymmetry of the entries. For $\tau \rightarrow 0$, the *Novosibirsk Function* turns into a Gaussian function. A nonzero τ allows to describe asymmetric functions.

The fits are performed with a χ^2 minimization using MINUIT [14] within the ROOT framework. All errors quoted are the 1σ standard deviations as computed by the fitting procedure, unless stated differently.

The fit range is limited to decouple the dependence on the number of entries outside the central region of the distribution. In order to increase the stability of the fitting procedure, it is performed iteratively:

1. The normalization constant, mean and RMS values are calculated from the histogram and used as start values for minimization with a Gaussian function. The Gaussian is fitted to the histogram in the range of $[-3\sigma, 3\sigma]$ around the peak.
2. The results from the Gaussian fit are used as start values for the *Novosibirsk Function* which is then fitted in the limited range $[-1.3\sigma, 1.3\sigma]$ around the peak.

3. The start values of the *Novosibirsk Function* are set to the fit results of step two. It is fitted again in the range $[-1.3\sigma, 1.3\sigma]$ around the peak to increase the stability.
4. The final fit is initialized with the values from the last iteration step and performed over a range dependent on the quantity which is intended to be determined.
 - (i) If the peak position is of interest, the last iteration is performed over a relatively small range of $[-1.2\sigma, 1.2\sigma]$ around the peak.
 - (ii) If the width is of interest, the fit range has to be extended since the fit has to cover values well below the half maximum in order to have a well defined FWHM. The fit is performed in the range $[-1.6\sigma, 1.6\sigma]$ around the peak.

The fitting procedure described above gives a very stable determination of the peak position and the width. Throughout this thesis, it will be used to determine the peak and width of given distributions, unless stated otherwise.

Fig. 4.6 shows exemplarily the ratio of the momentum of a measured track over the momentum of the truth matched track, p_{reco}/p_{true} . The distribution is fitted with the described algorithm. Sub-figures (a) and (b) display the two ranges described in step 4, (i) and (ii).

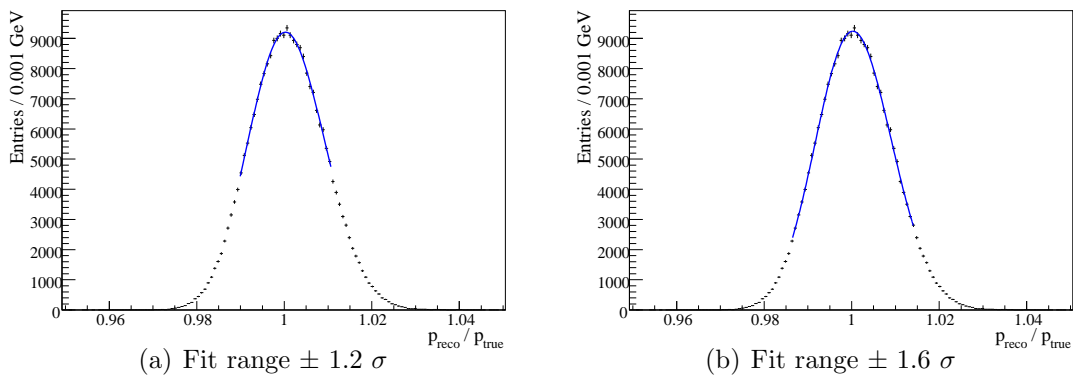


Figure 4.6: p_{reco}/p_{true} for muons. The two fits shown are as described, (a) for the determination of the peak position and (b) for the FWHM.

4.7 Photon Energy Estimate

In the $\mu\mu\gamma$ event sample, it is possible to calculate the photon energy from the four vectors of the charged particles, *i.e.* the muons and the beam electrons. In the energy range studied with the *BABAR* detector, charged particles can be measured much more precisely than neutral ones. Therefore the calculation can

be made without any calorimeter information. Thus, the estimate of energy and momentum of the photon has no bias from the calorimeter. The easiest way to calculate the photon energy is by a four vector calculation. This estimate can be improved with a kinematic fit. After a discussion of the input variables for the calculation, the different methods to calculate the photon properties are analyzed.

4.7.1 Input Variables

The photon energy is calculated from the measurement of the muon tracks in the tracking system and from the beam parameters.

Muons

The muons are measured in the tracking devices (*i.e.* vertex detector, drift and muon chamber) with a very high accuracy. The momentum and position resolution of the tracking system is discussed in section 3.2.2.

The final state of the event sample studied in this thesis consists of two muons and one high energetic photon. The momenta of the muons and the photon energy are anti-correlated. The precision of the photon energy estimate depends on the momentum resolution of the muon tracks associated with the photon. Thus, the momentum resolution (the sigma of p_{reco}/p_{true}) is studied as a function of the reconstructed photon energy (E_{raw}) in the simulation. The distribution of p_{reco}/p_{true} is shown in Fig. 4.6 as an example for the fitting procedure for the photon energy range of 0.4 to 0.6 GeV. In Fig. 4.7, the width of this distribution is shown as a function of the reconstructed photon energy.

Over the whole range studied, the momentum resolution in Monte Carlo simulation decreases from 0.9% - 0.5% with increasing photon energy from 400 MeV to 7 GeV. This decrease in momentum resolution is easily understood since with increasing photon energy the muon momentum decreases and thus the measurement of the drift chamber becomes more precise.

Systematic deviations between data and simulation as well as possible biases can be studied using the decay $J/\Psi \rightarrow \mu\mu$. The known mass of the J/Ψ is compared with the reconstructed dimuon mass. This study has been performed by R. Nogovski [13]. Systematic deviations in the Monte Carlo simulation describing the momentum measurement of charged particles in data are found to be at the level of 0.1%.

Beam Parameters

The beam parameters of the PEP-II storage ring are calculated from the total magnetic bending strength and the average deviations of the accelerating frequencies from their central values. The RMS energy spreads of the LER and HER beams are 2.3 and 5.5 MeV respectively [1]. That corresponds to a relative spread of 0.07 and 0.06% respectively.

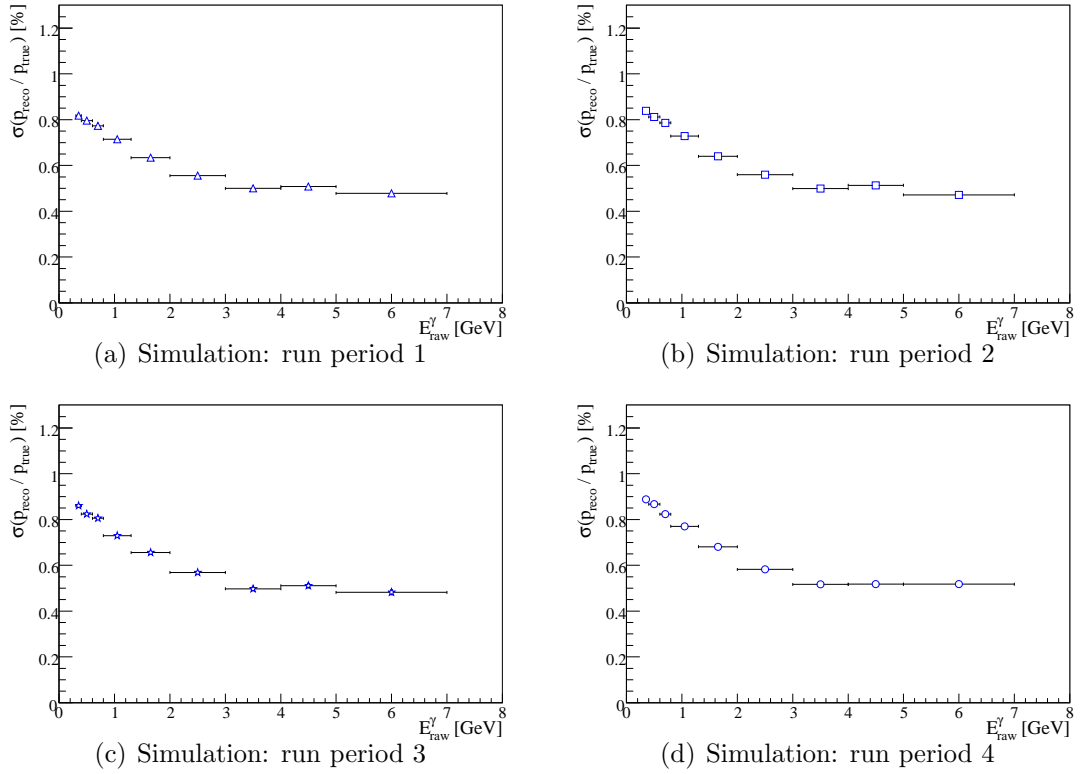


Figure 4.7: *Tracking resolution for muons as a function of photon energy.*

4.7.2 Four Vector Estimate

In principle it is straight forward to calculate the four vector of the photon \mathbf{p}_γ from the measured four vectors of the two muon tracks and the beam parameters,

$$\mathbf{p}_\gamma = (\mathbf{p}_{e^+} + \mathbf{p}_{e^-}) - (\mathbf{p}_{\mu^+} + \mathbf{p}_{\mu^-}), \quad (4.3)$$

where \mathbf{p}_γ denotes the four vector of the photon, \mathbf{p}_e the four vectors of the beam particles and \mathbf{p}_μ the four vectors of the muons. However, this naive equation does not take into account the finite resolution of the tracking devices. Thus, $(\mathbf{p}_\gamma)^2$ is not necessarily zero as expected for massless photons.

The photon deduced from four vector calculation has to be matched to a reconstructed photon. With the event selection discussed in section 4.2, only one photon with an energy higher than 50 MeV is present in the sample. Since only hard radiative photons are studied in this thesis, the reconstructed high energetic photon is taken to be the photon radiated from the muons and thus the photon calculated in the four vector estimate.

When comparing the calculated photon with generator level information, the estimated photon is matched first with the reconstructed one. In a second step, a generated photon is truth matched to the reconstructed photon. Thus, the

matching between the calculated and the generated photon is done indirectly using the reconstructed one.

In Fig. 4.8 (a), the photon energy estimate of the four vector addition is shown as a function of the generator level energy. The majority of the events populates the diagonal, meaning the calculated photon is a good estimate for the reconstructed one. However, roughly 5% of the events are seen off the diagonal. A significant amount of photons is wrongly predicted to have a high energy. In this case, a high energetic photon gets emitted outside the acceptance of the calorimeter and hence a lower energetic photon is mistaken as the photon radiated by the muons. Thus, the calculated photon is not matched to the radiated photon, but to another, low energetic photon.

An accumulation of photons generated with a high energy with almost zero energy predicted is seen as well. In these cases, a high energetic photon which is not produced in initial state radiation seems to be present in the sample. This high energetic photon gets matched to the calculated one.

4.7.3 Kinematic Fit

The four vector calculation of the photon properties can be improved using a kinematic fit. The kinematic fit is based on an iterative χ^2 minimization. The external constraints are introduced using the concept of Lagrange multipliers [19]:

$$\chi^2 = (\vec{P} - \vec{P}_0)^T V^{-1} (\vec{P} - \vec{P}_0) + 2\lambda \vec{f}(\vec{P}), \quad (4.4)$$

where V is the covariance matrix, \vec{P} the fit momentum vector, \vec{P}_0 the expected momentum vector and $\vec{f}(\vec{P})$ the constraint function. The vectors are column vectors including the vectors of all particles. The expected momentum vector is the measured track momentum for the muons. For the photon, the above described four vector estimate is used. The covariance matrix V consists of the individual error matrices for the charged and neutral particles participating in the fit. The covariance matrix of the photon is estimated from the covariance matrices of the charged particles².

The following conditions are used as constraints:

1. The invariant mass of the fitted photon is set to zero, the masses of the charged tracks are set to the muon mass,
2. the total energy in the c.m. frame is set to the measured beam energy and
3. the fitted particles are constrained to originate from the beam spot.

²The method of determining the covariance matrix of the photon is not rigorously correct since the resulting matrix is correlated with the muon covariance matrices. The errors of the photon are therefore not calculated correctly within the kinematic fit. However, the following discussion shows that a clear improvement of the estimate of the photon energy is achieved by using the kinematic fit.

The energy calculated by the kinematic fit is shown in Fig. 4.8 (b) as a function of the generated energy. The accumulations seen beside the diagonal are almost identical to those seen in the four vector calculation. This is expected since they are due to a mismatch between the calculated and the reconstructed photon.

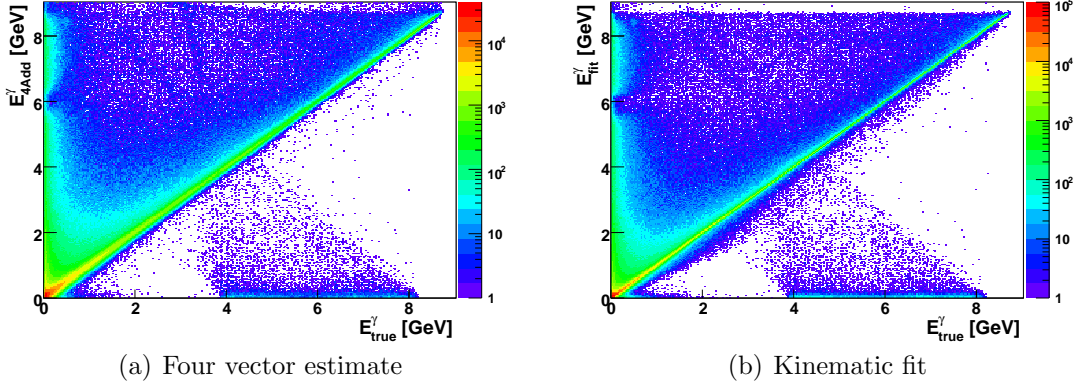


Figure 4.8: *Correlation of calculated and generated energy for (a) four vector estimate and (b) kinematic fit. No cuts to improve the estimate are applied, but all cuts of the event selection.*

4.7.4 Fit Quality

In some cases, as discussed in section 4.7.2, either the assumption of a $\mu\mu\gamma$ final state failed, or the association of the calculated with the reconstructed photon did not work. Thus, the photon estimate can be improved by additional selection criteria to rule out those cases:

1. The χ^2/dof of the kinematic fit is required to be smaller than 2.0, where dof denotes the degrees of freedom of the fit. This guarantees that the assumption of the event structure is fulfilled reasonably well.
2. The calculated energy has to be between 30% and 200% of the reconstructed energy. This guarantees that the calculated photon energy is in the right order of magnitude. The requirement is kept loose to minimize the bias introduced from the energy measurement.
3. The calculated position is required to be within 15 cm of the reconstructed one. The value of 15 cm corresponds roughly to four crystal sizes. This requirement guarantees that the calculated photon position is in the right region of the EMC. This requirement is kept loose enough to minimize systematic effects.

In Fig. 4.9 the calculated photon energy is shown as a function of the generated one with the requirements 2 and 3 applied for the four vector calculation and

with all three requirements applied for the kinematic fit. The accumulations seen in Fig. 4.8 have vanished. Both the kinematic fit and the four vector addition estimate the energy with entries to energies estimated too high. However, the fraction of these events is small.

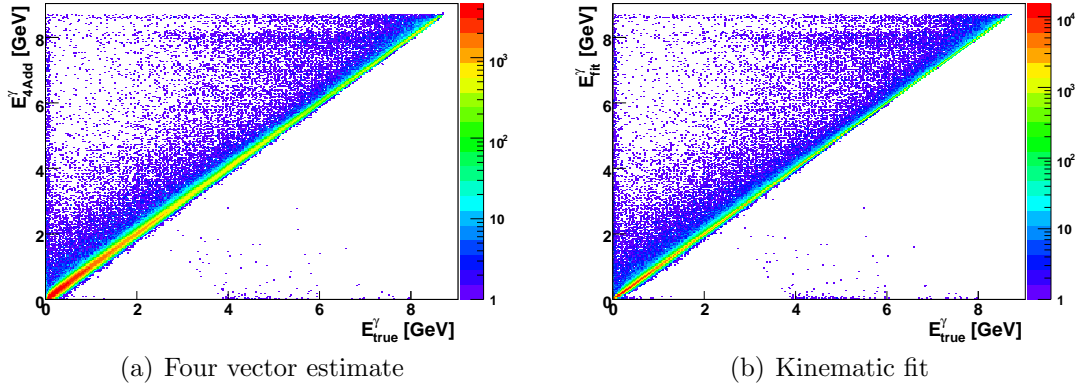


Figure 4.9: Correlation of calculated and generated energy for (a) four vector addition and (b) kinematic fit. All cuts for the fit quality are applied. The accumulations seen in Fig. 4.8 have vanished.

In Fig. 4.10 the ratio of the estimated over the generated energy is shown for two different ranges in the generated energy, $0.4 \text{ GeV} < E_{true} < 2 \text{ GeV}$ in Fig. 4.10 (a) and $2 \text{ GeV} < E_{true} < 4 \text{ GeV}$ in Fig. 4.10 (b). The calculation using the kinematic fit is drawn as black histogram and the four vector calculation in red. Both distributions are normalized to equal area. It is clearly seen that the kinematic fit gives a much better estimate for the generated energy. The improvement is mainly due to the additional information of the particle masses in the kinematic fit. Thus, the calculation of the photon properties with the kinematic fit is used throughout this thesis to estimate the photon properties.

The data sample available with all selections for the event type and the quality of the photon estimate applied is shown in table 4.2.

Run Period	Data	Simulation
1	$378 \cdot 10^3$ events	$414 \cdot 10^3$ events
2	$1034 \cdot 10^3$ events	$1298 \cdot 10^3$ events
3	$549 \cdot 10^3$ events	$224 \cdot 10^3$ events
4	$1472 \cdot 10^3$ events	$1543 \cdot 10^3$ events

Table 4.2: Number of photons available after all selection cuts. Except for the run period 3, the simulated events are more than data events.

An estimate for the quality of the fit and selection procedure is the peak position of the ratio of E_{fit}/E_{true} . It is shown in Fig. 4.11 (a) as a function of the

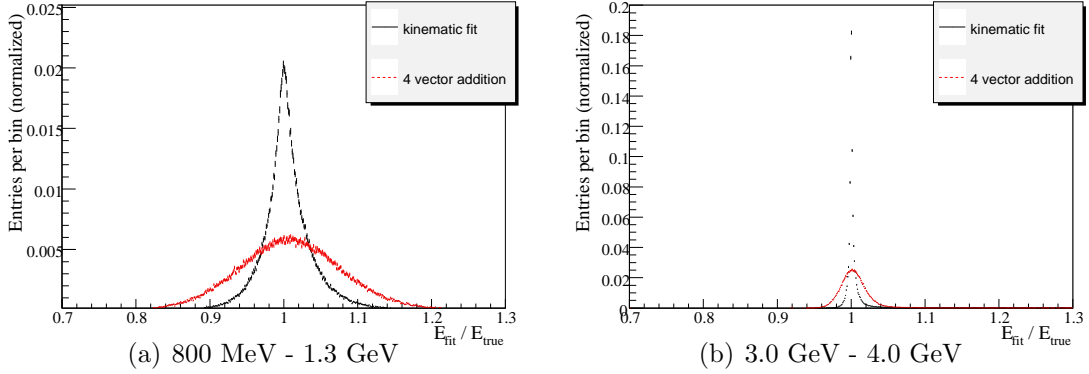


Figure 4.10: Ratio of calculated over generated energy for the kinematic fit (black) and the four vector calculation (red). Two ranges in the generated energy are shown. The distributions are normalized to equal area. The kinematic fit gives a much better estimate for the generated energy than the four vector calculation.

energy and in Fig. 4.11 (b) as a function of the polar angle for an energy range of 0.4 to 2 GeV. In both figures, the peak position is with an accuracy of 0.1% at 1.0. That means that the calculated energy is a very good estimate for the generated one.

In Fig. 4.12 (a), the width of the ratio E_{fit}/E_{true} is shown as a function of the photon energy. With increasing energies the fit resolution gets better. At energies below 400 MeV, the energy calculated by the fit deviates from the true energy and the resolution of the calculated energy is worse than 4%. Therefore, only energies above this value are considered for calibration. In the region between 0.4 and 2 GeV, the kinematic fit works as estimate for the true energy, but the finite resolution has to be considered. At photon energies above 2.0 GeV, the resolution of the fit estimate is negligible. In Fig. 4.12 (b) the width is shown as a function of the polar angle for the energy range of 400 MeV - 2.0 GeV. Throughout the whole range, it has a non-negligible value.

The position calculated with the kinematic fit is tested with the ratio $\theta_{fit} / \theta_{true}$ in Fig. 4.13 (a) as a function of the energy and (b) as a function of the polar angle. As for the energy, the fit estimate is excellent for energies above 400 MeV and has no bias over the polar angle range.

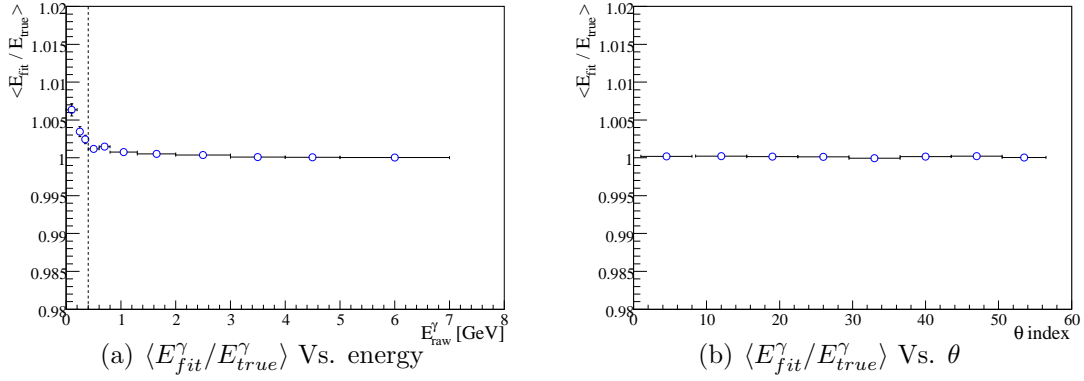


Figure 4.11: Photon energy calculated with the kinematic fit over generated energy. (a) As a function of the photon energy. (b) As a function of the photon polar angle. The energy range of 0.4 - 2.0 GeV is chosen here. The peak positions agrees within 0.1% with 1.0.

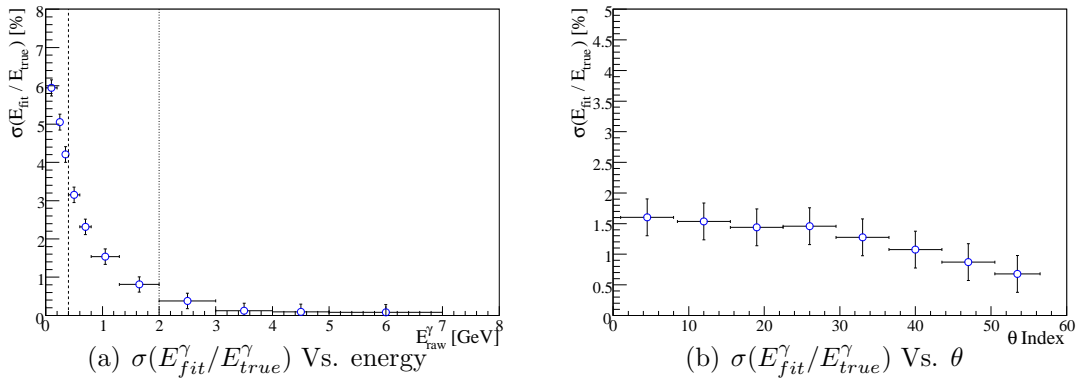


Figure 4.12: Width of the photon energy calculated by the kinematic fit over generated energy. (a) As a function of the photon energy. The width becomes negligible at photon energies above 2.0 GeV. (b) As a function of the photon polar angle. The energy range of 0.4 - 2.0 GeV is chosen here. The kinematic fit is used in the energy range above 0.4 GeV.

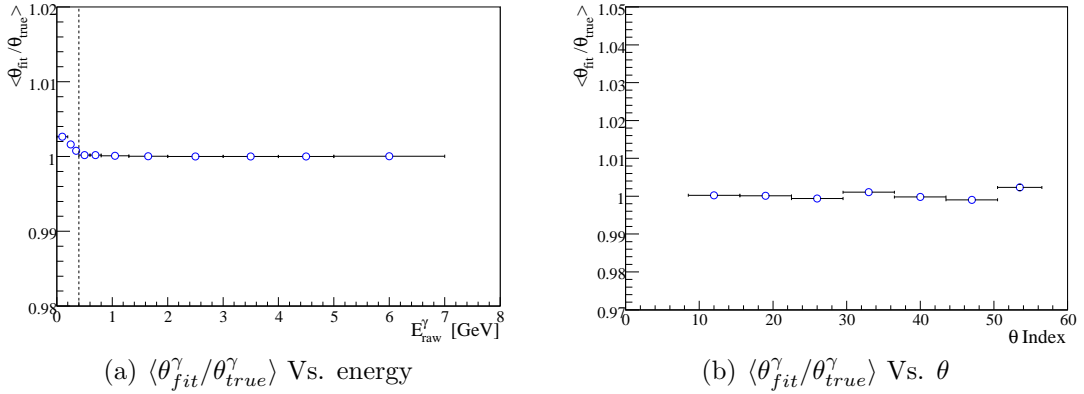


Figure 4.13: Peak position of $\theta_{fit} / \theta_{true}$ (a) versus photon energy and (b) versus the photon polar angle for energies of 2 - 4 GeV. For energies above 400 MeV and over the whole polar angle, the kinematic fit provides an excellent estimate for the generated angle.

4.8 Summary

With the criteria presented, it is possible to select a well defined sample of

$$e^+e^- \rightarrow \mu^+\mu^-\gamma \quad (4.5)$$

events. The Monte Carlo simulation has proven to describe the data in all observed quantities.

The energy and the polar angle of the radiated photon can be calculated using only the beam parameters and the muon momenta measured in the tracking devices. The photon properties can be estimated by a four vector calculation, but due to a finite detector resolution, the invariant mass of the calculated particle is not necessarily zero as expected for massless photons. This calculation can be improved using a kinematic fitting procedure with the additional information of the particle masses and the constraint that particles originate from the beam spot.

A sample is chosen where the association between the calculated, the reconstructed and for simulation the generated photon works reliably. The calculation using the kinematic fit has proven to estimate the photon energy and position with a minimal bias. The energy range usable for the kinematic fit is 400 MeV to 7 GeV. Between 400 MeV and 2 GeV, the kinematic fit has some uncertainties calculating the photon properties due to the finite tracking resolution. Above 2.0 GeV, the calculation gives an excellent estimate for the photon energy and position.

Chapter 5

Photon Energy Measurement

The electromagnetic calorimeter is the only device which allows to reconstruct photons in the *BABAR* detector. In order to measure photons at the right energy scale, an energy calibration is needed.

After a short discussion of the energy response of the calorimeter, a new cluster energy calibration using events of the type $e^+e^- \rightarrow \mu^+\mu^-\gamma$ is presented. With these events, it is possible to perform a calibration purely based on data up to energies of 7 GeV. The calibration is based on the energy of the radiated photon, calculated with a kinematic fit. This calculation has a finite resolution due to the tracking uncertainties. Therefore, the calibration cannot be taken directly from the comparison of measured and calculated energy. Instead, the uncalibrated data has to be normalized to the simulation. As discussed in section 3.3.3, the generated energy has to be corrected for simulated energy losses, which is called calibration of the simulation. The data can then be normalized to the simulation. After the cluster energy calibration is performed, systematic uncertainties are discussed.

In the second part of this chapter, the energy resolution of the calorimeter is determined for the high energy region.

5.1 Calorimeter Energy Response

As discussed in section 3.4, the energy calibration procedure of the EMC is separated into three steps:

1. Electronics calibration,
2. Single crystal calibration and
3. Cluster calibration.

This chapter focuses on the high energy part of the cluster energy calibration. To perform a calibration, the raw energy is compared with an estimate, where

$E_{raw} = \sum_i e_i$ and e_i is the energy of the crystal i (the result of calibration step 2). In case of simulated events, this estimate can be the energy of the simulated photon on generator level, E_{true} . In order to study the raw energy in the simulation, the ratio E_{raw}/E_{true} is analyzed.

Fig. 5.1 shows this ratio in two different energy ranges. The peak position is about 5% below 1.0 since not all of the photon energy is contained in the active material of the calorimeter (see section 3.4 for a detailed discussion). The distribution is not Gaussian in shape, it has entries outside the central area to lower energies. They are due to photons which have lost more energy in front of the calorimeter, *e.g.* those which started showering in the DIRC.

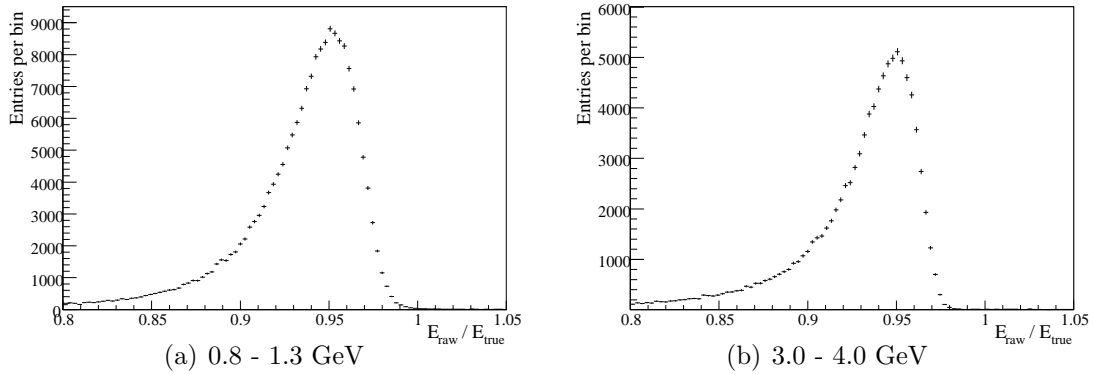


Figure 5.1: Energy response of the calorimeter in $\mu\mu\gamma$ simulation: E_{raw}/E_{true} for low and high photon energies.

The $\mu\mu\gamma$ data sample, provides photons with known energies for both data and simulation (see section 4.7.3). The raw energy can be compared with an estimate from the kinematic fit, E_{fit} . The ratio E_{raw}/E_{fit} is shown in Fig. 5.2 data and simulation in the same two energy ranges as in Fig. 5.1. The calorimeter response in data is not perfectly described in the simulation. The peak position is about 1% higher in the simulation for both energy ranges. The number of entries at low energies is overestimated in the simulation. The width of the distribution at lower energies has a significant contribution due to the resolution of the kinematic fit. Thus, the asymmetry of the energy response is washed out. As discussed in section 4.7.1, the input variables for the calculation of E_{fit} agree on a level better than 0.1%. Therefore the differences seen in the ratio E_{raw}/E_{fit} are due to a different calorimeter response in data and simulation, not to a difference in the estimate of the fit.

Since the energy response of the EMC differs for data and Monte Carlo simulation, the cluster energy has to be calibrated separately for data and the simulation.

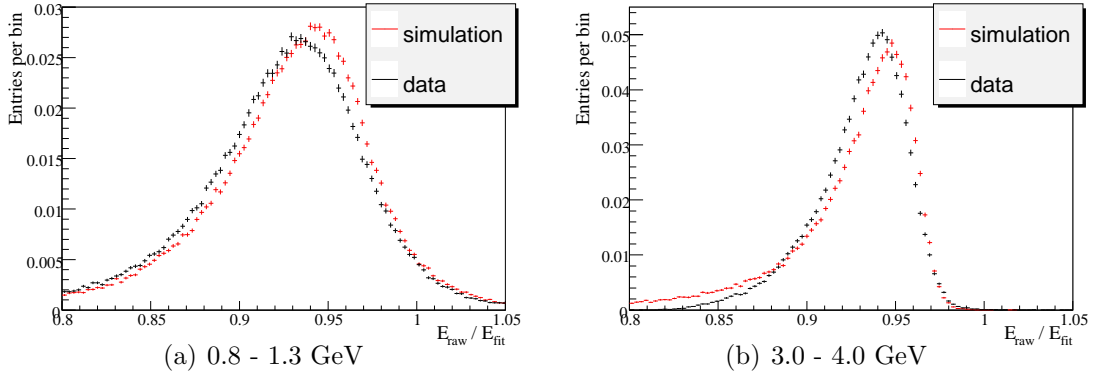


Figure 5.2: Energy response of the calorimeter for data and simulation: E_{raw}/E_{fit} for low and high energies (normalized to equal area). Systematic deviations in the peak position are seen in both energy ranges, in the high energy range the shape is clearly different as well. For low energies, the fit resolution gives a significant contribution to the width.

5.2 Cluster Energy Calibration

After introducing calibration algorithm, the cluster energy calibration for simulation and data will be discussed. At the end, the derived parameterization of the calibration function is verified.

5.2.1 Calibration Algorithm

In order to increase the stability of the calibration factors, the photon energy is shifted to the correct peak values, not to the correct mean. The peak is not influenced by entries outside the central area as the mean is. Calibrating the peak yields to a correct *most probable value* whereas calibrating the mean would yield in a photon energy which is *on average* correct.

Determination of the Calibration Factors

The fit estimate has a finite resolution (see section 4.7.4) which implies that the calibration factor in data cannot simply be derived from the ratio E_{raw}/E_{fit} . Instead, the energy in data has to be normalized to the simulation. Therefore, the measured energy in the simulation is corrected for the energy losses first, using the generated energy. This is called the calibration of the simulation.

Dependencies of the Calibration Factors

The time dependence of the calibration factors due to radiation damage is covered by the single crystal calibration. In order to correct possible other time

dependencies, the calibration factors are obtained for each of the four run periods separately.

The cluster calibration factor will depend on the energy since the shower depth increases proportional to the logarithm of the energy and thus leakage behind the crystal becomes more important at higher energies. It will as well depend on the polar angle since the material distribution in front of the EMC differs with θ . Since the EMC is completely symmetric in ϕ , no dependence on azimuthal angle is expected.

The cluster calibration factors are derived in bins of energy (E_{raw}) and polar angle (θ). The number of events in the $\mu\mu\gamma$ sample is not sufficient to derive the calibration in two dimensions. Also, it cannot be assumed that the calibration function factorizes in energy and polar angle dependent parts. Therefore, the polar angle dependent part of the calibration function is determined in three bins of the energy.

The energy calibration is performed in two steps: After the calibration of the energy dependence, the dependence on the polar angle is corrected. The total calibration function $c(E, \theta)$ is then defined as

$$c(E, \theta) = c_1(E) \cdot c_2^E(\theta) \quad (5.1)$$

where $c_1(E)$ is only the energy dependent part and $c_2^E(\theta)$ is the polar angle dependent part which is derived in three bins of energy.

The energy dependent calibration function $c_1(E)$ is obtained as a fit of the calibration factors obtained in 8 bins of the energy. The energy bins are chosen to have approximately equal statistics (see Fig. 4.1 for the photon phase space), therefore their size increases with increasing energy. The bins are shown in table 5.1.

The dependence on the polar angle is determined in 8 bins in the polar angle as well as in three energy bins. The polar angle bins are chosen equal to the module structure of the EMC described in section 3.3.2. The energy range of 0.4 - 4.0 GeV is divided into three bins. For energies above 4.0 GeV, the photons don't cover the whole calorimeter and thus a polar angle dependent calibration is not possible. To correct the cluster energy of these photons, the correction obtained in the 2.0 - 4.0 GeV energy bin is used. The bins of the polar angle dependent calibration are shown in table 5.1.

The determination of the cluster energy calibration is performed in $8 + 3 \cdot 8$ bins, 8 bins for the energy dependent calibration function and $3 \cdot 8$ bins for the calibration function dependent on the polar angle which is taken in three energy bins.

5.2.2 Simulation

The Monte Carlo cluster calibration is performed with generator level information. That is, the Monte Carlo calibration function is obtained from the peak

energy dependence		theta dependence			
bin	energy [GeV]	bin	energy [GeV]	bin	I_θ
0	0.4 - 0.6	0	0.4 - 1.0	0	1 - 8
1	0.6 - 0.8	1	1.0 - 2.0	1	9 - 15
2	0.8 - 1.3	2	2.0 - 4.0	2	16 - 22
3	1.3 - 2.0			3	23 - 29
4	2.0 - 3.0			4	30 - 36
5	3.0 - 4.0			5	37 - 43
6	4.0 - 5.0			6	44 - 50
7	5.0 - 7.0			7	51 - 56

Table 5.1: Bins used in the energy dependent calibration are shown in the left hand side of the table. The bins used for the polar angle dependent calibration are shown on the right hand side. The endcap, $I_\theta = 1 - 8$, is treated separately.

position of the ratio of the reconstructed over the generated energy,

$$c_{MC}(E, \theta) = \frac{1}{\text{peak}(E_{raw}^{MC}/E_{true}^{MC})}, \quad (5.2)$$

where E_{raw}^{MC} denotes the reconstructed energy without the cluster calibration applied and $\text{peak}()$ denotes the peak position of the given distribution. The peak position is determined with the algorithm discussed in section 4.6.

In order to cancel systematic effects, the Monte Carlo calibration is performed using a method as close as possible to the calibration in data. It is done with the $\mu\mu\gamma$ simulation in the same binning used in data. As discussed in section 4.3, no significant differences in the phase space multiplicity of the muons exist between data and simulation.

The calibration function, $c_{MC}(E, \theta)$, is determined assuming that it factorizes in parts according to Eq. 5.1. Thus, the cluster energy calibration in the Monte Carlo simulation is divided in two steps. The energy dependence is determined before the polar angle dependence.

Energy Dependence

The energy dependent calibration function $c_{1,MC}(E)$ is determined from the peak of the distribution of reconstructed over the generated energy. The peak position is obtained using the method described in section 4.6.

The energy dependent calibration factors determined according to Eq. 5.2 are shown as a function of the logarithm of the energy in Fig. 5.3. All errors are statistical errors only. A third order polynomial is fitted to the points. This function is taken as the calibration function $c_{1,MC}(E)$. It rises slowly to higher

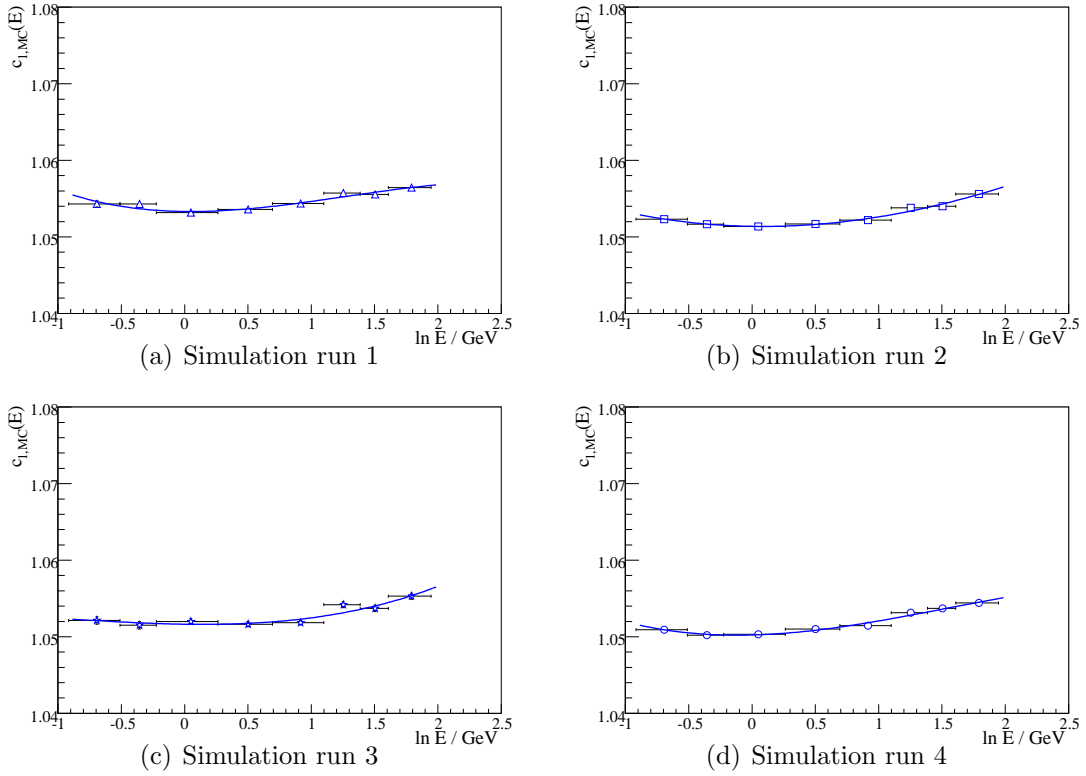


Figure 5.3: *Simulation of $\mu\mu\gamma$ data: Calibration function $c_1^{MC}(E)$ as function of the logarithm of the energy for the four different run periods. Note the logarithmic scale, -1 corresponds to 400 MeV and $+2$ to 7 GeV.*

energies. The overall scale of the calibration function changed for about 0.3% between the run periods. This is due to a change of the electronics read out algorithm after the run periods 1 and 3, which is included in the Monte Carlo simulation.

The rise at higher energies is due to the logarithmic increase of the penetration depth of the shower center with the energy and thus leakage behind the crystals becomes more important at high energies. The increase at low energies is due to the increasing relative energy loss in front of the EMC for lower energies.

Polar Angle Dependence

The calibration function $c_{1,MC}(E)$ is applied to the reconstructed energy to correct for the energy dependence. The corrected cluster energy, is then calibrated for the dependence of the polar angle.

Three different calibration functions for the three energy bins are determined. Each function is fitted as third order polynomial to the calibration factors determined using Eq. 5.2. In Fig. 5.4, the calibration factors $c_{2,MC}^E(\theta)$ are shown as a

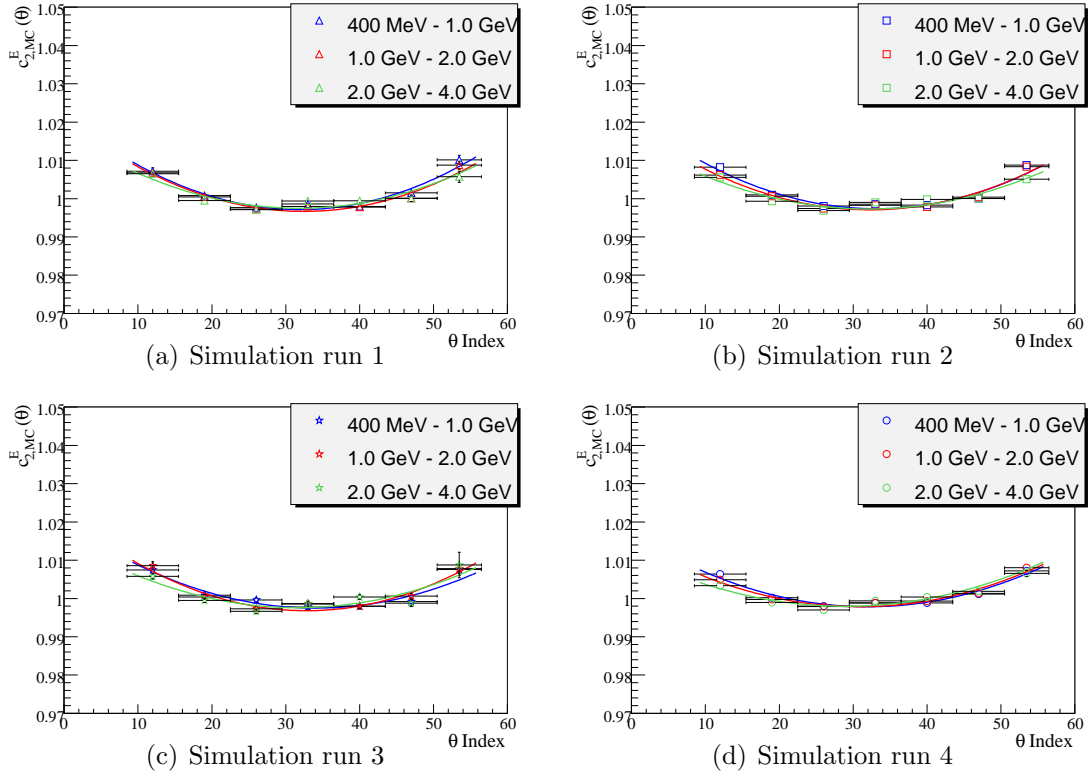


Figure 5.4: *Simulation: Calibration factor $c_{2,MC}^E(\theta)$ as function of the θ index for the 4 different run periods. The colors indicate the energy range: blue for 0.4 - 1.0 GeV, red for 1.0 - 2.0 GeV and green for 2.0 - 4.0 GeV. The calibration function shows no dependence on energy as well as no dependence on the run period.*

function of the crystal θ index.

Within the statistical significance, no dependence on the energy is seen. This indicates that the calibration function factorizes in energy and polar angle dependent parts. Within the significance, no difference between the four run periods is seen either.

Results of the Monte Carlo Calibration

In order to test the parameterization of the Monte Carlo calibration, the complete calibration function

$$c_{MC} = c_{1,MC}(E) \cdot c_{2,MC}^E(\theta) \quad (5.3)$$

is applied to the reconstructed energy. The ratio of the cluster energy calibrated and the generated energy is determined to test the calibration. In Fig. 5.5 (a) - (d) the peak position is shown as a function of the logarithm of the energy. The peak positions are at 1.0 with a deviation of less than 0.1%. The dependence of

the peak positions on the polar angle is shown in Fig. 5.5 (e) - (h). For the test of the parameterization, the polar angle is not divided in energy bins. The peak position is at 1.0 with a spread of 0.1 - 0.2% which is well within the statistical significance.

It can be concluded that the Monte Carlo simulation is calibrated to the correct peak position. The data can be normalized to the simulation in the next step.

Study of the Fit Bias

For the energy calibration in data, the ratio of reconstructed over fitted energy has to be evaluated. That is, the ratio of two broad, asymmetric distributions is taken. Thus, the peak position of the ratio gets shifted. This shift in the peak position due to the finite resolution of the kinematic fit will be studied in the Monte Carlo simulation in the following. For a more descriptive understanding of the effect, the distributions involved are shown exemplarily in Fig. 5.6 (a) - (c) for the lowest energy bin, 400 to 600 MeV. The effect is the largest here since the resolution of the estimate of the kinematic fit is large at low photon energies. Arrows indicate the peak position.

In Fig. 5.6 (a) the distribution of the calibrated over the generated energy is shown. The distribution has a large number of entries outside the central area or lower energies which is due to energy losses outside of the calorimeter. The peak position is at 1.0. In Fig. 5.6 (b), the estimate of the kinematic fit over the generated energy is shown. The distribution is symmetric with a peak position at 1.0. The width of this distribution is the resolution of the fit. Taking the ratio of the calibrated over the fitted energy, as shown in Fig. 5.6 (c) results in a distribution with a peak position lower than 1.0. This is the result of the division of two extended distributions. Note that

$$peak\left(\frac{E_{cal}}{E_{fit}}\right) \neq \frac{peak\left(\frac{E_{cal}}{E_{true}}\right)}{peak\left(\frac{E_{fit}}{E_{true}}\right)}, \quad (5.4)$$

where E_{cal} denotes the cluster calibrated energy (as discussed in section 5.2.2), E_{true} the generator energy and E_{fit} the energy calculated using the kinematic fit. The peak position of the given distributions is denoted by $peak()$.

In Fig. 5.6 (d), the peak position of the three distributions described above is shown as a function of the logarithm of the energy. In the lowest energy bin, 400 to 600 MeV, the shift of the peak position is 1.6%. With increasing energy the shift becomes less important.

The uncertainties in the energy calculated of the kinematic fit introduce a bias in the ratio of reconstructed over fitted energy. This bias has to be corrected. The calibration factor for data is obtained as a shift of the peak position in data to the peak position of the calibrated simulation. The calibration factor for data

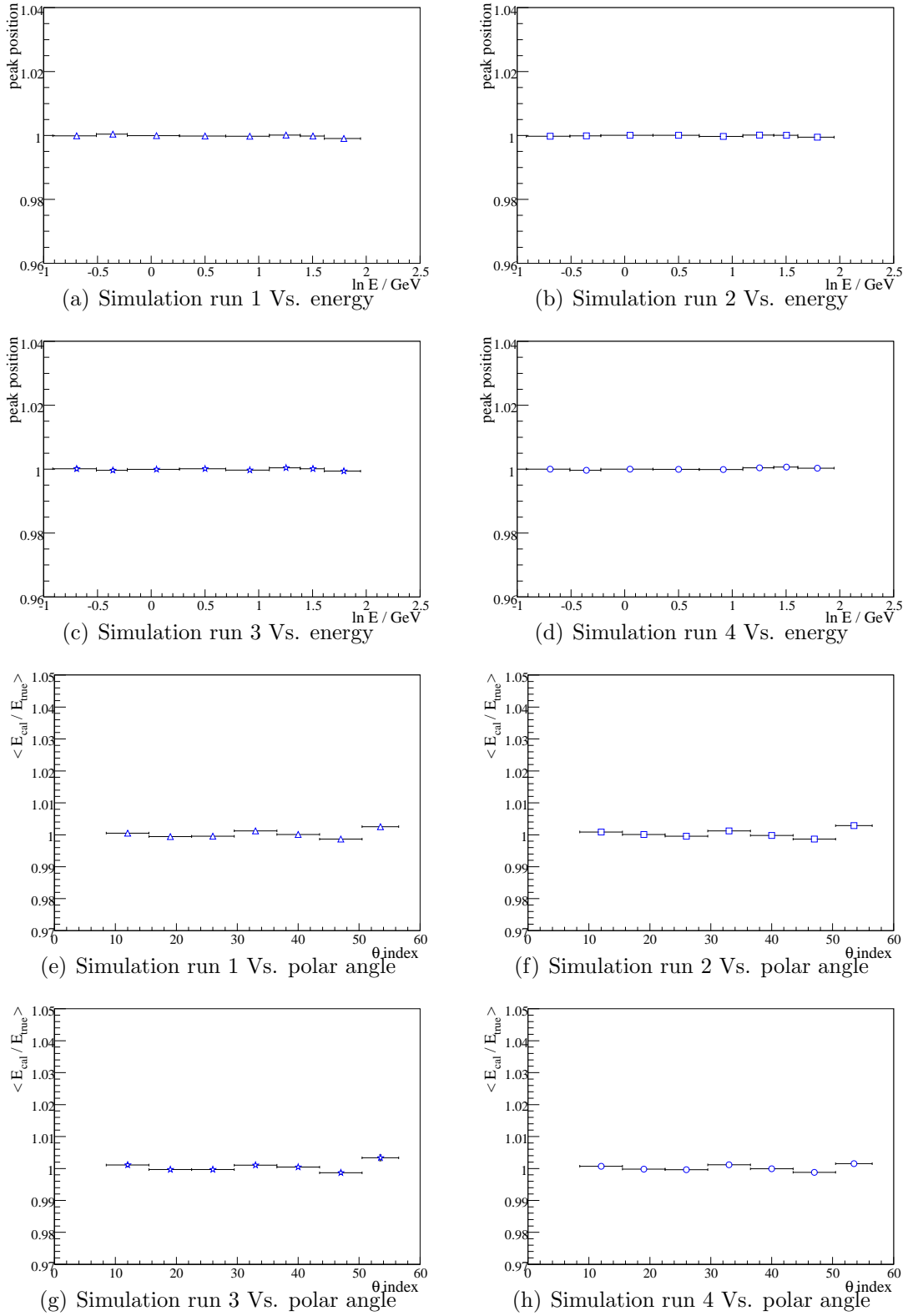


Figure 5.5: Peak positions of the ratio of calibrated and generated energy. (a) - (d) as a function of energy and (e) - (h) as a function of the crystal index in θ . All peak positions are in agreement with 1.0, the spread is of the order of 0.1 - 0.2 % versus the polar angle and smaller than 0.1% versus the energy.

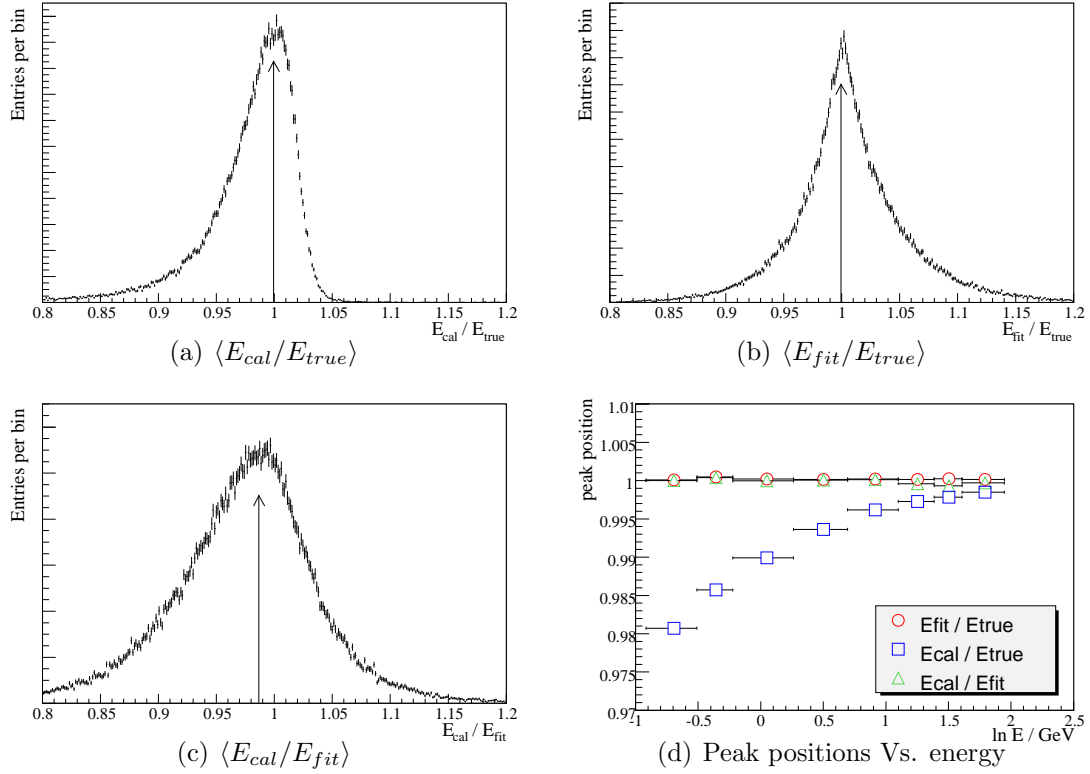


Figure 5.6: Simulation of $\mu\mu\gamma$ data: Example for the shift of the peak due to the finite width of the fitted energy for the energy range 400 - 600 MeV: (a)-(c) The peak of the calibrated over the generated energy is at 1.0 as well as the one of the fitted over the generated energy, but the peak position of the calibrated energy over the fit estimate is shifted. (d) Peak positions as a function of energy.

is thus defined as the double ratio Monte Carlo over data,

$$c_{data}(E, \theta) = \frac{peak(E_{cal}^{MC}/E_{fit}^{MC})}{peak(E_{raw}^{data}/E_{fit}^{data})}, \quad (5.5)$$

where $c_{data}(E, \theta)$ is the complete calibration factor for data. E_{cal}^{MC} denotes the cluster calibrated energy in the simulation, E_{raw}^{data} the raw energy in data and $E_{fit}^{MC/data}$ the energy calculated by the kinematic fit for simulation and data respectively. With this method, the bias observed as a shifted peak due to the resolution of E_{fit} is taken into account.

Test of the Bias Correction Strategy

The calibration scheme for data, Eq. 5.5, can be tested in Monte Carlo using generator information. The cluster calibration factor is obtained in two different

ways: Firstly, it is taken straight from the ratio of the uncalibrated energy over the generated value,

$$c_{MC}(E, \theta) = \frac{1}{\text{peak}(E_{raw}^{MC}/E_{true}^{MC})}, \quad (5.6)$$

as the calibration is done for the Monte Carlo simulation. Secondly, it is calculated using a double ratio analogue to the one defined in Eq. 5.5 (as implemented for the cluster calibration in data),

$$\widetilde{c}_{MC}(E, \theta) = \frac{\text{peak}(E_{cal}^{MC}/E_{fit}^{MC})}{\text{peak}(E_{raw}^{MC}/E_{fit}^{MC})} \quad (5.7)$$

where both the calibrated and un-calibrated energy is taken from the simulation. In this way, the unfolding of the shift of the calibration factor due to the fit resolution can be tested. The difference of the two calibration factors is a measure for systematic uncertainties in the calibration procedure.

Fig. 5.7 shows the calibration factors determined in the two different ways as a function of the logarithm of the energy. The Monte Carlo data for the four run periods is shown in the sub-figures 5.7 (a) - (d). Within the statistical errors, the calibration factors agree for all run periods. No systematic deviation between the two schemes is observed. The variations between the points are a measure for the systematic uncertainties of the calibration procedure, which is at most 0.1%. For the run periods with low event numbers, run 1 and 3, the variations between the two algorithms are statistically dominated.

In summary, the unfolding of the uncertainties of the energy estimate by the kinematic fit gives a very well defined peak position. Any further systematic errors of the calibration factors are due to differences between data and Monte Carlo simulation. Those differences and their implications are studied in section 5.3.

5.2.3 Data

As discussed in section 4.7.4, the photon energy can be calculated using a kinematic fit without any calorimeter information for energies above 400 MeV. The tracking measurement is not sufficient to estimate the photon energy below 400 MeV. Above this energy, a bias correction is necessary. As discussed in the previous section, evaluating the ratio simulation over data cancels the bias due to the finite resolution of the tracking measurement (assuming the same tracking resolution).

The calibration for data is determined in the same bins as the Monte Carlo calibration, it is splitted in an energy and a polar angle dependent part,

$$c_{data} = c_{1,data}(E) \cdot c_{2,data}^E(\theta). \quad (5.8)$$

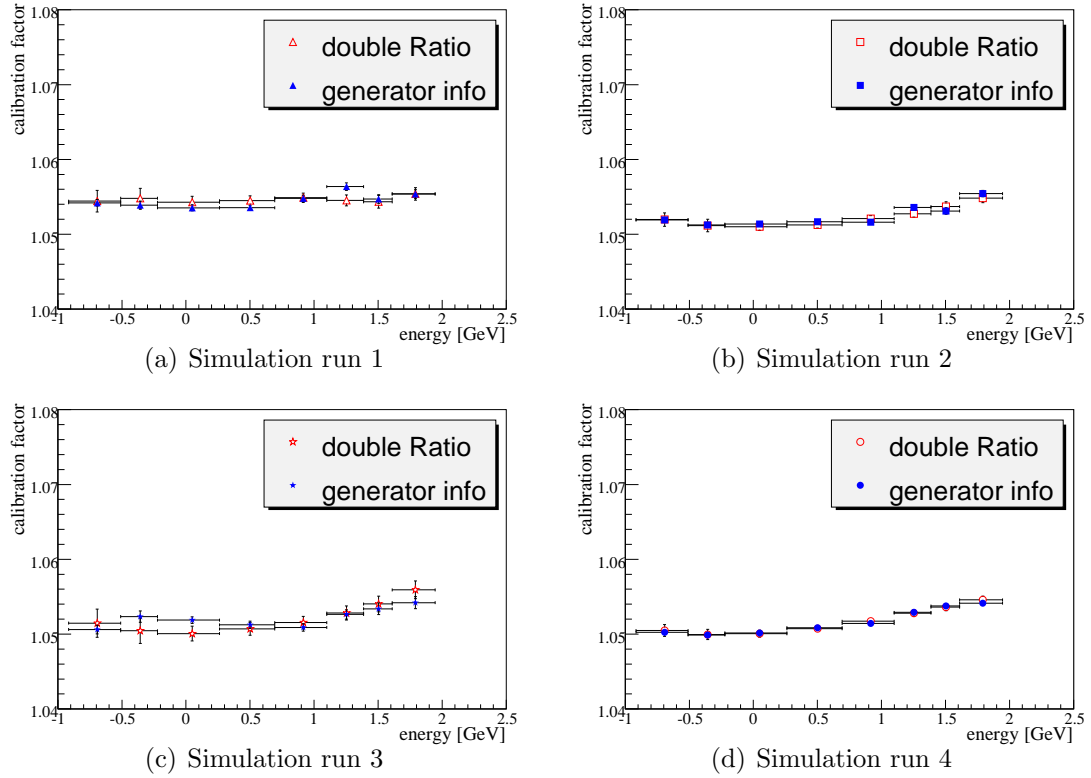


Figure 5.7: Monte Carlo simulation study of the calibration scheme. The energy calibration factors are obtained in two different ways: Firstly using generator information (blue markers) and secondly using the double ratio $\widetilde{c}_{MC}(E, \theta)$ as defined in Eq. 5.5 (red markers). Both techniques agree within the fit errors.

Energy Dependence

The energy dependent part of the calibration function $c_{1,data}(E)$ is determined from the double ratio (Eq. 5.5) in bins of the logarithm of the energy. In Fig. 5.8 this is shown for the four run periods. A third order polynomial is fitted to the points. The run periods 2-4 show only a small energy dependence. It varies for about 0.5% over the full range.

The calibration function obtained from the first data taking period of the *BABAR* detector has a completely different shape compared to the run periods 2-4. The calibration factors vary with a sinusoidal shape. It is assumed that this behavior is an artefact of data taking problems in the first run period. It is not reproduced by the Monte Carlo simulation.

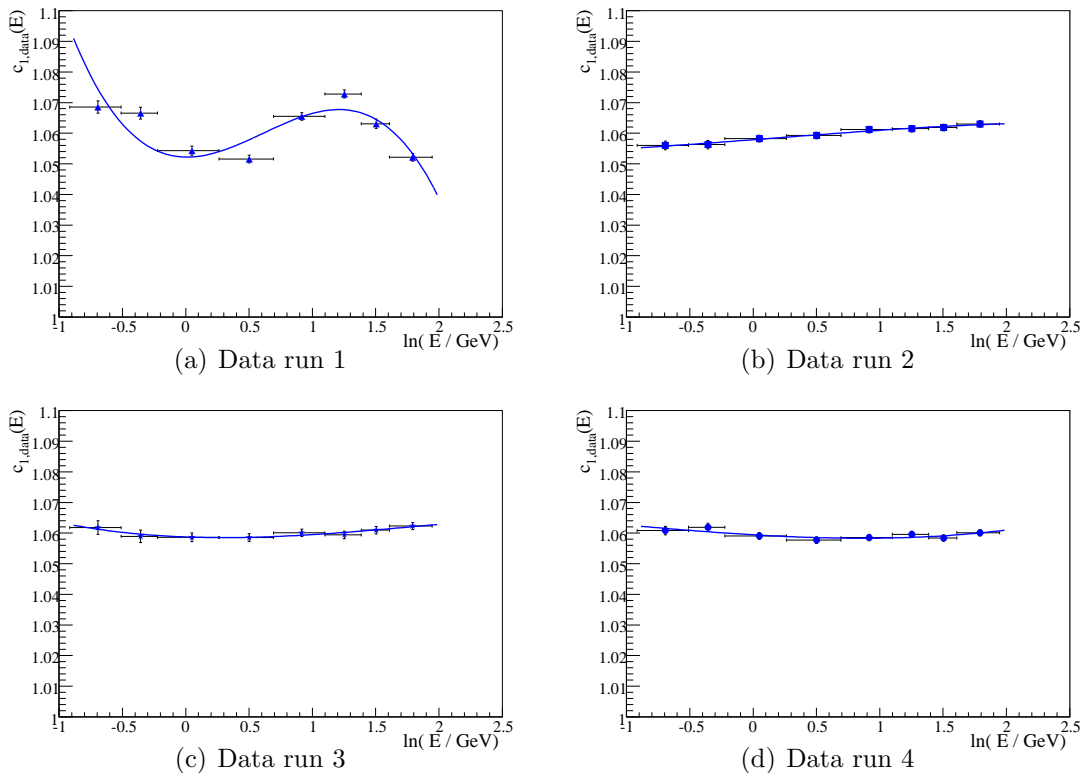


Figure 5.8: Energy dependent calibration factor for data, $c_{1,data}(E)$. The double ratio according to Eq. 5.5 is drawn as a function of the logarithm of the energy. Significant differences between the runs are seen, the obtained calibration factors for run 1 show variations of 1.5%.

The third order polynomial fit describes the data points for the run periods 2-4 very well. Run period 1 has to be treated differently. The calibration function is defined piecewise: The first and the last bin are set constant to the value of the

calibration factor determined for particular bin. The fitted polynomial is used for the inner bins.

Polar Angle Dependence

In order to determine the polar angle dependent calibration function $c_{2,data}^E(\theta)$ in data, the energy dependent calibration function $c_{1,data}(E)$ is applied first.

Fig 5.9 shows the calibration factors $c_{2,data}^E(\theta)$ as a function of the polar angle. The three energy ranges studied are indicated with colors: The lowest energy bin, 0.4 - 1.0 GeV, is drawn in blue, the middle bin 1.0 - 2.0 GeV in red and the high energy bin, 2.0 -4.0 GeV in green.

A clear dependence on the polar angle is seen throughout all four run periods. The variation of the calibration function over θ is 2.5% in the run periods 3 and 4, 2% in the second run period and up to 5% in the first run period. An energy dependence is seen as well.

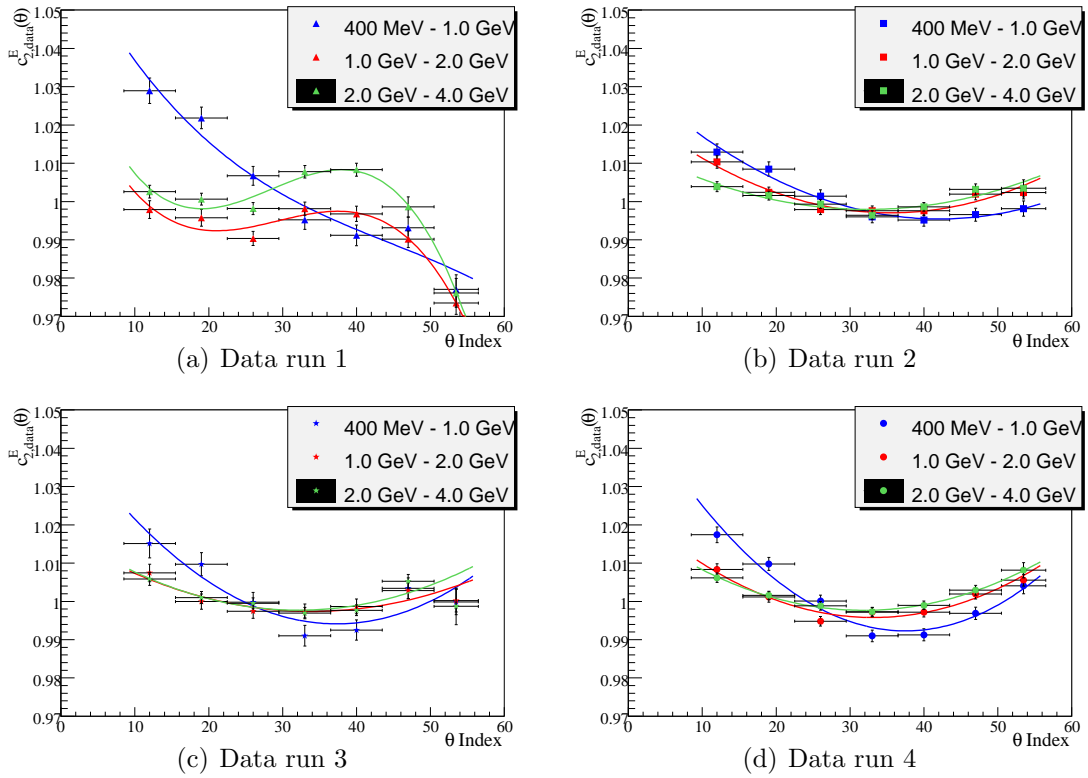


Figure 5.9: Polar angle dependent calibration factor for data, $c_{2,data}^E(\theta)$. The double ratio according to Eq. 5.5 is shown as a function of the crystal index in θ . The figures (a) - (d) show the four different run periods. A change of the calibration factor between the runs as well as an energy dependence is seen.

The shape of the polar angle dependence is similar in the run periods 2 - 4. The calibration function has maxima in forward and backward barrel (small and large I_θ respectively). The minimum depends on the energy range: In the lowest energy bin it is shifted backwards in comparison to higher energies. The rise in forward direction is increases with decreasing energy.

The shape in the first run period is completely different. It has a maximum in forward direction, relative maxima and minima in between and drops down in backward direction. The energy dependence of $c_{2,data}^E(\theta)$ is on the level of several percent, *i.e.* larger than the overall variation over the θ in the other run periods. As well as in the discussion of the energy dependence, the different behavior of the first data taking period is assumed to be an artefact of a different configuration of the *BABAR* detector.

Over all four run periods, the three different energy ranges of $c_{2,data}^E(\theta)$ differ significantly. Thus, the calibration function in data does not factorize.

The Monte Carlo simulation does not reproduce the difference between the calibration functions on a scale of several percent, depending on the run period. The energy dependence of the calibration function $c_{2,data}^E(\theta)$ is not reproduced by the simulation either.

5.2.4 Test of the Calibration

The cluster energy calibration for data is obtained as the product of the energy and the θ dependent parts of the calibration function: $c_{data} = c_{1,data}(E) \cdot c_{2,data}^E(\theta)$. In order to test the calibration, the parameterization is applied. Thus, a double ratio similar to Eq. 5.5 is defined,

$$\Delta_E^{peak} = \frac{peak(E_{cal}^{MC} / E_{fit}^{MC})}{peak(E_{cal}^{data} / E_{fit}^{data})}, \quad (5.9)$$

where E_{cal} denotes the cluster calibrated energy for data and Monte Carlo respectively and E_{fit} the energy calculated with the kinematic fit. The ratio of the peaks of the two distributions is taken.

The double ratio Δ_E^{peak} is expected to be at 1.0 over the whole energy range and over the polar angle if the cluster energy is well calibrated. It was shown in section 5.2.2 that the calibrated Monte Carlo cluster energy reproduces the correct energy scale within a statistical uncertainty of 0.1%. Therefore, possible deviations of Δ_E^{peak} from 1.0 have to be due to a not correctly calibrated cluster energy in data.

The double ratio Δ_E^{peak} is shown in Fig. 5.10 for the four run periods. In the subfigures (a) - (d) the double ratio is taken as a function of the energy, in the subfigures (e) - (h) as a function of the polar angle. The double ratio of the calibrated energies shows no dependence on energy, polar angle or run period. A remaining difference of the description of the data by the simulation is of the order of 0.1% for the run periods 2 to 4 and 0.5% for run period 1.

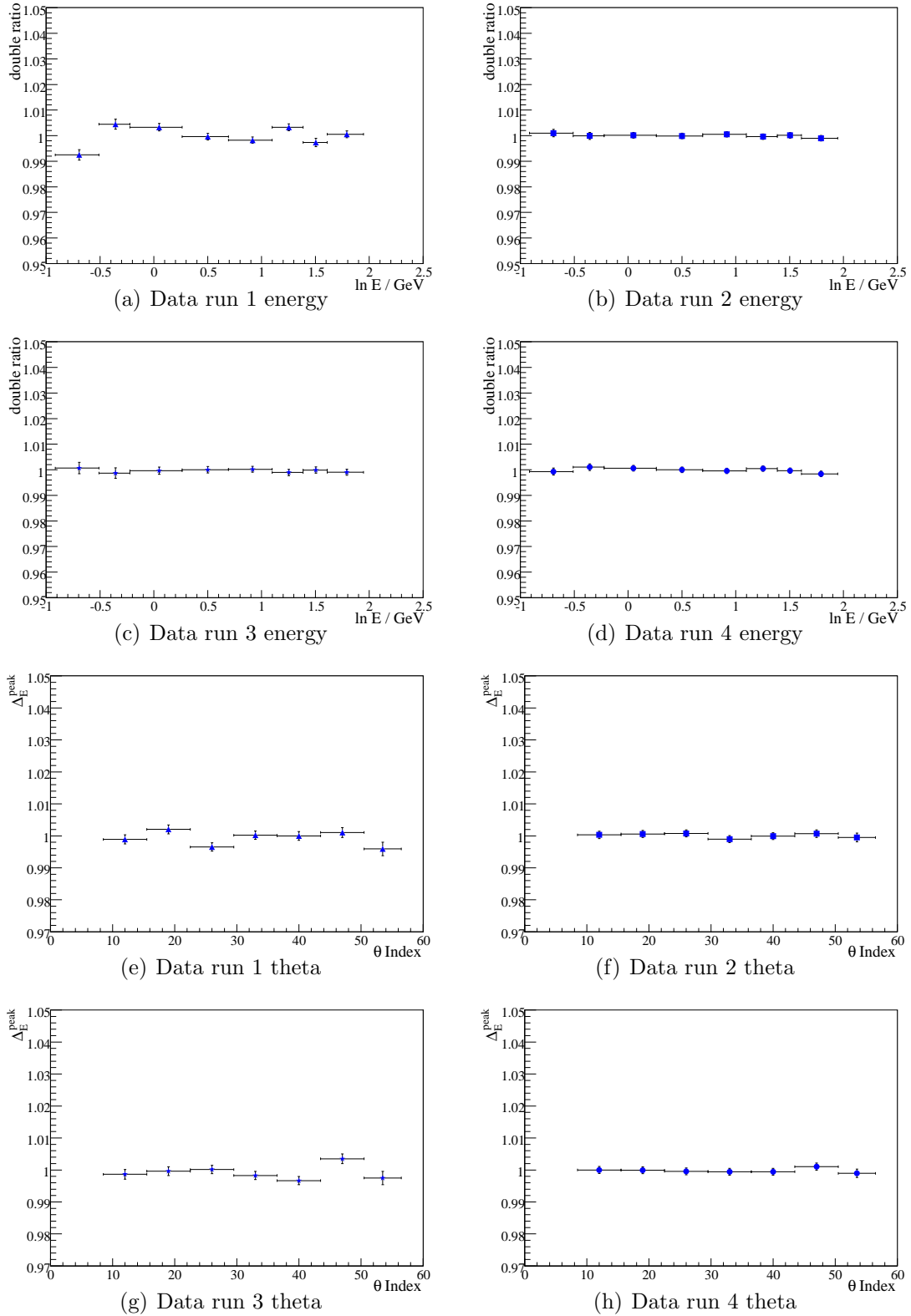


Figure 5.10: (a) - (d): Double ratio Δ_E^{peak} as defined in Eq. 5.9 as a function of $\ln(E)$. The calibrated cluster energy peaks at 1.0 with deviations of the order of 0.1% and 1% for the run periods 2-4 and 1 respectively. (e) - (h): Δ_E^{peak} as a function of θ . The cluster energy is calibrated to a level of 0.2% and 0.5% for the run periods 2,4 and 1,3 respectively.

The dependence on polar angle scatters more, but no systematic dependence can be seen. The deviations of the double ratio from 1.0 are of the order of 0.2% for the high statistics run periods 2 and 4 and 0.4% for the low statistics run periods 1 and 3. These deviations are well within the statistical significance of the calibration factors.

The energy calibration obtained from $\mu\mu\gamma$ events works reliably for the energy range of 400 MeV to 7 GeV. The energy dependence of the calibration factors in the polar angle seen in data is not described by Monte Carlo. The calibration corrects for it.

Systematic studies of the calibration factors are presented in the next section.

5.3 Systematic Studies of the Calibration

The calibration method using $\mu\mu\gamma$ events relies on the quality of the Monte Carlo detector simulation describing the data. In addition to the studies presented in section 4.4, several other sources of systematic uncertainties will be studied in this section.

Firstly, the width and asymmetries of the distributions involved are discussed. Next, the constraint that the particles involved in the kinematic fit originate from the beam spot, the momentum measurement in the drift chamber as well as the determination of the beam parameters are studied. Before concluding with a summary of the systematic uncertainties, the uncertainty introduced by the algorithm to determine the peak position is analyzed.

5.3.1 Shape of the Distributions in Data and Simulation

In the calibration, the double ratio simulation over data of the ratios reconstructed over fitted energy as defined in Eq. 5.5 is used to determine the calibration factor. For both data and simulation, the ratio of two distributions with finite resolution is taken. The peak position depends on:

1. the width of the calculated energy, $\sigma(E_{fit})$,
2. the asymmetric number of events outside the central area of the distribution in the calculated energy, $\tau(E_{fit})$,
3. the width of reconstructed energy, $\sigma(E_{raw})$ and
4. the asymmetric number of events outside the central area of the distribution in the reconstructed energy, $\tau(E_{raw})$.

It is well known that the width and the number of entries outside the central area of the distribution are different in data and simulation (see Fig. 5.2). The width of the distributions contributing to the double ratio is studied first. The double ratio

$$\Delta_E^{FWHM} = \frac{FWHM(E_{raw}^{MC}/E_{fit}^{MC})}{FWHM(E_{raw}^{data}/E_{fit}^{data})} \quad (5.10)$$

is defined, where the full-width-half-maximum of the specified ratios is determined. It gives the deviation in width between data and simulation. Observed differences can originate either from differences in the reconstructed energy between data and simulation or from differences in the fitted energy. Given the available information, these two possibilities cannot be distinguished. However, the input quantities of the photon calculation are known to agree on a level of better than 0.1% (see section 4.7.1).

As shown in section 5.2.3, the peak positions of the reconstructed energy in the simulation differs from the data values by about 1%. The double ratio Δ_E^{FWHM} is corrected for this.

The double ratio Δ_E^{FWHM} is shown in Fig. 5.11 as a function of the energy. Within the significance, no energy dependence is seen. The average deviations between data and simulation are approximately 15% in the run periods 2 to 4 and approximately 25% in run period 1.

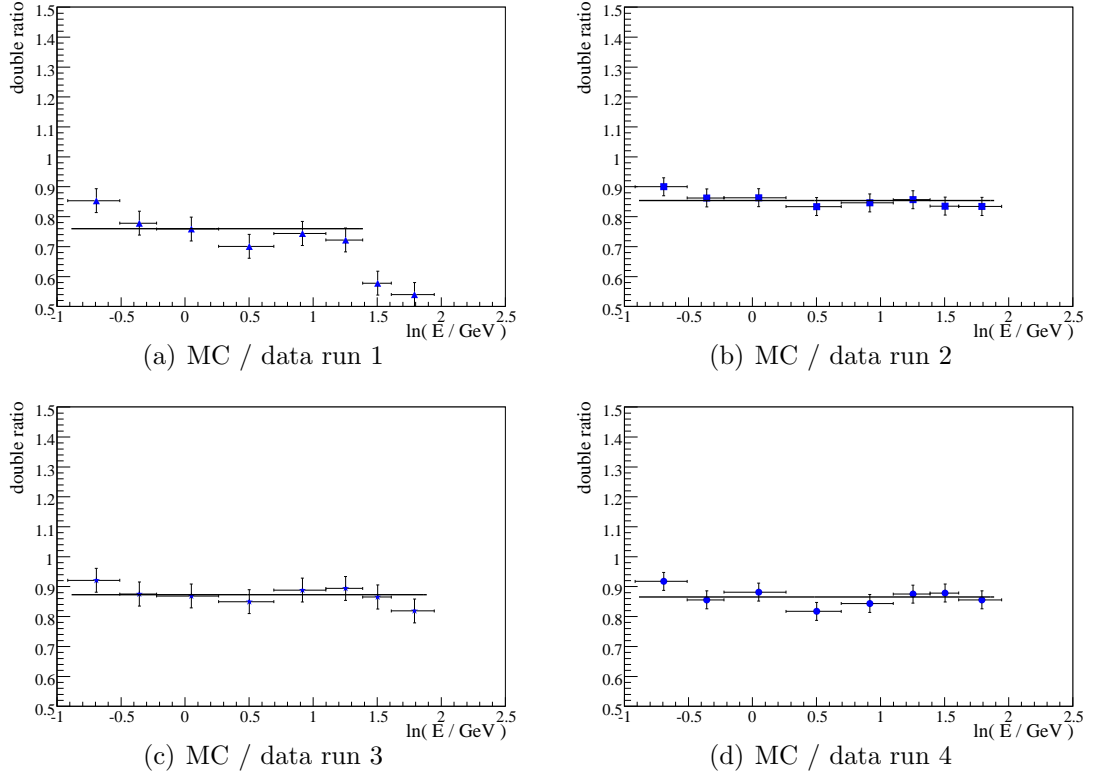


Figure 5.11: Corrected double ratio of the width, Δ_E^{FWHM} as defined in Eq. 5.10. The width is in the simulation over all run periods 15 - 25 % smaller than in data.

The better energy resolution in the simulation is not understood. It may be due to

1. an underestimation in the detector simulation of the material distribution in front of the EMC or
2. the cutoff implemented in the simulation of low energetic photons may not perfectly be tuned.

The implications of this difference on the calibration factor will be studied at the end of this section.

Furthermore, the asymmetric τ of the distributions contributing to the double ratio influence the peak position of E_{raw}/E_{fit} . The estimate by the kinematic fit has an asymmetric number of entries outside the central part. Therefore, the asymmetries of the raw energy cannot be studied using the ratio E_{raw}/E_{fit} . In order to give an estimate of the effect of the outliers on the calibration factor, a difference of 15% between data and simulation is assumed.

Effects on the Calibration Factor

The effect of differences between the response function of the EMC and the simulation can be studied using a toy Monte Carlo simulation [23]. The energy response of photons is parameterized using a single photon simulation. This parameterization allows to change the response, specially the contributions of events outside the central area and of the resolution. The effect of changes in the quantities $\sigma(E_{fit})$, $\tau(E_{fit})$, $\sigma(E_{raw})$ and $\tau(E_{raw})$ on the calibration factor can be simulated. By this, a correction for the measured resolution difference of 15% between data and simulation is determined. The energy dependent correction function $\delta^{syst}(E)$ is shown in Fig. 5.12. The corrections are only significant in the energy range below 1 GeV. These corrections reflect the differences in the description of the data by the Monte Carlo simulation and have to be applied to the calibration function for data obtained from the $\mu\mu\gamma$ dataset.

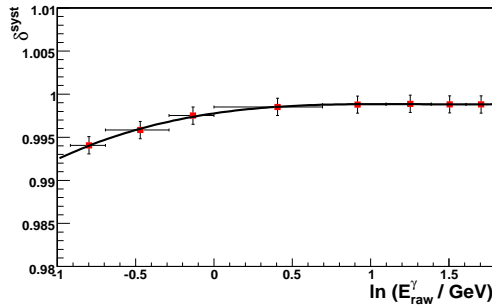


Figure 5.12: Total correction δ^{syst} for the calibration factor $c_{data}(E, \theta)$. The correction is at maximum 0.6% [24].

5.3.2 Charged Particle Measurement

The photon four vectors are calculated using the kinematic fit without any calorimeter information. The four vectors of the muons as well as the beam parameters are used as input quantities.

The muon momentum is measured in the tracking system, as discussed in section 3.2.2. The quality of the simulation describing the data is better than 0.1% (see section 4.7.1). It can be concluded that besides the effect due to the

finite tracking resolution, which is taken into account by the calibration scheme, there is no bias of the kinematic fit due to the momentum measurement.

The second input of the kinematic fit is the beam information. The beam parameters are known up to 0.07 and 0.06% for the low energy ring and the high energy one respectively (section 4.7.1). This precision is better than the one achieved in the tracking devices. The influence of the uncertainties of the beam parameters does not lead to any systematic effects seen in the kinematic fitting of the photon energy.

5.3.3 Uncertainty in Beam Spot

The kinematic fit uses the constraint that all particles must originate from the beam spot. In data, the beam spot is determined by averaging the event vertices of each machine run. In the simulation, however, the beam spot is fixed to one point. Hence, the influence of these differences needs to be studied. In data, the RMS spread of the beam spot is about 100 μm along the beam axis and a few μm transverse to it.

The change of the peak position of E_{fit}/E_{true} with a variation of the beam spot is studied. In the test performed here, the beam spot is shifted for each event by 2 and 5 standard deviations respectively.

Since it was necessary to reprocess the data with a shifted beam spot, the tests in this section are performed using a sample with less events than those used for the calibration. The sample was chosen such that the peak position is well defined.

In Fig. 5.13 the peak position of E_{fit}/E_{true} is shown as a function of the energy. In Fig. 5.13 (a) the beam spot is shifted in direction of the beam axis and in (b) perpendicular to it by two and five standard deviations respectively. Within the statistical uncertainties, no influence on the peak position of the variations of the beam spot is seen.

It can be concluded that systematic uncertainties in the determination of the beam spot would not result in a bias of the kinematic fit.

5.3.4 Peak Fit Procedure

The algorithm to determine the peak position of the distributions used for the calibration is described in section 4.6. The range of the fit region is limited. The systematic uncertainty introduced by this specific algorithm can be estimated with variations of the fit procedure. The peak position changes by maximally 0.1% with variations of the peak determination algorithm. The systematic error of the calibration factors is minimized because they are measured as ratio of two quantities where the method to determine the peak position is the same.

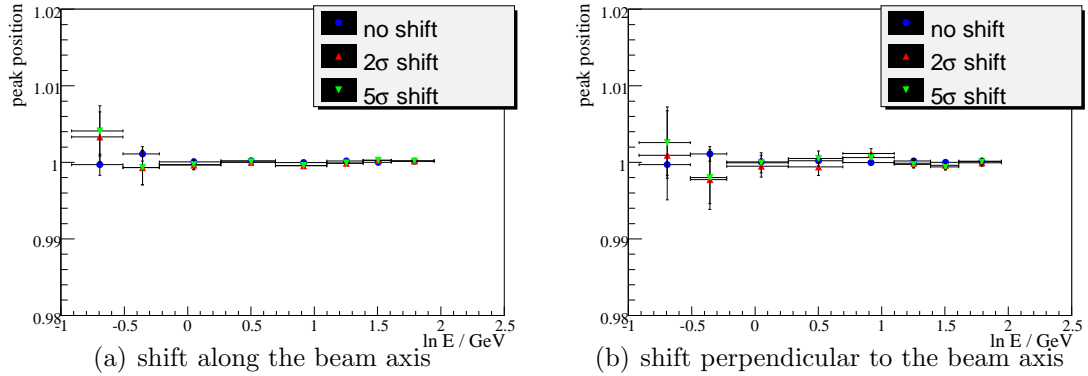


Figure 5.13: Peak position of E_{fit}/E_{true} as a function of the generator energy. The peak position is shown with no variation in blue circles, with a variation of 2σ in red triangles and in green triangles for a variation of 5σ . No significant change is seen.

5.3.5 Summary of Systematic Uncertainties

The systematic uncertainties in the determination of the calibration function have been estimated. They are found to be as follows:

- The influence of differences in the response function of the EMC on the calibration function is determined from variations as described in section 5.3.1. The unmeasured τ is assumed vary within 15%, the uncertainty in the determination of the resolution is 3%. Within these changes, the calibration function changes by maximally 0.2%. This is taken as systematic uncertainty due to differences in the response function between data and simulation.
- The contribution from the muon momentum measurement is below 0.1%.
- Variations in the beam spot give within the significance no effect on the fit estimate.
- The systematic uncertainty originating from the peak fit determination was found to be 0.1%.

The single contributions to the systematic uncertainty are added quadratically since they are assumed to be uncorrelated. This yields in a total systematic uncertainty of 0.3% which is added quadratically to the statistical uncertainties.

5.4 Energy Resolution

Using the $\mu\mu\gamma$ data sample, the energy resolution of the EMC can be measured for high energy photons. The energy resolution $\sigma(E)/E$ of the calorimeter is assumed to be of the form (see section 3.3.1 for a discussion of this parameterization)

$$\frac{\sigma(E)}{E} = \left(\frac{a}{\sqrt[4]{E/\text{GeV}}} \oplus b \right) \%, \quad (5.11)$$

where a and b are the coefficients for the energy dependent and the constant term respectively. Both terms are added quadratically.

The energy resolution can be determined from the width of the distribution of E_{cal}/E_{fit} . However, the resolution of E_{fit} due to the uncertainties in the tracking measurement has to be taken into account. This is studied in the simulation in Fig. 5.14. The full-width-half-maximum of the distributions of E_{cal}/E_{true} , which is the energy resolution of the calorimeter, and E_{cal}/E_{fit} , which is the energy resolution convoluted with the fit resolution are shown.

For energies below 2 GeV, the estimate using the fitted energy is wrong by more than 1.5%. At energies between 2 and 3 GeV, it is too high by 0.3% and above this energy the contribution of the fit resolution is negligible. The energy resolution is determined for photon energies above 2 GeV. In the energy range of 2 to 3 GeV, an systematic uncertainty of 0.3% is added.

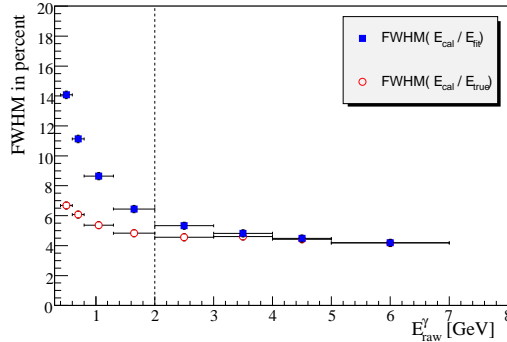


Figure 5.14: *FWHM of the distributions of E_{cal}/E_{true} and E_{cal}/E_{fit} in red circles and blue squares respectively. For low energies, the fit contribution is clearly seen. The energy resolution is reasonably well described above 2.0 GeV.*

The energy resolution is defined as the sigma of the distribution, *i.e.* as

$$\sigma = \frac{FWHM\left(\frac{E_{cal}}{E_{fit}}\right)}{\sqrt{4\ln(4)}}, \quad (5.12)$$

where FWHM denotes the full-width-half-maximum of the distribution. The factor $\sqrt{4\ln(4)}$ originates from the relation between the FWHM and sigma of a normal distribution.

In Fig. 5.15 (a) the energy resolution obtained from the $\mu\mu\gamma$ dataset is shown as a function of the energy. A dashed line indicates the energy above which the measurements are used to determine the resolution. The resolution is determined by a fit of a function of the type of Eq. 5.11. It is only performed in the energy range above 2.0 GeV. The values obtained from the fit for data and Monte Carlo simulation are shown in the left hand side of table 5.2.

In Fig. 5.15 (b) the range used to fit the energy resolution is magnified. The parameterization given in an earlier EMC performance study (NIM paper) [1] is drawn in dashed line. Compared to this measurement, the resolution of the NIM parameterization is too large. The simulated energy resolution is somewhat better than the resolution of the reconstructed energy. This may be due to a wrongly simulated material distribution in front of the calorimeter.

However, it has to be emphasized that the resolution measurement at high energies is clearly not sufficient to determine a parameterization in energy dependent and constant term as discussed in section 3.3.1. In order to have a better handle on the energy dependence of the resolution, the $\mu\mu\gamma$ dataset has to be combined with low energy measurements. A possible candidate is the decay of the Σ baryon, work in this area is in progress [17].

Dataset		This measurement	NIM parameterization
Data	a [%]	2.74 ± 0.61	2.32 ± 0.30
	b [%]	0.57 ± 1.45	1.85 ± 0.12
Simulation	a [%]	2.73 ± 0.09	
	b [%]	0.0 ± 2.07	

Table 5.2: *Energy resolution determined in this measurement and parameterization given in the NIM paper [1].*

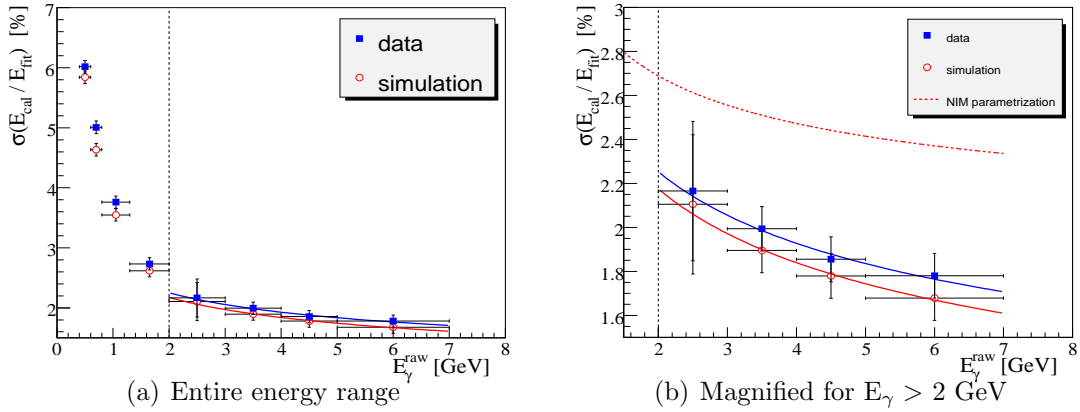


Figure 5.15: The energy resolution is shown as a function of the energy. A dashed line indicates the region above which the fit bias is negligible. (a) over the full range covered by the $\mu\mu\gamma$ dataset. (b) zoomed into the region where the fit is done. The parameterization according to the NIM paper is drawn in as well (b).

5.5 Summary

For the first time in the *BABAR* experiment, a cluster energy calibration for energies above 1.5 GeV was derived from physics processes. Kinematically constrained photons from the reaction $e^+e^- \rightarrow \mu^+\mu^-\gamma$ are used for the calibration. The dependence on energy and polar angle is calibrated separately for the four different periods of data taking. The calibration technique uses the uncalibrated data which is normalized to the calibrated response in the simulation. This algorithm takes the finite resolution of the calculated energy into account. The obtained calibration function reproduces the correct energy within a statistical uncertainty of 0.1 - 0.4% for the energy range up to 7 GeV.

Systematic effects of the $\mu\mu\gamma$ calibration scheme have been studied. As an important aspect, the width of the reconstructed over the fitted energy was found to be 15 - 25 % smaller in the Monte Carlo simulation than in data. The effect of this difference on the calibration factor was studied and a correction applied. The overall systematic error was found to be 0.3%.

The energy resolution of the calorimeter has been determined in the energy range of 2 - 7 GeV. In data, it was measured to be

$$\frac{\sigma(E)}{E} = \left(\frac{(2.74 \pm 0.61)}{\sqrt[4]{E/\text{GeV}}} \oplus (0.57 \pm 1.45) \right) \%. \quad (5.13)$$

In the simulation, the energy resolution has been determined the same way as in

data. It was found to be

$$\frac{\sigma(E)}{E} = \left(\frac{(2.73 \pm 0.09)}{\sqrt[4]{E/\text{GeV}}} \oplus (0.0 \pm 2.07) \right) \%. \quad (5.14)$$

which is better than the resolution in data. However, as seen in the large errors, the high energy part measured with $\mu\mu\gamma$ events is not sufficient to determine the parameterization in a constant and an energy dependent part.

The cluster calibration scheme using $\mu\mu\gamma$ events is to be combined with the cluster calibration obtained from neutral pion decays which covers the low energy spectrum. For the combination of the $\mu\mu\gamma$ and the π^0 calibration, systematic effects in both datasets have to be studied carefully. For the $\mu\mu\gamma$ dataset, this has been discussed in section 5.3.

Neutral pions are reconstructed from two photons. At photon energies below 0.7 GeV, the resolution of the reconstructed invariant mass of the π^0 is dominated by the energy resolution. At higher photon energies, the position measurement dominates. Hence, a possible bias in the position reconstruction of photons results in a systematic error in the cluster energy calibration function of the π^0 calibration in the energy range above 0.7 GeV. The $\mu\mu\gamma$ dataset can also be used to study the position reconstruction of photons in the calorimeter. This is discussed in the next section.

Chapter 6

Photon Position Reconstruction

One of the tasks of the electromagnetic calorimeter is the position measurement of photons which is the topic of this chapter. Data from the fourth run period of data taking and the associated Monte Carlo simulation is used in this chapter if not stated differently.

After a discussion of the position reconstruction algorithm, the dependence of the position reconstruction on the polar angle is studied on a large scale, not looking at structures inside single crystals. Afterwards, systematic deviations of the reconstructed to the true photon position inside single crystals are analyzed and a correction scheme for these deviations is developed.

Any bias in the position measurement could result in systematic shifts of kinematic variables, *e.g.* four vectors of neutral pions, and introduce systematic shifts in physics results. Therefore, possible biases have to be studied carefully and must be corrected if possible.

6.1 Position Reconstruction Algorithm

In general, the shower induced by a photon entering the calorimeter spreads over many crystals. Since the *BABAR* calorimeter is not longitudinally segmented, only the transverse position of the photon can be measured. A weighted average of the crystal position in a shower is used to determine the transverse position. The weight with which a crystal enters depends on the energy the shower deposits in it. Several different approaches exist for the weighting model:

The easiest ansatz is to use a linear weighting model. The position \vec{x} of a photon is reconstructed to be

$$\vec{x} = \sum_{i=1}^n \vec{x}_i \frac{E_i}{\sum_{j=1}^n E_j}, \quad (6.1)$$

where \vec{x}_i denotes the central position of the crystal front face in which the energy E_i is deposited in. The sum includes all crystals of the cluster.

A different approach, the logarithmic weighting, reduces the weight of the most energetic crystals and enhances the lower energy ones. It takes the exponential structure of the shower in transverse direction into account. The position \vec{x} of the photon gets reconstructed as¹

$$\vec{x} = \sum_{i=1}^n \vec{x}_i \max(0, a + \ln(\frac{E_i}{\sum_{i=1}^n E_i})). \quad (6.2)$$

The sum includes all crystals of the cluster, a is the cutoff parameter which guarantees that the logarithm gets a positive argument and removes crystals with very low energy.

The position reconstruction algorithms can be studied in the simulation. Fig. 6.1 compares the linear and the logarithmic weighting function used for position reconstruction. In the case of linear weighting, Fig. 6.1 (a), the reconstructed polar angle (θ_{emc}) drawn as a function of the generated value (θ_{true}) has a big tilt compared to the ideal correlation line. In contrast to that, the logarithmic weighting, Fig. 6.1 (b), has a much smaller systematic deviation from the ideal correlation.

The algorithm used in the *BABAR* experiment for position reconstruction was optimized in single photon Monte Carlo [18]. Logarithmic weighting with a cutoff parameter of $a = 4.0$ is used for data production. That means, only crystals with a deposited energy of more than 1.8% of the total cluster energy are considered to calculate the photon position.

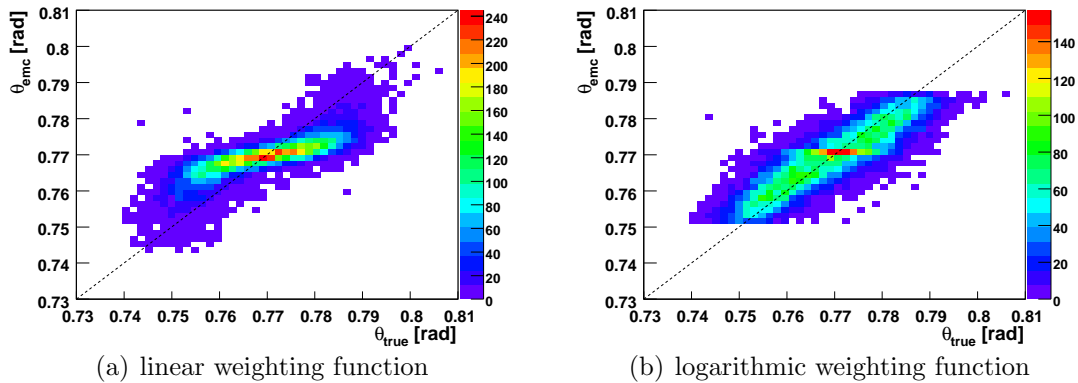


Figure 6.1: Simulation with $I_\theta = 19$ and $0.4 < E_\gamma < 2.0$ GeV. In the linear weighting (a), the reconstructed and the true position are not as well correlated as in the logarithmic weighting (b). [25]

Fig. 6.2 shows the number of crystal rings² contributing to the photon position reconstruction in the $e^+e^- \rightarrow \mu^+\mu^-\gamma$ dataset. For the polar angle determination,

¹The algorithm described in Eq. 6.1 and Eq. 6.2 reconstructs the cluster position two-dimensionally. The radial component is fixed to be 12.5 cm.

²More precisely: The number of different indices in θ and ϕ respectively.

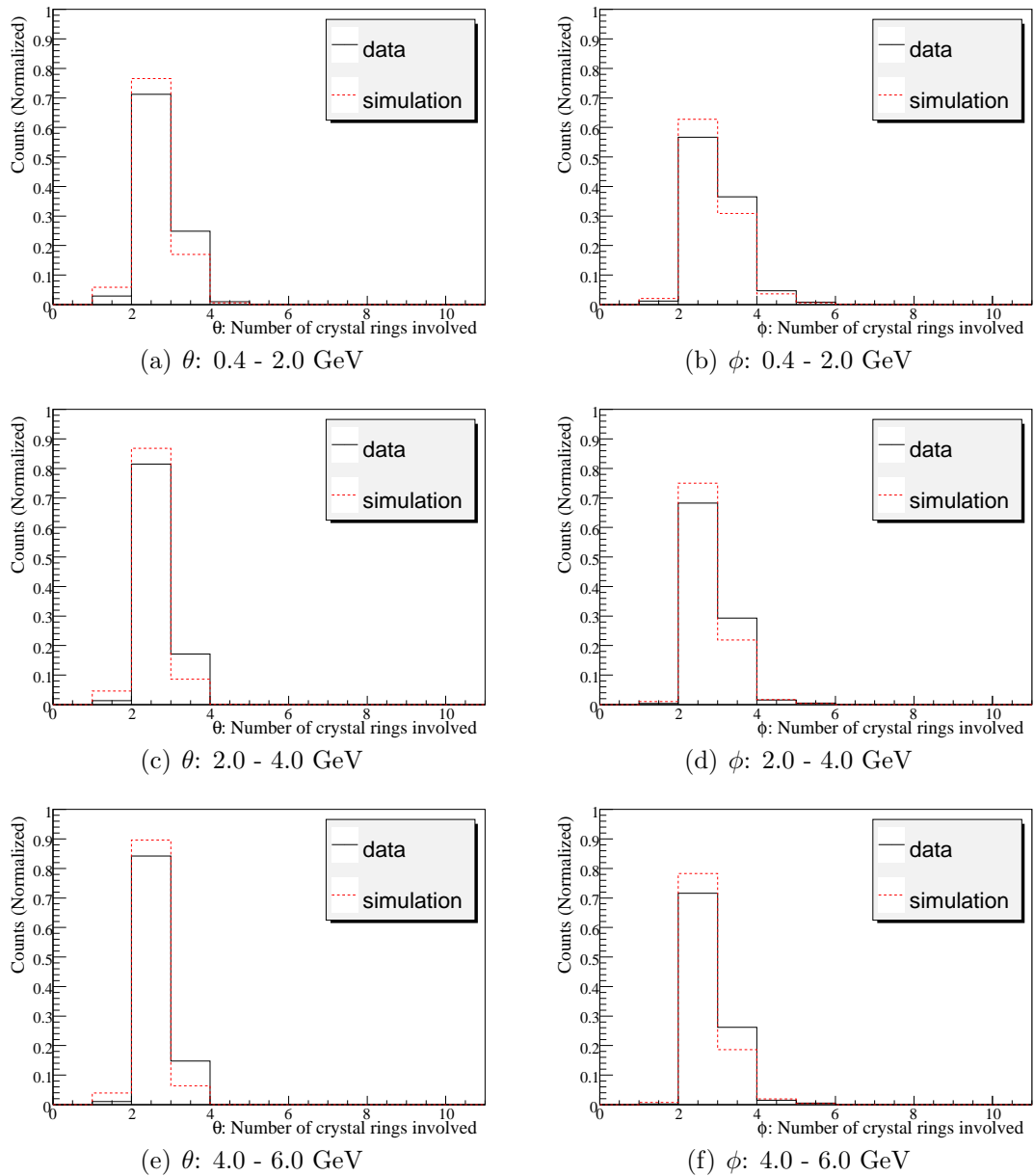


Figure 6.2: Number of crystal rings per cluster above the 1.8% threshold used for position reconstruction. The number of crystals is shown in θ and ϕ as well as in different energy bins.

there is a significant number of events with only one crystal above cutoff in one direction. For these crystals the reconstructed position is set equal to the crystal center. This results in an artificial peak at the crystal center (seen in Fig. 6.1). There are more events with one crystal in the simulation than in data.

6.1.1 Position Estimate Using the Kinematic Fit

For $\mu\mu\gamma$ events, the position of the photon can be calculated using the kinematic fit. As shown in section 4.7.4, θ_{fit} is reproducing the generated value with good accuracy.

The correlation of the angle calculated with the kinematic fit is shown as a function of the generated value in Fig. 6.3. The crystal rings with indices $I_\theta = 20 - 25$ are chosen as an example. This corresponds to the central part of the barrel. A diagonal line of ideal correlation (where $\theta_{fit} = \theta_{true}$) and crystal boundaries are drawn as well. No crystal structure is seen. The angular estimate of the kinematic fit has entries outside the central area to high and low angles.

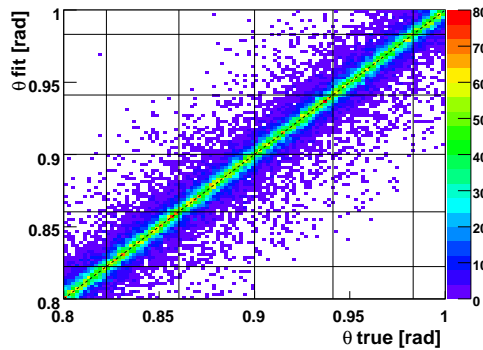


Figure 6.3: Estimate of the kinematic fit (θ_{fit}) as function of the generated angle, (θ_{true}). No crystal structure is seen.

6.2 Position Reconstruction on Module Level

Two different aspects of the position reconstruction are studied on a large scale, that means averaged over several crystals in azimuthal or polar angle. First, the quality of the angular reconstruction in data is compared with the simulation. Second, the angular resolution is studied.

6.2.1 Reconstructed Angles in Data and Simulation

The quality of the Monte Carlo simulation describing the position reconstruction in data is studied with the peak position of the distribution of reconstructed over the fitted polar angle ($\theta_{emc}/\theta_{fit}$). In order to avoid systematic deviations due to

the finite fit resolution (see discussion in section 5.2.2), the double ratio Δ_{θ}^{peak} is defined in analogy to Eq. 5.5,

$$\Delta_{\theta}^{peak} = \frac{peak(\theta_{emc}^{MC}/\theta_{fit}^{MC})}{peak(\theta_{emc}^{data}/\theta_{fit}^{data})}, \quad (6.3)$$

where θ_{emc} is the position reconstructed using the weighted mean discussed in section 6.1 and θ_{fit} is the estimate for the photon polar angle from the kinematic fit for data and simulation respectively. In Fig. 6.4, the double ratio as defined in Eq. 6.3 is shown as a function of the θ index for all four run periods. The position is reconstructed with deviations between data and simulation of less than 0.5% in forward barrel and deviations of the order of 0.1% in the central and backward barrel.

It has to be emphasized that this shows only the accuracy to which the simulation describes the data. This does not imply that the absolute scale is determined to the same accuracy.

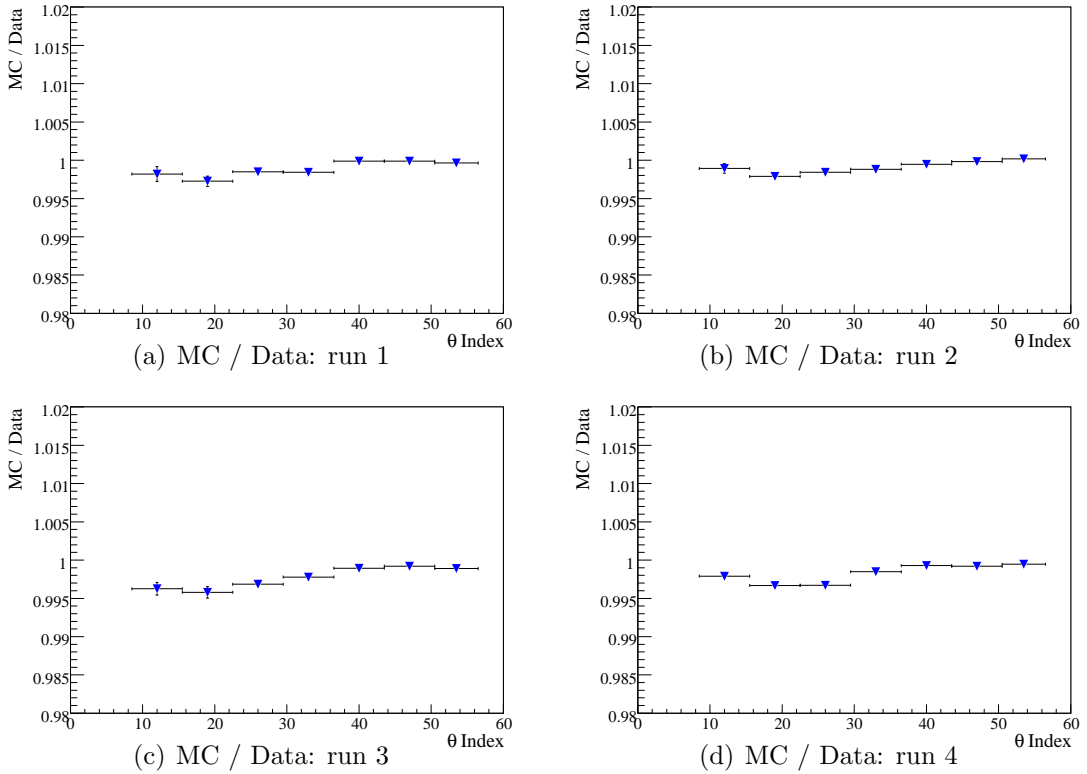


Figure 6.4: Ratio of simulation over data: Δ_{θ}^{peak} as defined in Eq. 6.3 for all four run periods. Deviations between simulation and data of smaller than 0.5% are seen.

6.2.2 Position Resolution

To measure the resolution, the difference

$$\theta_{ef} = \theta_{emc} - \theta_{fit} \quad (6.4)$$

of the reconstructed angle (θ_{emc}) and the angle calculated with the kinematic fit (θ_{fit}) is studied. This results in a distribution which has a peak value around zero. The angular resolution $\sigma(\theta_{ef})$ is then defined as the full-width-half-maximum of θ_{ef} over 2.355 (analogue to section 5.4).

Unfolding the Resolution of the Fitted Angle

The photon position as obtained from the kinematic fit has a finite resolution. Similarly to the energy measurement in chapter 5.2.3, the fit resolution improves with increasing energies. Compared to the energy measurement, the situation here is much simpler: The resolution distributions are to a good approximation symmetric (see Appendix B) and can be described by a Gaussian. The width of $\theta_{ef} = \theta_{emc} - \theta_{fit}$ is a convolution of the resolution of the calorimeter $\sigma(\theta_{et})$ and the resolution of the kinematic fit $\sigma(\theta_{ft})$. Assuming Gaussian error propagation, $\sigma(\theta_{ef})$ can be written as

$$\sigma(\theta_{ef}) = \sqrt{\sigma(\theta_{et})^2 + \sigma(\theta_{ft})^2}, \quad (6.5)$$

where $\theta_{et} = \theta_{emc} - \theta_{true}$ and $\theta_{ft} = \theta_{fit} - \theta_{true}$. The measured resolution of the calorimeter, $\sigma^{EMC}(\theta)$, can be obtained from the width of θ_{ef} by subtracting the fit resolution quadratically,

$$\sigma^{EMC}(\theta) \approx \sqrt{\sigma(\theta_{ef})^2 - \sigma(\theta_{ft})^2}, \quad (6.6)$$

where $\sigma(\theta_{ef})$ is measured in both data and simulation separately and $\sigma(\theta_{ft})$, the fit resolution, is taken from the simulation. This assumes that the tracking resolution in data is described by the simulation. The quadratic subtraction remains an estimate since the resolution distributions are not entirely Gaussian.

The unfolding derived in Eq. 6.6 can be tested in the simulation. Ideally, the unfolded resolution $\sigma^{EMC}(\theta)$ would equal the calorimeter resolution $\sigma(\theta_{et})$. Fig. 6.5 shows $\sigma(\theta_{ef})$, $\sigma(\theta_{et})$ and the proper calorimeter resolution $\sigma^{EMC}(\theta)$ as a function of the energy.

$\sigma^{EMC}(\theta)$ is used to determine the resolution for energies above 1.3 GeV. The systematic error introduced by the unfolding is approximated from the difference between $\sigma(\theta_{et})$ and $\sigma^{EMC}(\theta)$. In the energy range of 1.3 to 2.0 GeV, it is assigned to be 1.5 mrad. For higher energies, the quadratic subtraction works better and a systematic error of 0.5 mrad is assigned.

In the following, the quadratic subtraction of the fit resolution is used to determine the angular resolution for the polar and azimuthal angle.

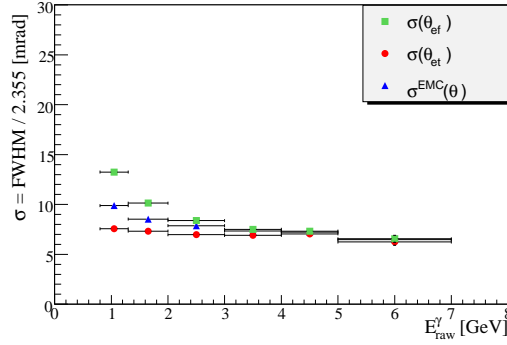


Figure 6.5: Study of $\sigma(\theta)$ Vs. energy for the central barrel in the simulation. The contribution of the fit resolution is clearly seen in $\sigma(\theta_{\text{ef}})$. The proper calorimeter resolution $\sigma^{\text{EMC}}(\theta)$ describes the true resolution reasonably well for energies above 1.3 GeV.

Resolution of the Polar Angle

In the calorimeter, the polar angle is not measured directly³. For physics analyses, the resolution of the measurement of azimuthal and polar angle are needed. By measuring $\sigma(\theta)$, a dependency on the distance r^{EMC} between the interaction point to the calorimeter is introduced,

$$\sigma(\theta) \approx \sigma(z)/r^{\text{EMC}}, \quad (6.7)$$

where $\sigma(\theta)$ and $\sigma(z)$ denote the resolution in angular and spatial measurement respectively. The distance r^{EMC} enhances or suppresses the measured quantities. The calorimeter is divided in four different areas with approximately equal distance r^{EMC} . As the calorimeter is constructed completely symmetric in ϕ , no dependence on the azimuthal angle is expected. Additionally, as described in section 3.3.2, the material distribution in front of the calorimeter differs significantly with polar angle.

In order to account for these effects, the calorimeter is divided into four sections in the polar angle. They are defined as follows:

1. Endcap: This includes the crystals with the θ crystal index $I_\theta = 1 - 8$
2. Forward barrel: This includes the first three modules in the EMC barrel, *i.e.* crystals with $I_\theta = 9 - 30$
3. Central barrel: This includes the next two modules in the EMC barrel, *i.e.* crystals with $I_\theta = 31 - 44$
4. Backward barrel: This includes the last two modules in the EMC barrel, *i.e.* crystals with $I_\theta = 44 - 56$

³ The quantities measured directly in the calorimeter are given by the symmetry of the detector, *i.e.* in cylindrical coordinates for the barrel (see section 3.3.2).

The energy dependence of the angular resolution is assumed to consist of an energy dependent and a constant part. It is parameterized as

$$\sigma(\theta) = \left(\frac{a}{\sqrt{E(\text{GeV})}} + b \right) \text{mrad}, \quad (6.8)$$

where a and b are determined separately for the four divisions of the calorimeter.

In Fig. 6.6 the measured angular resolution $\sigma^{EMC}(\theta)$ determined with the quadratical subtraction (Eq. 6.6) is shown as a function of the energy for data and simulation for the four divisions of the EMC. The resolution is determined from a fit of Eq. 6.8 to the measured points. The change of the resolution over the four divisions is dominated by the change of the distance to the interaction point.

The measured coefficients of the angular resolution can be found in table 6.1. The angular resolution is in all ranges in data better than in simulation. This is expected from the measurement of the shower width described in section 5.3.1: The position resolution of a crystal calorimeter depends on the *effective crystal size*, *i.e.* on the ratio of the crystal size to the shower width. Since the transverse shower size is smaller in the simulation, the *effective crystal size* is bigger and hence the position resolution is worse.

The errors determined from the fit are quite large since the systematic uncertainties introduced with the unfolding of the finite width are approximated conservatively.

EMC Region		Data	Simulation
endcap	a [mrad]	4.20±2.23	5.86±0.39
	b [mrad]	0.39±1.03	0±3.11
forward barrel	a [mrad]	8.75±2.89	10.12±0.49
	b [mrad]	0.05±1.91	0.0 ±2.27
central barrel	a [mrad]	5.17±3.60	6.86±3.74
	b [mrad]	4.88±1.79	5.07±1.83
backward barrel	a [mrad]	1.31±5.54	3.23±0.04
	b [mrad]	6.03±3.20	5.38±3.48

Table 6.1: Measured coefficients of the angular resolution in θ . The change over the divisions in the polar angle is dominated by the changing distance r^{EMC} .

Resolution of the Azimuthal Angle

The resolution of the azimuthal angular measurement $\sigma^{EMC}(\phi)$ is determined analogue to Eq. 6.6. Due to the change of material distribution over θ , the resolution of the azimuthal angle is determined in the same divisions as $\sigma^{EMC}(\theta)$.

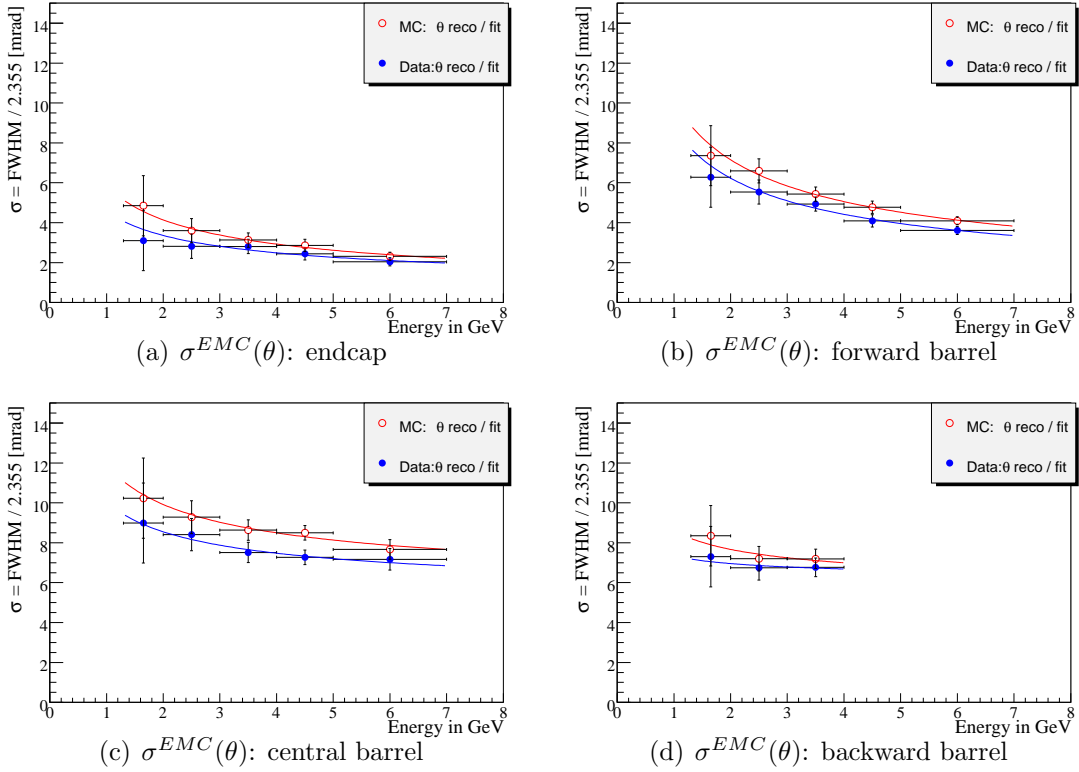


Figure 6.6: Measured resolution of the polar angle ($\sigma^{EMC}(\theta)$, Eq. 6.6) as a function of energy for data (full circles) and simulation (open circles). The four divisions of the EMC are shown as sub-figures (a) to (d). The change of the angular resolution over the polar angle is dominated by the change in r^{EMC} .

However, the calorimeter is symmetric in ϕ and thus no dependence on the location in the calorimeter is observed.

In Fig. 6.7, $\sigma^{EMC}(\phi)$ is shown as a function of the energy. The resolution is determined from a fit to the measured points. It is performed in the range of 1.3 to 7.0 GeV in the forward and central barrel and up to 4.0 GeV in the backward barrel. The limited range in the backward barrel is due to the photon phase space (see Fig 4.1). Table 6.2 shows the measured coefficients of angular resolution of the azimuthal angle.

Given the large errors of the parameterizations, no significant change of $\sigma^{EMC}(\phi)$ with the divisions is observed. Within the significance, the simulation describes the resolution in data. It is not completely understood why the clear difference between the simulation and data seen in the polar angle is not observed in the azimuthal angle. A hint to understand this may be the bigger difference in the number of crystals used for position reconstruction between data and simulation (Fig. 6.2).

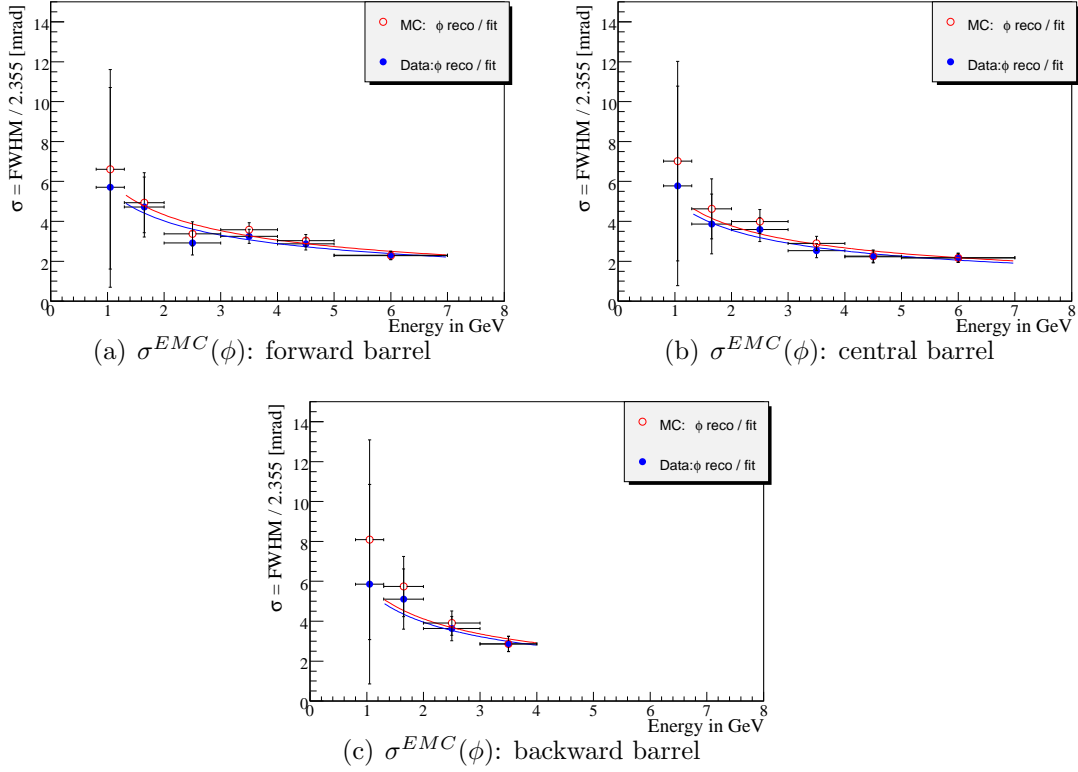


Figure 6.7: Measured resolution of the azimuthal angle $\sigma^{EMC}(\phi)$ as a function of energy for data and simulation. The sub-figures (a) - (c) denote the different divisions of the barrel part of the calorimeter. The simulation describes the data within the significance.

EMC Region		Data	Simulation
forward barrel	a [mrad]	5.48 ± 2.51	6.12 ± 0.40
	b [mrad]	0.14 ± 2.44	0.0 ± 0.97
central barrel	a [mrad]	5.03 ± 0.38	5.33 ± 0.38
	b [mrad]	0.0 ± 2.07	0.0 ± 0.68
backward barrel	a [mrad]	5.59 ± 0.63	5.82 ± 0.64
	b [mrad]	0.0 ± 2.56	0.0 ± 1.40

Table 6.2: Measured coefficients of the angular resolution in ϕ . The resolution is within the significance equal between data and simulation as well as for the divisions of the EMC.

6.3 Position Measurement Inside Single Crystals

In this section, deviations of the reconstructed to the true photon position inside single crystals are studied. This can be done independently for data and simulation using θ_{fit} . Therefore, a possible correction can be obtained separately for both datasets using the same method.

6.3.1 Qualitative Discussion

Using Generator Level Information

In order to study the sub-crystal position measurement, the angle reconstructed in the calorimeter (θ_{emc}) is compared with the generated angle (θ_{true}) as shown in Fig. 6.8. Ideally, one would expect a diagonal line washed out with the resolution. However, as already seen in Fig. 6.1, the position reconstruction algorithm introduces a systematic deviation depending on the position relative to the edges of the crystal.

The reconstructed polar angle, correlated with the true angle in the simulation is shown in Fig. 6.8. Crystals with indices $I_\theta=20-25$ are chosen as an example. This corresponds to the central part of the calorimeter, the same features are seen everywhere in the EMC. The crystal boundaries are drawn as solid lines, a dashed diagonal line shows the ideal correlation ($\theta_{emc} = \theta_{true}$).

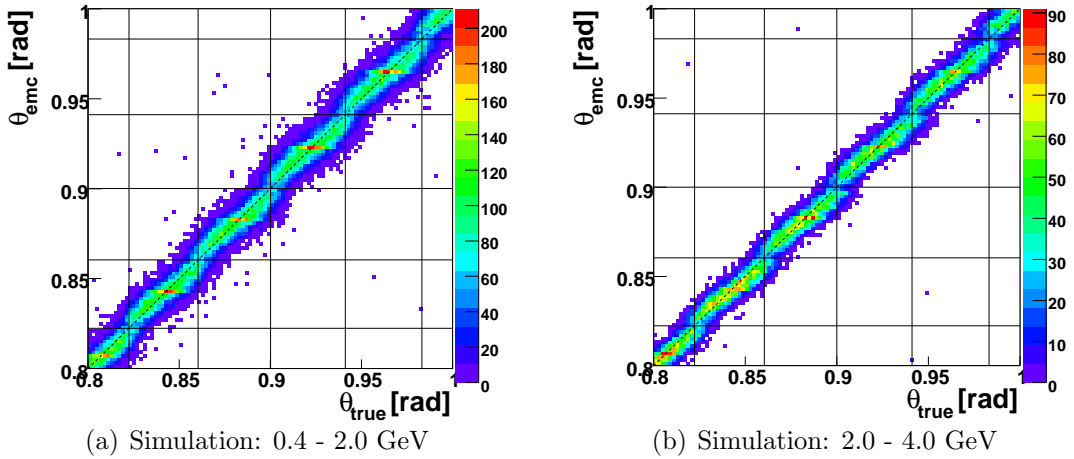


Figure 6.8: Simulation of $\mu\mu\gamma$ data: Crystals in the central barrel with indices $I_\theta = 20 - 25$: θ_{emc} versus θ_{true} . The solid lines correspond to the crystal boundaries on each axis, the dashed line to the ideal correlation. Deviations from a straight line, the so called S-shape, are clearly visible for each crystal.

The shape of the deviation shown in Fig. 6.8 is sinusoidal. There is no deviation observable at the crystal center whereas the deviation is maximal at about

1/3 and 2/3 of the crystal front face. At the crystal edges, the deviation reduces to a minimum again. In the following, this deviation is called S-shaped.

The systematic deviation seen in the position reconstruction algorithm agrees qualitatively with earlier Monte Carlo studies [20].

Using the Kinematic Fit

The structures inside single crystals can be studied using the photon angle calculated with the kinematic fit. As shown in section 6.1.1, θ_{fit} provides an excellent estimate for the position of the generated particle. It will be used in the following to estimate the true photon position.

In Fig. 6.9, θ_{emc} is drawn as a function of θ_{fit} for simulation and data in two energy ranges. The S-shape structure introduced by the position reconstruction algorithm is clearly visible. However, the structure is smeared out due to uncertainties of the kinematic fit. Using θ_{fit} instead of θ_{true} , the S-shape deviation looks more like a linear tilt, than like the sinusoidal deviation observed using generator level information. The tails seen in Fig. 6.9 are due to tails in the estimate of the kinematic fit describing the true (generator level) angle. The effect in data is much smaller than in the simulation, but there is clearly a systematic crystal structure visible.

The band structure seen in the tails of Fig. 6.9 is due to the requirement that the reconstructed and the calculated position agree within 15 cm (see section 4.7.4). Beside the uncertainties introduced, the kinematic fit provides a good handle to study structures of the position reconstruction inside single crystals.

A very fundamental way to study the position reconstruction is to draw the reconstructed angle in a histogram binned fine enough to see a crystal structure. This is done in Fig. 6.10 for data and simulation. Solid lines indicate the crystal boundaries. A crystal structure is clearly visible as well as a big difference in position reconstruction between data and simulation. The size of the gaps between two crystals is significantly larger in the simulation than in data. This is consistent with the observation that the S-shape deviation is more emphasized in the simulation. A larger systematic deviation in the reconstructed angle results in the projection in a more pronounced crystal structure. For the rest of this chapter, this effect will be quantified and possible correction schemes will be developed.

6.3.2 Quantitative Discussion

In order to quantify and correct the observed deviation on the crystal front face, the crystal structure seen in Fig. 6.9 can be divided in slices and the peak positions of the resulting distributions are determined by a fitting procedure.

The S-shape is measured quantitatively in the energy interval of 2.0 to 4.0 GeV. In this range, the photons still cover the whole calorimeter and the estimate of

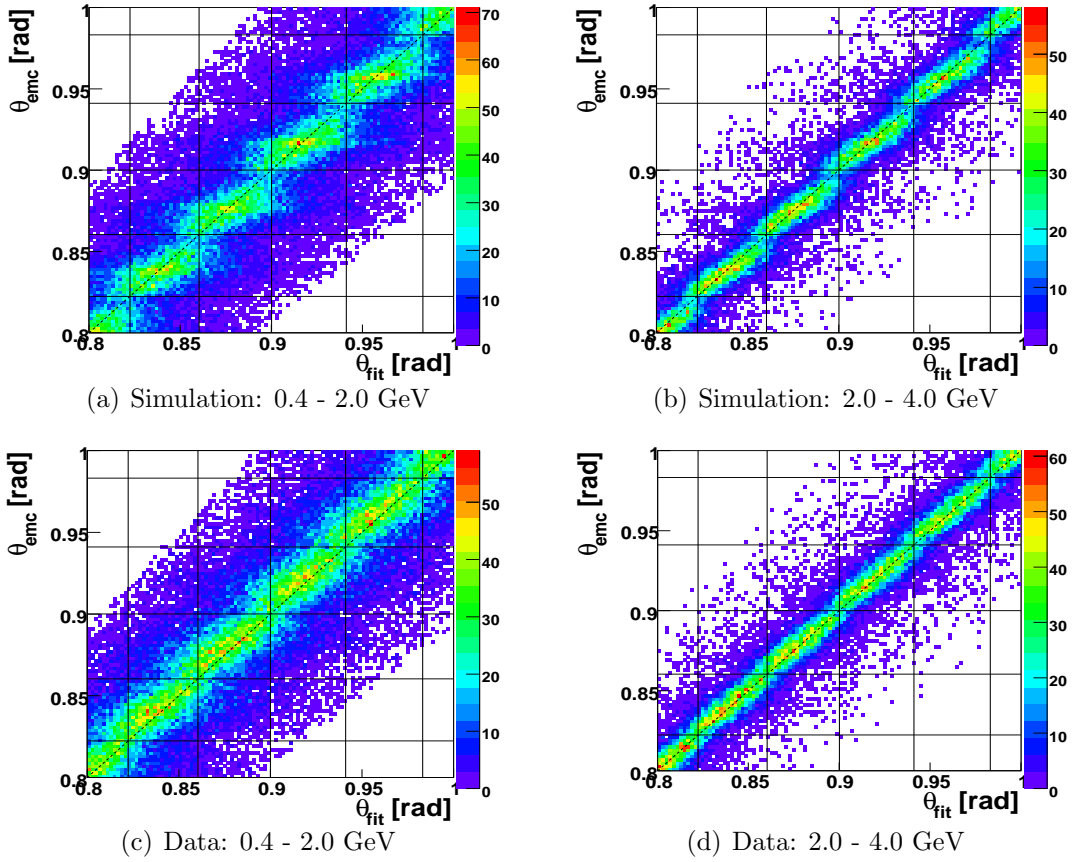


Figure 6.9: Correlation of the θ_{emc} and θ_{fit} for data and simulation. As an example, crystals with indices $I_\theta = 20-25$ are chosen. The same features are seen everywhere in the EMC. A deviation from the ideal correlation can be observed. The effect is larger in the simulation than in data.

the kinematic fit is well correlated with the true angle. At higher energies, the kinematic fit gives excellent estimate, but the photon phase space is restricted to the forward area. At lower energies the uncertainties in the kinematic fit lead to a poor estimate of the true angle.

The procedure is the following: Each of the 56 θ -crystal rings is divided in 10 equidistant slices. In total, there are $10 \cdot 56$ slices. The events are then binned in these slices in θ_{fit} . In each slice, θ_{emc} is drawn in a histogram. This results in a distribution of the reconstructed angle for each slice in the fitted angle, as shown as an example for $I_\theta = 19$ in Fig. 6.11. The peak position of this distribution is determined by a fit using a Novosibirsk function (see Eq. 4.2 for details).

The peak position obtained from the peak fit procedure is shown in Fig. 6.11 is drawn versus the center of the slice in θ_{fit} . This results in a correlation of the reconstructed angle with the angle calculated with the kinematic fit for each of

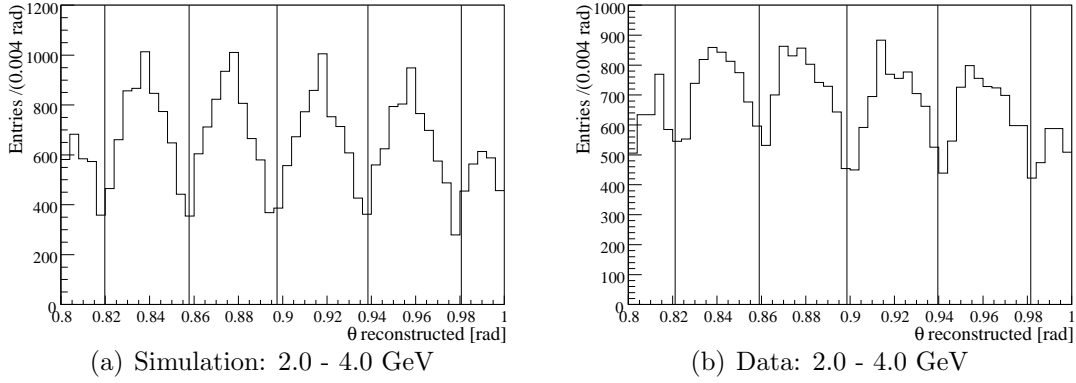


Figure 6.10: Histogram of θ_{emc} in simulation and data. Exemplarily, crystals with indices $I_\theta = 20 - 25$ are shown. A crystal structure is clearly visible, in simulation it is more pronounced than in data.

the 56 θ -crystal rings.

Fig. 6.12 shows the peak position of the reconstructed polar angle as a function of θ_{fit} for data and simulation. The size of the sub crystal deviation is expected to be different along θ -direction, dependent on the distance to the interaction point and on the material distribution in front of the EMC. As an example, four crystal rings in different areas of the calorimeter have been chosen: The forward barrel ($I_\theta = 15, 25$), central barrel ($I_\theta = 35$) and the backward barrel ($I_\theta = 45$). In both data and simulation, the S-shape deviation is clearly visible. When comparing Fig. 6.12 (a) for the simulation and (b) for data the difference is striking: The effect is very strong in simulation and quite weak in data.

It is expected that the effect is stronger in the simulation since the shower is about 15% narrower (see section 5.3.1) and hence less crystals are involved in the position reconstruction. This can be seen as well in Fig. 6.2 which shows that the number of crystals used in the position reconstruction algorithm is significantly smaller in the simulation than in data.

The dependence of θ_{emc} on θ_{fit} is fitted with

$$f_i(\theta_{fit}) = a_0 \cdot \theta_{fit}^3 + a_1 \cdot \theta_{fit}^2 + a_2 \cdot \theta_{fit} + a_3 \quad (6.9)$$

where the $f_i(\theta_{fit})$ are the fit functions for all 56 θ -rings with parameters a_j which are determined for each crystal ring separately. The following constraints are put on the fit function:

1. The fit function is required to satisfy

$$f_i(\theta_{fit}) = \theta_{fit} \quad (6.10)$$

at the boundaries of each crystal. This is motivated with the observations using generator level information (section 6.3.1, Fig. 6.8) and ensures furthermore a continuous transition between the crystals.

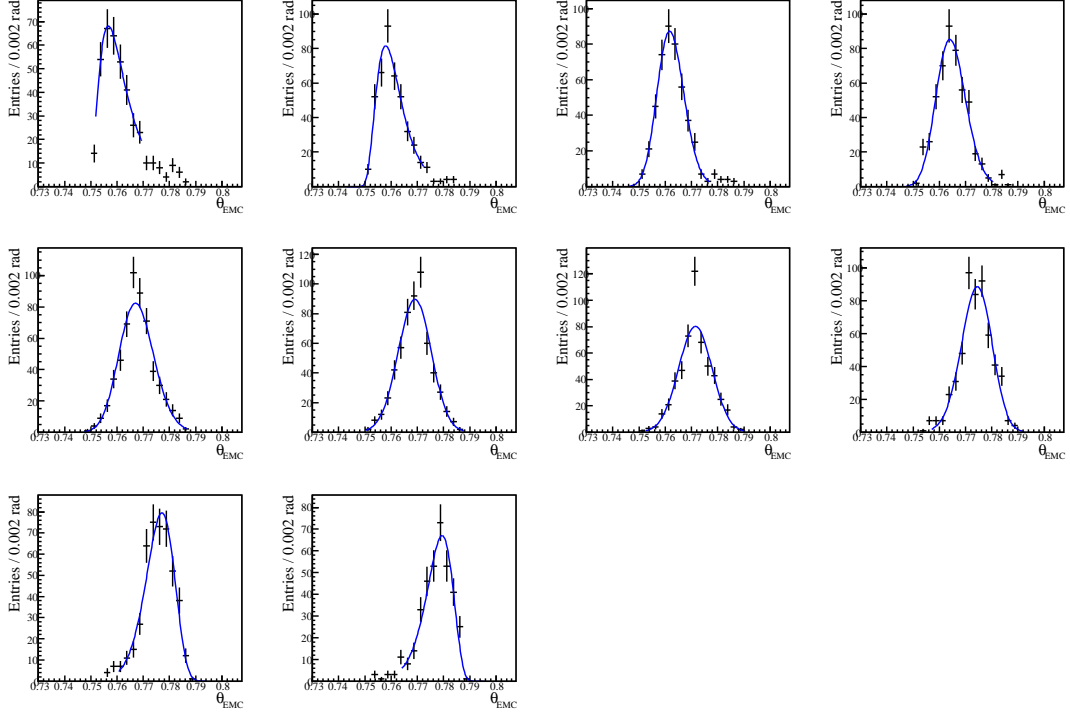


Figure 6.11: Exemplarily shown is the crystal with $I_\theta = 19$ in the simulation. Subfigures 1 - 10 denote the ten slices of the crystal, calculated in θ_{fit} .

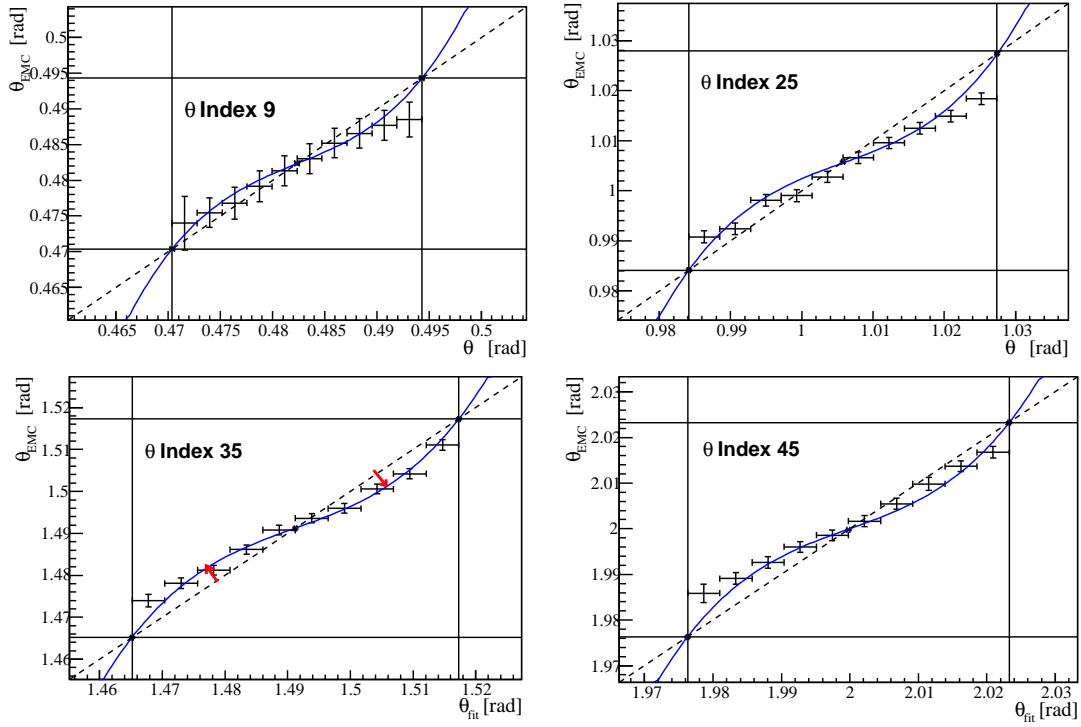
2. It is required that Eq 6.10 is satisfied at the crystal center. This ensures a symmetric parameterization.

The overall size of the sub crystal deviation can be quantified using the function $f_i(\theta_{fit})$. A quantity δ_i^S called amplitude is introduced,

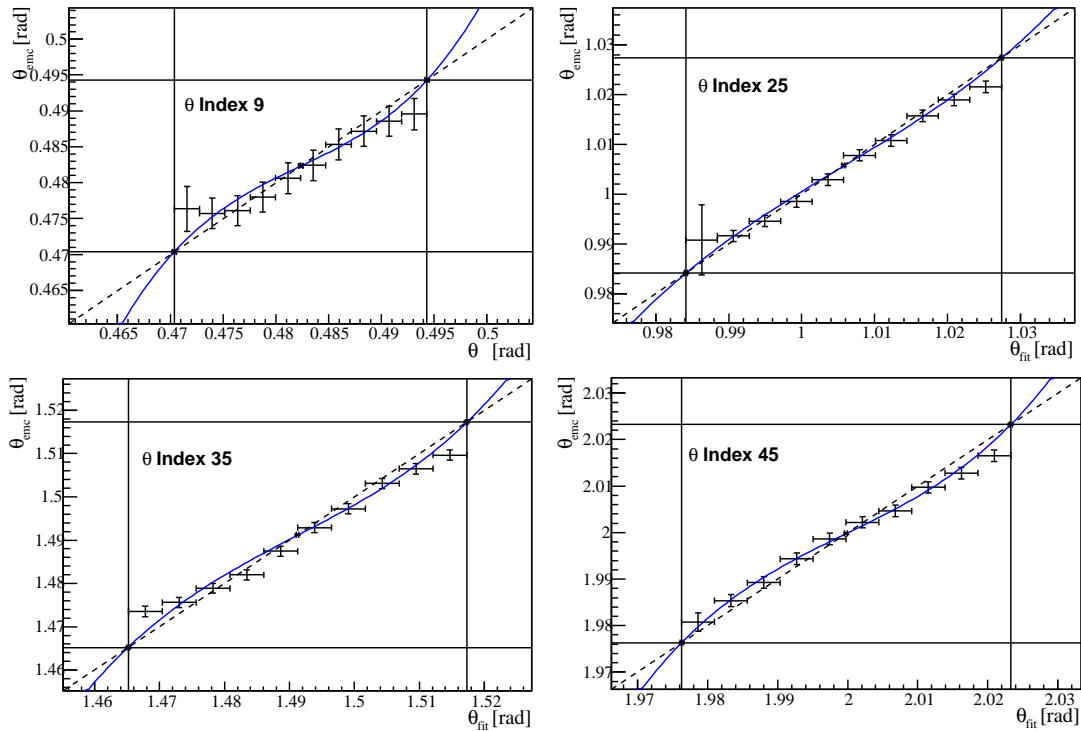
$$\delta_i^S = |A_1^{MAX}| + |A_2^{MAX}| \quad (6.11)$$

where A_1^{MAX} and A_2^{MAX} are the amplitudes of $f_i(\theta_{fit})$ relative to the ideal correlation line (which satisfies $g(\theta_{fit}) = \theta_{fit}$) in the first and second half of the crystal respectively. A_1^{MAX} and A_2^{MAX} are drawn as red arrows in the lower left figure of Fig. 6.12 (a). The quantity δ_i^S measures the maximal size of the deviation in the position reconstruction for the i^{th} crystal ring.

The size of the S-shape deviation of the reconstructed angle studied using the kinematic fit, $\delta_i^S(\theta_{emc}/\theta_{fit})$ is determined for each θ -index separately. It is shown in Fig. 6.13 (a) for the simulation. It increases from ~ 4 mrad in the forward part of the detector to ~ 10 mrad in the center and decreases afterwards again. The variations are quite large. In data, Fig. 6.13 (b), $\delta_i^S(\theta_{emc}/\theta_{fit})$ is significantly smaller increasing from ~ 2 mrad to ~ 4 mrad in the central barrel. For both data and simulation, the increase of the amplitude is due to the changing distance.



(a) Simulation



(b) Data

Figure 6.12: θ_{emc} versus θ_{fit} for (a) simulation and (b) data (2.0 - 4.0 GeV). Four crystal rings are selected as an example. A diagonal line (dashed) as ideal correlation line is drawn as well as the crystal boundaries (solid).

An effect of the same size gets enhanced in the central barrel by the ratio of the distances r^{EMC} between the interaction point and the cluster centroid.

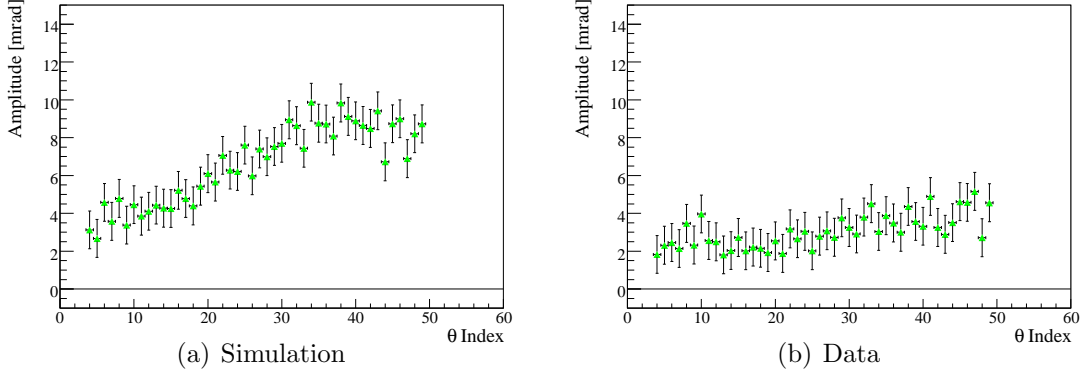


Figure 6.13: $2.0 - 4.0$ GeV: $\delta_i^S(\theta_{emc}/\theta_{fit})$ for simulation and data as a function of the θ -crystal index. A correlation of the amplitude with the polar angle is visible with a maximum at the central barrel ($I_\theta=37$).

Systematic Study of θ_{fit}

It has to be shown that the sub-crystal structure seen in Fig. 6.12 and 6.13 is not due to a bias in θ_{fit} . Therefore, the amplitude $\delta_i^S(\theta_{fit}/\theta_{true})$ of the angle calculated with the kinematic fit versus the generated angle is studied. It is shown as a function of the θ -index in Fig. 6.14.

Within the significance, no position dependent systematic effect in θ_{fit} is observed. The variations in the distribution of $\delta_i^S(\theta_{fit}/\theta_{true})$ are a measure for the systematic error introduced by the kinematic fit as measure for the true angle. It can be approximated conservatively from Fig. 6.14 as ± 1 mrad, being constant over the polar angle. This value will be assigned to the measurement of the amplitude, i.e. to the size of the S-shape deviation.

6.4 Correction of the Sub-Crystal Deviation

There are two principally different ways to study the influence of a correction for the S-shape deviation depending on the input parameter of the correction function: A correction function can be developed using the calculation with the kinematic fit as input or using the reconstructed angle itself as input.

Using fit information is intrinsically much easier since the input quantity is well known. It is a good method to study the feasibility of a correction for the sub-crystal structure and to analyze the influence of the S-shape deviation on the resolution. Unfortunately, in order to develop a correction, the calculation

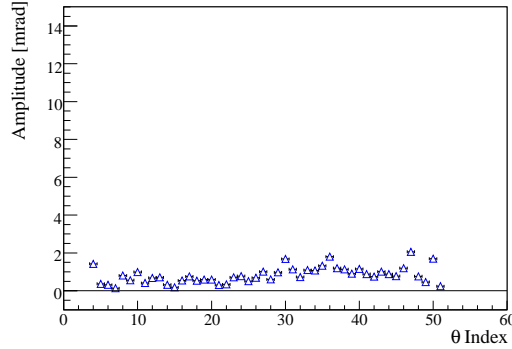


Figure 6.14: *MC 2 - 4 GeV: $\delta_i^S(\theta_{fit}/\theta_{true})$ versus the θ -index. The kinematic fit estimates the sub-crystal position without a dependency on the polar angle, but with variations of about ± 1 mrad.*

using the kinematic fit cannot be used. A correction can be developed using the reconstructed angle as input. This is more complicated since the input quantity of the correction has uncertainties itself.

The correction functions are determined depending on the polar angle for the crystal rings $I_\theta=4-50$. In the three most forward rings, $I_\theta=1-3$ there are about three radiation lengths material in front of the crystals and the signal is therefore bad compared to the rest of the calorimeter. In the most backward rings, $I_\theta=51-56$, due to kinematics the event number is not sufficient to perform a correction (see chapter 4.1 for the photon phase space). These crystal rings are left uncorrected. This leaves 47 crystal rings in the polar angle to perform a correction for.

6.4.1 Systematic Study Using Fit Information

In this chapter, an additive correction for the S-shape deviation is studied. The correction depends on the calculation by the kinematic fit. The difference between the measured angle and the expectation is called *mean shift*, $\Delta\theta_{fit}^{emc}$ and is defined as

$$\Delta\theta_{fit}^{emc} = \theta_{emc} - \theta_{fit} \quad (6.12)$$

where this difference is taken in each of the 10 slices per crystal ring described in chapter 6.3.2.

The mean shift is shown in Fig. 6.15 exemplarily for four different crystals in the forward ($I_\theta = 9, 25$), central ($I_\theta = 35$) and backward ($I_\theta = 45$) barrel part of the calorimeter for data and simulation. In the simulation, the amplitude is about 5 mrad in the central barrel dropping to smaller values in the very forward barrel ($I_\theta = 9$). In data, the amplitude of the mean shift is significantly smaller.

The correction function is defined by a constrained third order polynomial fit to the mean shift. The constraints are similar to those described for Eq. 6.9, $\Delta\theta_{fit}^{emc}$ is required to be zero at the crystal boundaries and at the center. The fit

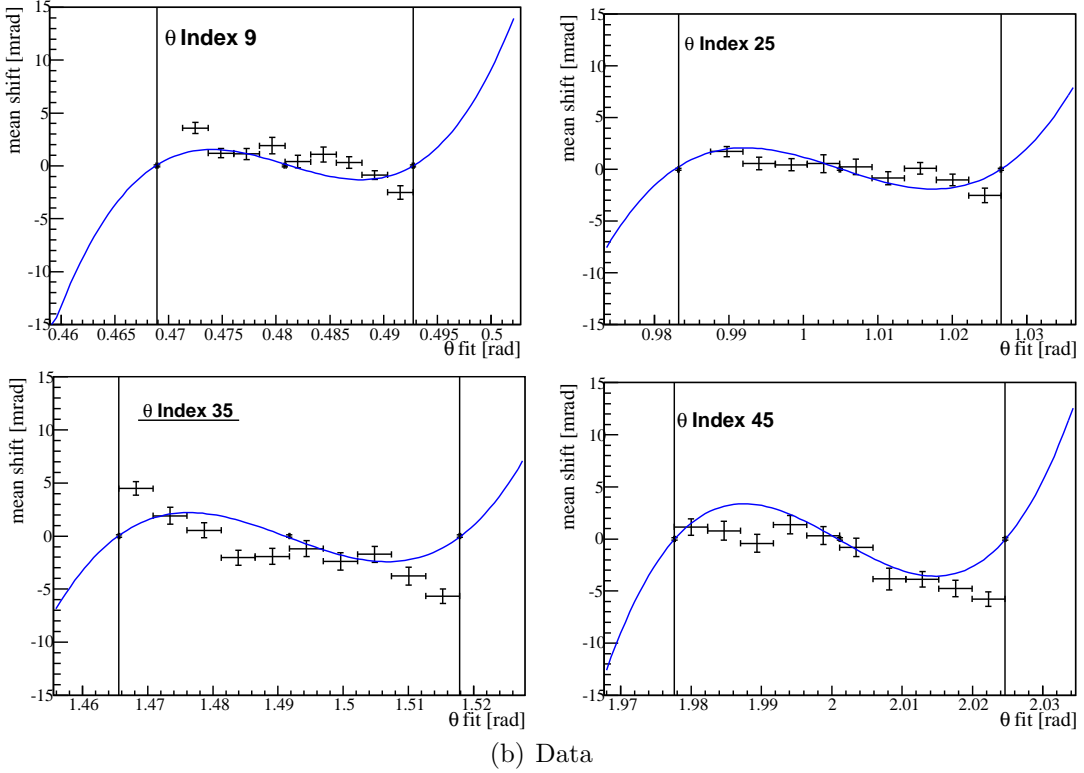
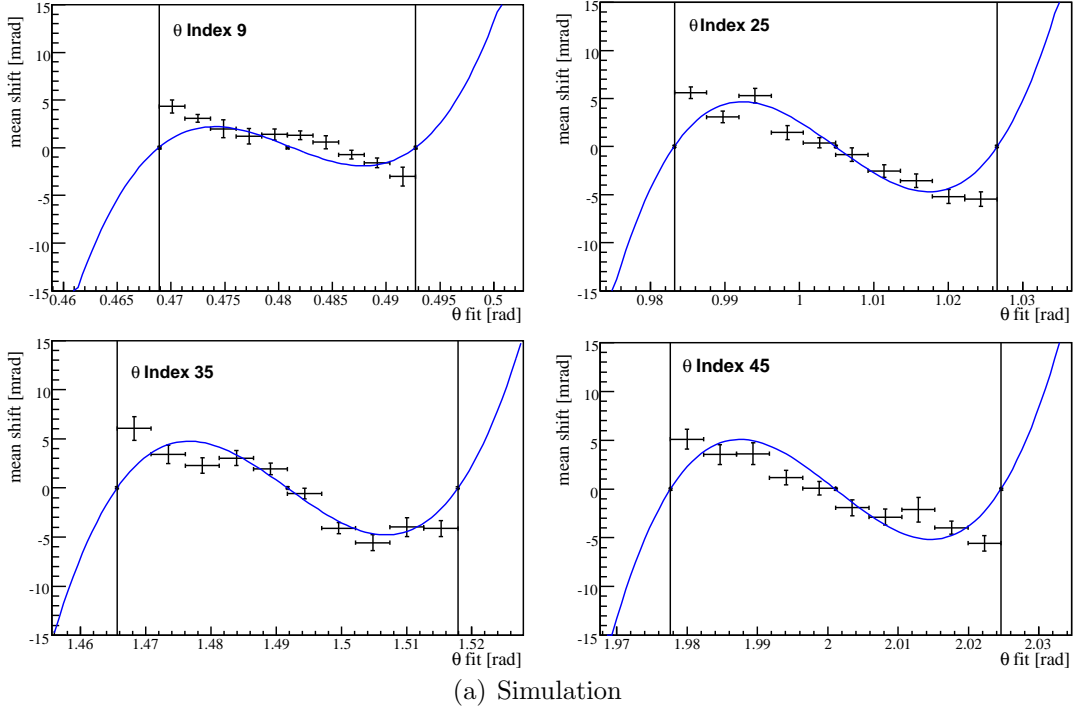


Figure 6.15: Mean shift $\Delta\theta_{fit}^{mc}$ for 2.0 - 4.0 GeV: The Difference of the reconstructed polar angle to the ideal correlation line is drawn as a function of the fitted angle.

describes the measured points reasonably well (see App. C for a χ^2 distribution) with a tendency to underestimate the effect. In Fig. 6.12 (a) and (b), it is seen that the assumption of a vanishing correction at the crystal boundaries is doubtful. However, since the edges of a crystal have some signal pollution of the neighbor crystals and the sinusoidal shape is seen using generator information, this constraint of the fit is kept. A continuous transition between the crystals seems to be more reasonable as well.

The correction procedure is as follows: For each event, the crystal index in θ and the relative position on the crystal face is determined from the angle estimated by the kinematic fit. According to the crystal index, a mean shift correction function is chosen. This function is evaluated at the specified relative position in the crystal. The functional value of the correction function gives the offset of the reconstructed angle to the true angle (approximated with the kinematic fit). In order to correct for the effect, this offset is subtracted from the reconstructed angle. As mentioned before, the crystal rings $I_\theta = 1 - 3$ and $I_\theta = 51 - 56$ are left uncorrected.

Results of the Mean Shift Correction

A histogram of the reconstructed polar angle with the mean shift correction applied is shown in Fig. 6.16 as black line for the rings $20 < I_\theta < 25$. The uncorrected polar angle is drawn as red, dashed line. The ratio of peaks to gaps is a measure for the quality of the angular reconstruction.

In the simulation, the gaps between the crystals are reduced by the correction, leaving a distribution with less emphasized structures. However, a crystal structure is still clearly visible. While for data, the correction has only a small effect, the agreement between data and simulation improves drastically.

The mean shift correction results in a flattened amplitude as shown in Fig. 6.17 for corrected and uncorrected datasets in data and simulation. The amplitude $\delta_i^S(\theta_{emc}/\theta_{fit})$ for the simulation is reduced from maximally 10 mrad with a strong dependence on the polar angle to an average effect of 3 mrad with a maximum at ~ 4 mrad. The dependence on the polar angle has vanished as well. For data the original effect is much smaller as shown in Fig. 6.17 (b). Still, the mean shift correction reduces the amplitude to an average size of ~ 1.5 mrad. The improvement in the agreement between data and simulation is clearly seen.

With the correction of the S-shape deviation using the kinematic fit, the sub-crystal deviation in the angular reconstruction is reduced significantly. The effect on the angular resolution is studied in Fig. 6.18. The calorimeter is divided in four sections, as introduced in section 6.2.2, represented in the sub-figures (a) - (d). The resolution has improved for all four divisions. Especially the simulated values, where the mean shift is significantly larger than in data, the improvement in resolution is clearly seen. The measured resolution is determined with the procedure described in section 6.2.2. For a better clearness, the fit functions

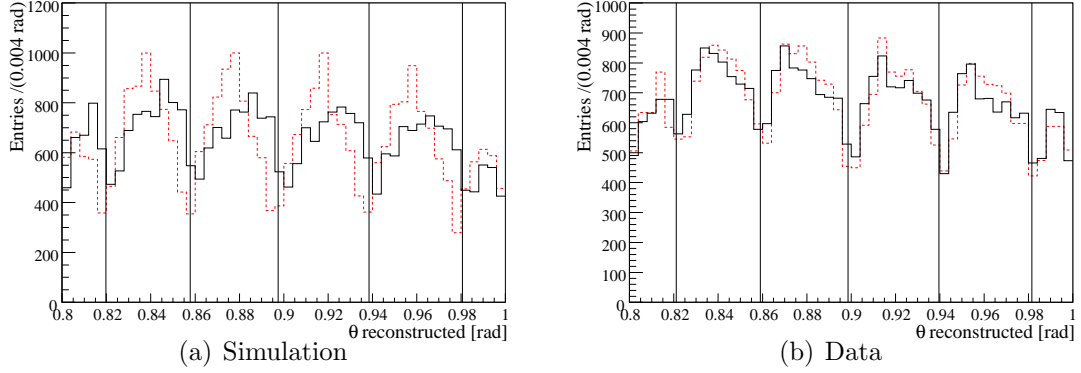


Figure 6.16: Histogram of the polar angle reconstruction in simulation and data for the energy range of 2.0 - 4.0 GeV, exemplarily for the crystals $I_\theta = 20 - 25$. The red dashed histogram is without a correction applied, the solid black one is the mean shift corrected histogram. In the correction, the gaps between the crystals reduce.

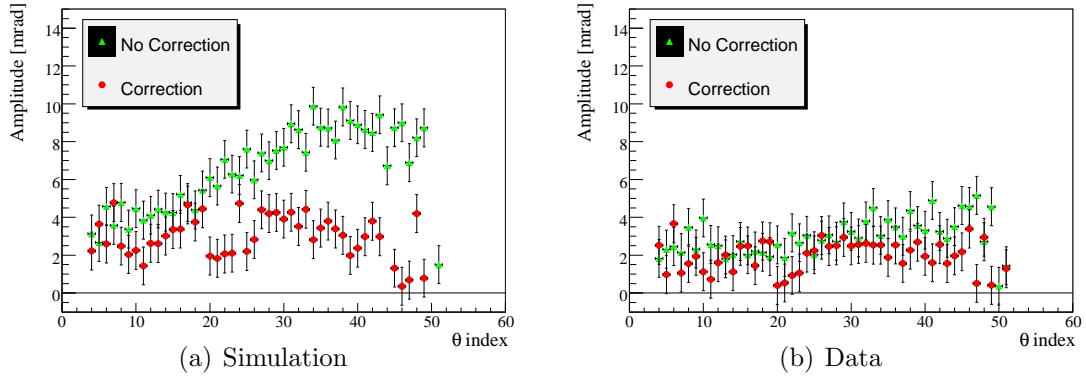


Figure 6.17: 2.0 - 4.0 GeV: Corrected and uncorrected amplitude for the simulation and data. The correction shown is the mean shift correction determined dependent on the calculation with the kinematic fit. A clear reduction of the amplitude can be observed for the simulation.

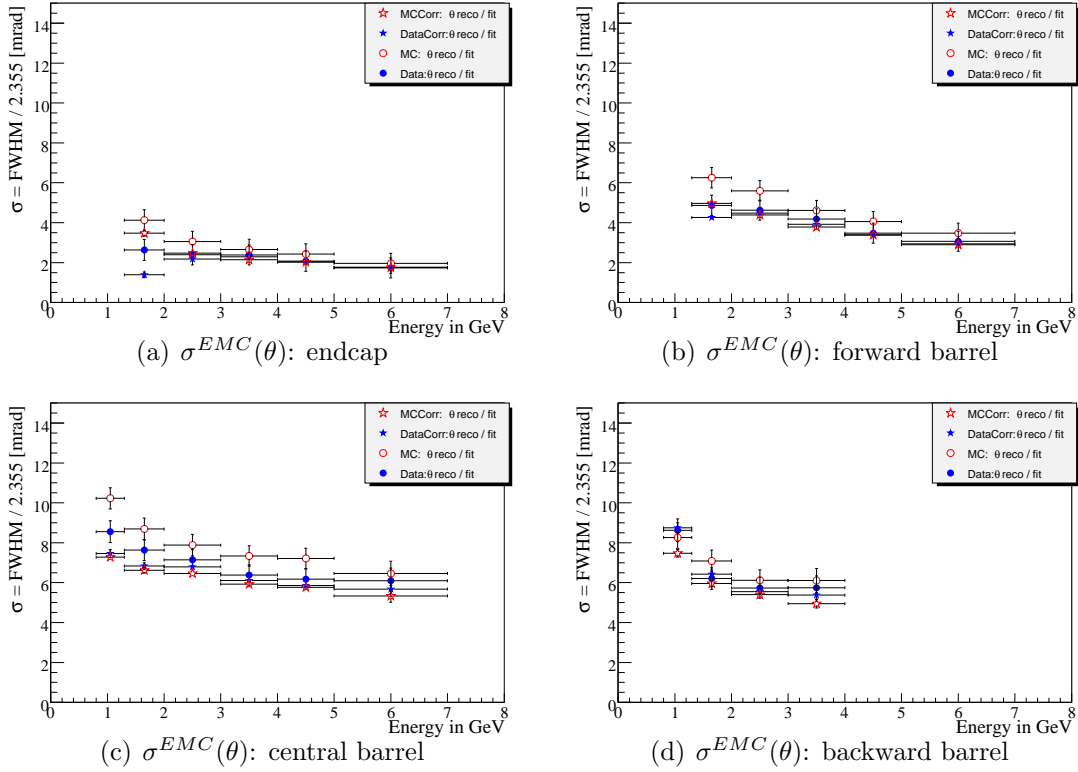


Figure 6.18: Resolution of the polar angle with the mean shift correction. The four figures represent the different divisions of the calorimeter as defined in chapter 6.2.2. With the correction applied, the resolution is improved and the agreement of data and the simulation improved as well.

are not drawn in Fig. 6.18. A summary of the coefficients of the fitted angular resolution is given table 6.3.

The presented correction reduces the sub-crystal deviation, improves the angular resolution and leads to a better description of the data by the simulation. It has to be emphasized that this study relies on the calculated photon position, it can therefore only be seen as study of the effects of the sub crystal deviation on position reconstruction.

From these observations, it is possible to conclude that the differences in position reconstruction between data and Monte Carlo simulation are due to a big part to the different deviations on the sub-crystal level. A more fundamental approach to eliminate the difference between data and the simulation would be to correct for the origin of this difference. That would mean to broaden the shower width in the Monte Carlo simulation.

EMC region		Uncorrected		Corrected	
		Data	Simulation	Data	Simulation
endcap	a [mrad]	4.20±2.23	5.86±0.39	4.77±0.19	4.95±0.19
	b [mrad]	0.39±1.03	0±3.11	0.0±0.27	0±2.82
forward barrel	a [mrad]	8.75±2.89	10.12±0.49	7.37±1.54	7.18±1.54
	b [mrad]	0.05±1.91	0.0 ±2.27	0.50±0.77	0.57 ±0.73
central barrel	a [mrad]	5.17±3.60	6.86±3.74	5.73±1.35	4.30±1.18
	b [mrad]	4.88±1.79	5.07±1.83	4.20±0.70	4.12±0.63
backward barrel	a [mrad]	1.31±5.54	3.23±0.04	5.32±2.33	4.92±2.17
	b [mrad]	6.03±3.20	5.38±3.48	3.35±1.45	2.21±1.35

Table 6.3: $\sigma(\theta)$ for a corrected and an uncorrected dataset. With the correction applied, the resolution improves more in the simulation and the agreement between data and simulation improves.

6.4.2 Correction of the Sub Crystal Deviations

In order to develop a correction scheme which is usable for an arbitrary dataset, a correction has to be defined which depends only on the reconstructed angle θ_{emc} . For this, the functional dependence discussed in section 6.3.2 is used.

The correction proceeds as follows: The S-shape deviation is fitted for each crystal ring in data and simulation separately using the fit function Eq. 6.9 with constraints (see Fig. 6.12). The crystals used for the correction include, as in the last section, crystal rings with $I_\theta = 4 - 50$. There are 47 correction functions which obey a relation of the form:

$$\theta_{emc} = f_i(\theta_{fit}) \approx f_i(\theta_{true}) \quad (6.13)$$

where f_i is fitted correction function for the i^{th} crystal ring. That means the reconstructed angle is a S-like function of the angle calculated with the kinematic fit, and thus of the true angle. It can be inverted analytically using cardanos formulas [27]. The inverted function is the correction function. It is applied to the reconstructed angle:

$$f_i^{-1}(\theta_{emc}) = \theta_{fit} \approx \theta_{true} \quad (6.14)$$

where $f_i^{-1}(\theta_{emc})$ is the correction function which is to be applied to the reconstructed angle yielding to an angle corrected for the sub crystal deviation.

Results of the Correction

Unlike in section 6.4.1, the input quantity θ_{emc} of the correction function has uncertainties itself. These uncertainties of the angular measurement smear out the

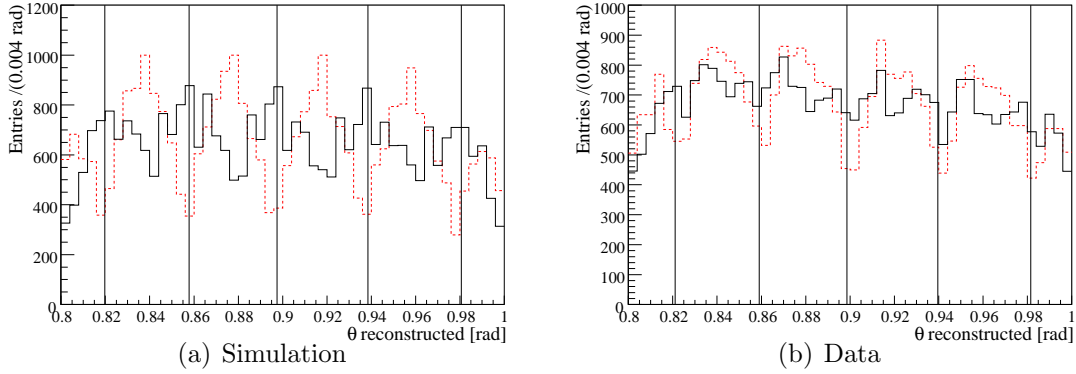


Figure 6.19: Histogram of the polar angle reconstruction in the simulation and data for the energy range of 2.0 - 4.0 GeV. The red dashed histogram is without a correction applied, the solid black one is the corrected histogram. In data, the crystal structure vanishes completely whereas being reduced significantly in the simulation.

correction and the results are not expected to reach the improvements obtained for the systematic study using θ_{fit} .

The reconstructed polar angle is histogrammed in Fig. 6.19. The uncorrected histogram is drawn in dashed, red line and the corrected one in solid black line. The crystal structure vanishes completely in data. For the simulation, the structure is reduced significantly. An accumulation of entries is seen at the gaps between the entries.

In Fig. 6.20, the amplitude of the S-shape deviation $\delta_i^S(\theta_{emc}/\theta_{fit})$ is drawn as function of the polar angle. The correlation of the amplitude with the polar angle vanished after the correction. A broad distribution with a mean around 3-4 mrad in the simulation and around 1-2 mrad in data remains.

The effect of the S-shape correction on the position resolution is studied in Fig. 6.21. Overall, the resolution does not improve due to the correction. This was expected since the uncertainty of the position measurement is folded into the resolution when the S-shape correction is applied. However, the systematic difference in position reconstruction between data and simulation is corrected. The dependence on the polar angle of the observed deviation is corrected.

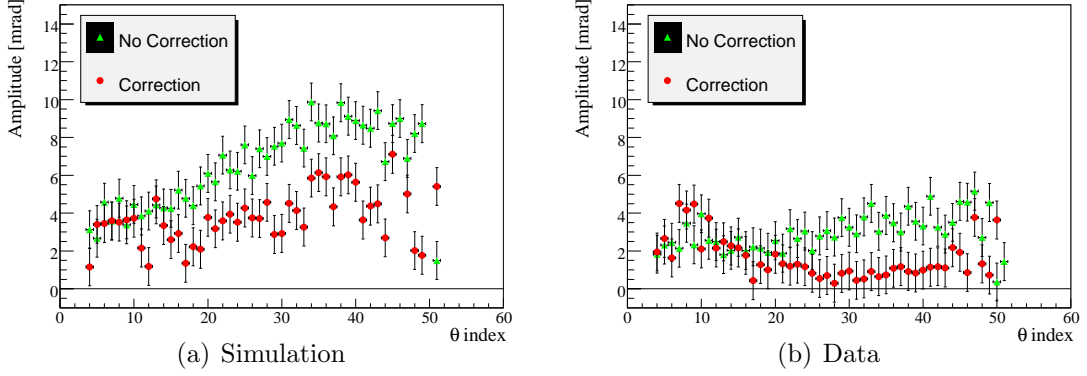


Figure 6.20: $2.0 - 4.0$ GeV: Corrected and uncorrected amplitude for simulation and data. The correction shown is the correction dependent on the reconstructed angle. A clear reduction of the amplitude is seen for both data and the simulation.

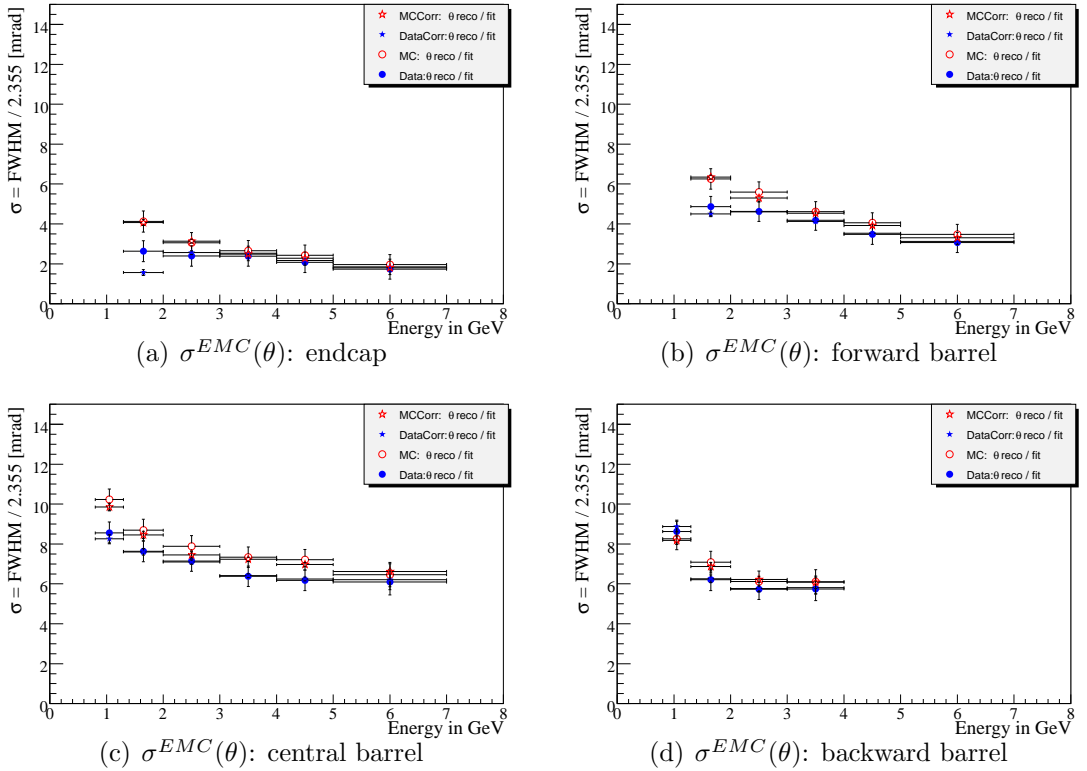


Figure 6.21: Resolution of the polar angle for data and simulation. The applied correction is independent of the calculation with the kinematic fit. No improvement is seen within the significance.

6.5 Summary

The position reconstruction of the *BABAR* calorimeter has been studied. On the crystal level, the simulation was found to describe the data with an accuracy of 0.1-0.5%.

The angular resolution of the *BABAR* calorimeter has for the first time been measured directly for photons in data and Monte Carlo simulation. It was determined in four regions of the calorimeter. Over the whole calorimeter, the angular resolution is better in data than in the simulation. This can be understood taking the smaller width of generated showers into account.

It was found that the position reconstruction has a systematic deviation dependent on the position relative to the edges of the crystal. The size of this effect is dependent on the polar angle, being maximally 10 mrad. It is much more distinct in the simulation. In a feasibility study, a correction for this deviation is developed, relying on the position calculated with the kinematic fit. The influence of the deviation on the angular resolution is studied, it was found to improve after the correction. Furthermore, the agreement between data and simulation is very good after the correction.

A correction scheme for the observed deviation was developed. Due to the uncertainty in the reconstructed angle, no improvement in the position resolution is found. However, the sub-crystal deviation is corrected and the agreement between data and simulation is improved.

Chapter 7

Calibration with Minimal Ionizing Muons

Muons from the final state of the process $e^+e^- \rightarrow \mu^+\mu^-\gamma$ are studied in this chapter. Muons at energies between 2 and 9 GeV, are close to the minimal value of energy deposition according to the Bethe Bloch formula (see Eq. 2.4), they are called minimum ionizing particles (MIP). The energy deposited by a muon in the EMC is of the order of 200 MeV.

The minimal ionizing signal of muons is used as an alternative approach to study the performance of the EMC. Muons are very abundant and their momentum is well measured by the tracking devices. In contrast to electromagnetic showers, the energy deposition is localized, making it possible to study the properties of single crystals. However, the longitudinal energy deposition is in contrast to electromagnetic showers homogenous. In this chapter, the energy deposition of muons in the calorimeter is used to study the energy measured in individual crystal rings.

7.1 Single Crystal Calibration

The local attributes of a single crystal are easily accessible with MIPs, in contrast to electromagnetic showers where a cluster of many crystals is studied. As additional requirement is set that the muon signal creates clusters with one crystal only. In order to increase the number of events, crystal rings in the polar angle are studied in this section.

The average energy loss dE/dx of muons can be calculated using the Bethe-Bloch formula (see Eq. 2.4). In the EMC, dE/dx can be measured from the energy deposition of muons in the crystals. It is approximated by

$$\left\langle \frac{dE}{dx} \right\rangle \approx \frac{E_{raw}}{l}, \quad (7.1)$$

where l denotes the crystal length. A summary of the crystal lengths can be

I_θ	length [cm]
1	30.5
2-8	32.5
9-15	32.55
16-22	31.62
23-29	30.69
30-56	29.76

Table 7.1: Length of the crystals according to the index in the polar angle.

found in table 7.1.

The measured dE/dx does not equal the value calculated using the Bethe-Bloch formula. The muons are required to deposit energy only in one crystal. This excludes the high energetic outliers which have a significant influence on the mean of the deposited energy (but do not affect the peak position). The Bethe-Bloch formula determines the mean of the energy loss. Therefore, the value calculated using the Bethe-Bloch formula does not describe the energy deposition as it is studied here¹. Only the relative response of individual crystal rings is determined.

Fig. 7.1 shows the deposited raw energy (with single crystal calibration applied, section 3.4) exemplarily for two crystal rings in the polar angle. The peak position is determined with a fit of a Novosibirsk function (Eq. 4.2) according to the algorithm described in section 4.6.

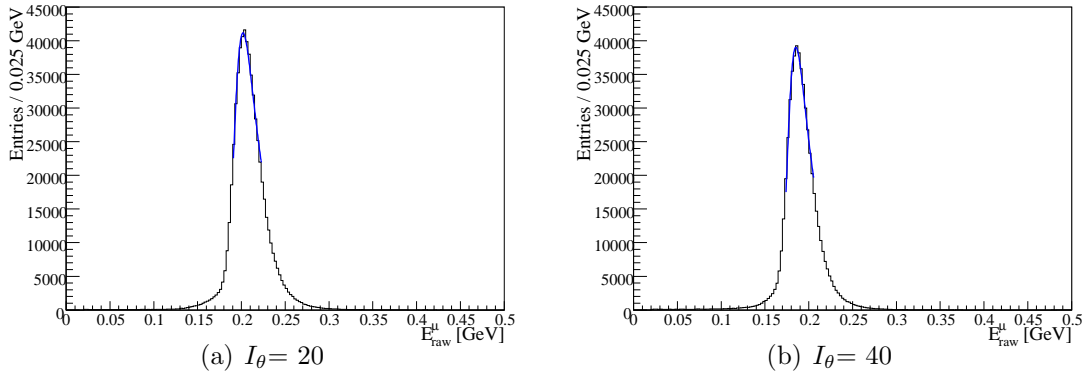


Figure 7.1: Energy deposition (E_{raw}) by muons, exemplarily shown for $I_\theta = 20$ and $I_\theta = 40$. The fit to determine the peak position is shown as well.

The peak position determined from Fig. 7.1 divided by the crystal length is

¹It is found that the Bethe-Bloch formula describes the energy deposition of muon in the EMC if the requirement of one crystal is released.

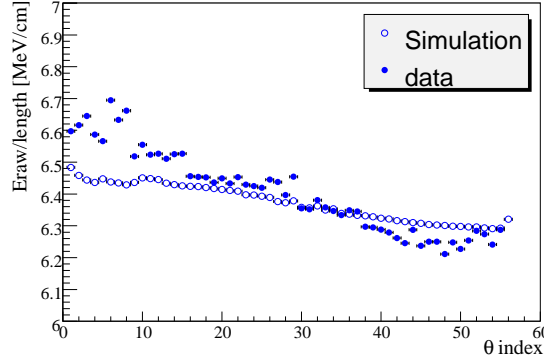


Figure 7.2: E_{raw} over crystal length as a function of I_θ . The data (close circles) show variations of the order of 1%, whereas in simulation (open circles) only small variations in forward direction are seen. The overall slope can be assigned to the relativistic rise of the energy deposition. It is not well described by the simulation.

shown in Fig. 7.2 as a function of the crystal index in the polar angle for simulation and data. Two features are seen: The slope of the deposited energy in data is not described by the simulation and the measured response of the crystal rings shows crystal to crystal variations at the 1% level. Since the muon momentum is correlated with the polar angle (see Fig. 4.2), the slope seen in Fig. 7.2 can be understood to originate from the relativistic rise in the Bethe-Bloch formula. The observed differences in the single crystal response can be used to deduce single crystal correction. The deviations from the expectation have to be determined. As discussed above, the deposited energy cannot be normalized to the Bethe-Bloch formula.

The energy deposition of each event has to be normalized to the average energy deposited at its momentum. The deposited energy over the crystal length is thus drawn as a function of the momentum in Fig. 7.3 for both simulation (a) and data (b). It is fitted with a third order polynomial $f^{MC/data}(p_\mu)$,

$$f^{MC/data}(p_\mu) = peak \left(\frac{E_{raw}}{l}(p_\mu) \right) \quad (7.2)$$

which is determined separately for simulation and data. It describes the momentum dependence of the energy deposition well ($\chi^2/dof = 0.2$ for simulation and 1.75 for data). In data, the increase of the deposited energy with the momentum is roughly 7%. This is not described in the simulation, where the momentum dependence is of the order of 4%. In order to study systematic deviations in the response between the crystal rings, the deposited energy is normalized to the corresponding value of $f^{MC/data}(p_\mu)$.

The energy deposition of muons per unit length is normalized to $f^{MC/data}$,

$$\Delta_\mu^{peak}(I_\theta) = peak \left(\frac{E_{raw}}{l \cdot f^{MC,data}(p_\mu)} \right), \quad (7.3)$$

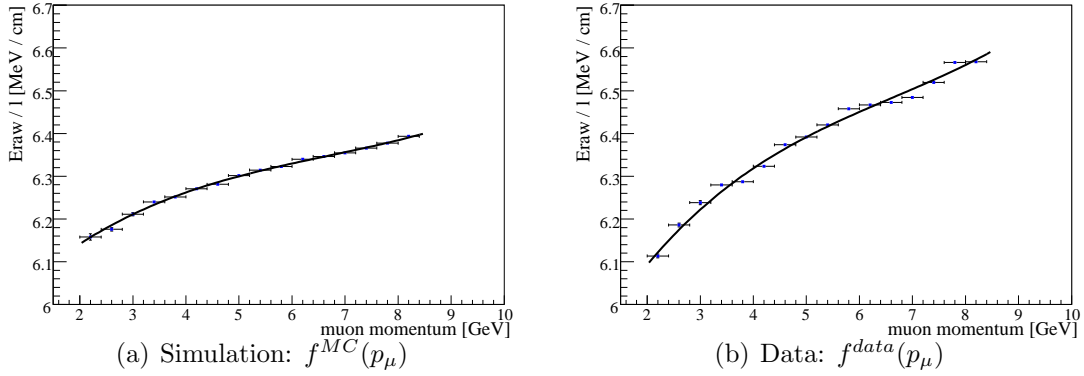


Figure 7.3: dE/dx approximated by E_{raw} / l as a function of the energy for (a) simulation and (b) data. The energy dependence in data is not described in the simulation. The function $f^{MC/data}(p_\mu)$ is fitted to the points.

where the peak position is determined in dependence of the θ -index, and f is taken separately for data and simulation. It is a measure for the relative response of the crystal rings. In the simulation, Fig. 7.4 (a), deviations of $\Delta_\mu^{peak}(I_\theta)$ from 1.0 in forward direction of the order of 0.3% are seen. In data, Fig. 7.4 (b), $\Delta_\mu^{peak}(I_\theta)$ shows crystal to crystal variations of the order of $\pm 1\%$ over the whole range in the polar angle. This variation hint to differences between the crystals according to their θ -index. The observed deviations of $\Delta_\mu^{peak}(I_\theta)$ from 1.0 can be used as single crystal calibration factors to correct the different crystal to crystal response along the polar angle.

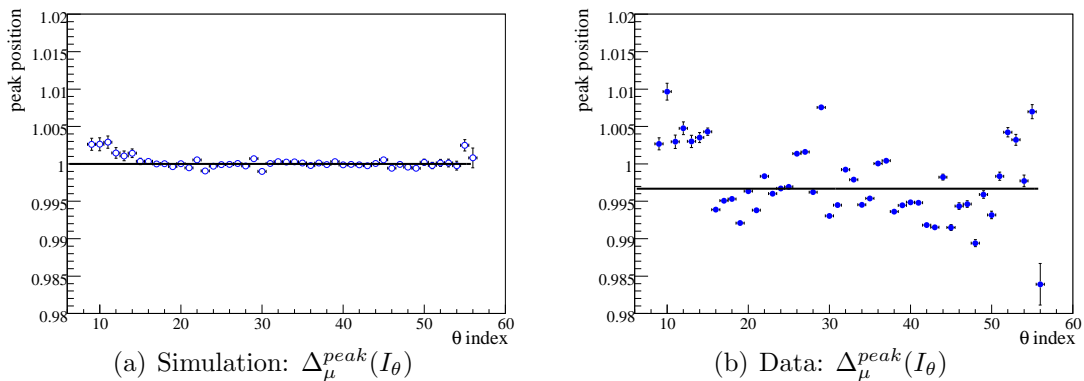


Figure 7.4: *Single crystal response $\Delta_{\mu}^{peak}(I_{\theta})$ normalized to the momentum dependent energy loss (a) for simulation. Some variations of the order of 0.3% are seen in forward direction. (b) for data. Variations in the crystal response of the order of $\pm 1\%$ are seen.*

7.2 Cluster Calibration with MIPS

The longitudinal deposition of energy is different for muons compared to photons. Therefore, the relative single crystal calibration obtained in the last section can be compared to the one obtained from photons.

An approach is to determine the response for photon clusters over the polar angle and compare it with $\Delta_{\mu}^{peak}(I_{\theta})$. In order to account for the finite fit resolution, the double ratio simulation over data,

$$\Delta_{\gamma}^{peak}(I_{\theta}) = \frac{peak(E_{cal}^{MC}/E_{fit}^{MC})}{peak(E_{cal}^{data}/E_{fit}^{data})},$$

analogue to Eq. 5.9 is taken. To increase the number of events, a combined dataset of the run periods 2 to 4 is used². Since in general a shower is extended over many crystals, the crystal with the center of gravity of the shower is taken as the position in the polar angle.

The double ratio simulation over data is shown in Fig. 7.5 (a) as a function of the polar angle. Variations on the level of 0.5% are seen. In order to compare $\Delta_{\gamma}^{peak}(I_{\theta})$ with $\Delta_{\mu}^{peak}(I_{\theta})$, both are drawn in Fig. 7.5 (b) as correlation. Clearly, both quantities are not correlated. The measured crystal to crystal variations in $\Delta_{\mu}^{peak}(I_{\theta})$ are not directly transferable to photon clusters.

The difference in the longitudinal energy deposition for muons and photons together with light yield variations along the crystal do not allow to calibrate the single crystal response with muons.

² It can be shown that the crystal to crystal structures seen in $\Delta_{\mu}^{peak}(I_{\theta})$ persist over the run periods 2 - 4 [33].

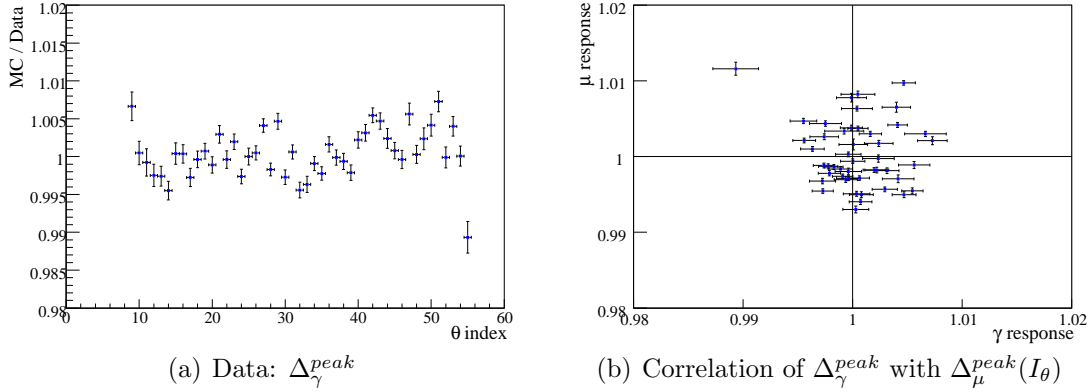


Figure 7.5: (a) Δ_γ^{peak} for data as defined in Eq. 7.4. Structures on the level of 0.5% are seen. (b) Correlation between the structures for muons and for photons. No clear correlation is seen.

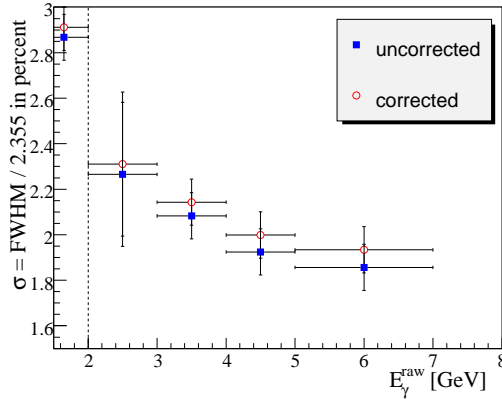


Figure 7.6: Energy resolution with and without single crystal correction. The correction slightly worsens the resolution for photons.

The quality of the calibration using muons can be evaluated by recalculating the cluster energies of the photons. If $\Delta_\mu^{peak}(I_\theta)$ was transferable to photons, the energy resolution determined for the corrected clusters should improve. Fig. 7.6 shows the energy resolution, as discussed in section 5.4, for the uncorrected and the corrected cluster. Since each individual resolution value with the correction applied is larger than the uncorrected one, the calibration using MIPs does not improve the constant contribution to the resolution. However, within the errors, no significant difference in resolution between corrected and uncorrected cluster energies is found.

7.3 Results

The energy deposition in the calorimeter is fundamentally different for electromagnetic showers and for minimal ionizing particles. For showers, the energy deposition is longitudinally localized, depending on the incident energy. The shower maximum is always well in the first half of the crystal (see table 2.1). The situation with muons is completely different: The energy deposition of a muon is given as integral over the whole longitudinal axis of the crystal. The light yield of the crystals changes over the longitudinal axis. Design requirement for the *BABAR* calorimeter were a maximal change of light yield of $\pm 3\%$ in the front half of the crystal and $\pm 5\%$ in the rear half. Light yield changes measured before assembly of the EMC are in this order of magnitude (see App. D for the light yield of some sample crystals). The variations measured before assembly have changed significantly due to radiation damage, specially in the first half of the crystals. Given these changes in light yield, it is not obvious how to translate the crystal response measured with muons to the one for clusters. Using corrections obtained from muon measurements directly, as it is done in this section, is clearly not appropriate.

7.4 Summary

Muons can be used as a tool to study the calorimeter response on a level of single crystal rings. Unfortunately, the response measured with muons is not directly transferable to the response to photons. The different distribution of energy deposition along the longitudinal axis of the crystal together with the change of light yield along this axis is the reason for that.

In order to calibrate the EMC for electromagnetic showers using measurements with muons, a more sophisticated ansatz has to be taken. This could include a model for the change of light yield over the crystal.

Chapter 8

Conclusion and Outlook

Photons from radiative muon pairs,

$$e^+e^- \rightarrow \mu^+\mu^-\gamma \quad (8.1)$$

have proven to be an excellent tool to study the photon reconstruction in the electromagnetic calorimeter as well as to measure the resolution of angle and energy reconstruction.

The energy and the angle of the radiated photon are calculated with a kinematic fit, without using any calorimeter information. The fit provides an excellent estimate for energy and angle of the photon for energies above 400 MeV.

Using the above photons, it was for the first time possible to derive a cluster energy calibration for photon energies above 1.5 GeV. The dependence on energy and polar angle is calibrated separately for the four periods of data taking. The obtained calibration functions reproduce the correct energies within a 0.1%-0.4% statistical uncertainty. In addition there is a 0.3% systematic uncertainty of the energy scale.

Using photons with energies above 2 GeV, the energy dependent resolution function has been determined to be

$$\frac{\sigma(E)}{E} = \left(\frac{(2.74 \pm 0.61)}{\sqrt[4]{E/GeV}} \oplus (0.57 \pm 1.45) \right) \%. \quad (8.2)$$

The resolution obtained in the Monte Carlo simulation was found to be smaller than in data. As indicated by the large statistical errors, the high energy photons are not sufficient to determine the two terms of the resolution function ($1/\sqrt[4]{E}$ term, constant term) independently.

It was for the first time possible to determine the angular resolution of the *BABAR* calorimeter for photons in a direct way for data as well as for the Monte Carlo simulation. Over the whole calorimeter, the obtained angular resolution in data is better than in the Monte Carlo simulation. This can be understood taking into account the smaller shower width in the simulation.

The photon position reconstruction of the *BABAR* calorimeter has been studied. A systematic deviation of the reconstructed from the true photon position inside the crystals was found. The size of this effect depends on the polar angle and reaches up to 10 mrad for the simulation. In data, the deviation is significantly smaller. A position correction was developed and leads to a good correlation of the reconstructed and true position. The agreement between data and simulation is significantly improved.

Minimal ionizing signals of muons can be used as a tool to study the calorimeter response on a level of single crystal rings. The studies demonstrate that the response measured with muons is not directly transferable to the response to photons. The reason for this is the different distribution of energy deposition along the longitudinal axis of the crystal together with the change of light yield along this axis. Therefore, a calibration for photons cannot be determined from the energy deposition of muons in a direct way.

Outlook

The cluster energy calibration obtained from $\mu\mu\gamma$ events, valid for large energies, is combined with the calibration using π^0 decays, which exists only for low photon energies ($E_\gamma < 1.5$ GeV). The combined energy dependent calibration factors are shown in Fig. 8.1. It should be noted that the calibration using $\pi^0 \rightarrow \gamma\gamma$

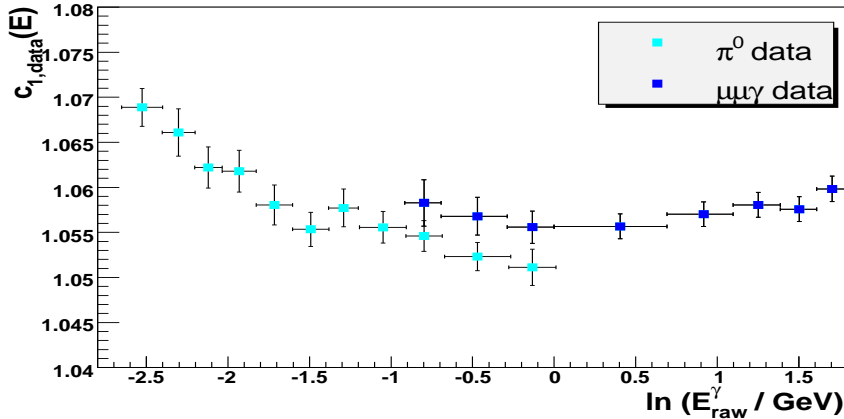


Figure 8.1: Combined energy calibration factors obtained from $\pi^0 \rightarrow \gamma\gamma$ and $e^+e^- \rightarrow \mu^+\mu^-\gamma$ [34].

decays suffers at high photon energies larger systematic uncertainties than the presented calibration with kinematically constrained photons. Because of the limited resolution, the latter method is unfortunately not applicable to small photon energies.

A reaction which provides constrained photons at low energies is the decay $\Sigma \rightarrow \Lambda\gamma$ ($E_\gamma = 76.96$ MeV in c.m. system). It provides photons in a range between 50 and 400 MeV in the laboratory.

Bibliography

- [1] B. Aubert *et al.* [BABAR Collaboration], Nucl. Instrum. Meth. A **479**, 1 (2002).
- [2] J.H. Christenson, J.W. Cronin, V. Fitch, R. Turlay, Phys. Rev. Lett. **13** 138 (1964).
- [3] M. Kobayashi, T. Maskawa, *CP Violation In The Renormalizable Theory Of Weak Interaction*, Prog. Theor. Phys. **49** 652 (1973).
- [4] P.F. Harrison, H.R. Quinn, *The BABAR Physics Book – Physics at an Asymmetric B Factory*, SLAC-R-504 (1998).
- [5] B. Aubert *et al.* [BABAR Collaboration], *Measurements of the $B \rightarrow X/s$ gamma branching fraction and photon spectrum from a sum of exclusive final states*, arXiv:hep-ex/0508004. (2005)
- [6] D. Boutigny *et al.* [BABAR Collaboration]: *The BABAR Technical Design Report*, SLAC-R-0457 (1995)
- [7] O. Buchmueller *et al.*, *Initial State Radiation: event selection, 1C fit, IRS luminosity*, BAD 558 (2003)
- [8] M. Benayoun *et al.*, *Spectroscopy at B-factories Using hard Photon Emission*, Modern Phys Lett. A Vol 14, No 37 (1999)2605
- [9] D.H. Perkins, *Introduction to High Energy Physics* Cambridge University Press, (2000)
- [10] S. Eidelman *et al.*, Phys. Lett. Meth. B **592**, 1 (2004).
- [11] H. Wong, *Detector Physics and Physics from Detectors*, Lecture Notes (2005)
- [12] R.K. Bock, A Vasilescu, *The Particle Detectors Brief Book*, Springer Verlag, (1998)
- [13] R. Nogowski *et al.*: *Precision Studies of the J/ψ Mass in $J/\psi \rightarrow \mu^+\mu^-$ Decays*, BAD 1283 (2005)
- [14] F. James, MINUIT – Function Minimization and Error Analysis, CERN Program Library Long Writeup D506 (1994)

- [15] TauQED AWG KK2f Monte Carlo Webpage,
http://www.slac.stanford.edu/%7Eemarkhod/kk_new.html, last access Oct. 2005
- [16] S. Giani *et al.*, Geant – Detector Description and Simulation Tool, CERN Program Library Long Writeup W5013 (1994).
- [17] C. Shilling, *Low energy EMC response using $\Sigma \rightarrow \Lambda\gamma$* , presentation in the EMC calibration meeting, June 2005
- [18] S. Otto: *Untersuchungen zur Ortsrekonstruktion elektromagnetischer Schauer mit dem BaBar-Kalorimeter*, Diplomarbeit, TUD-IKTP/00-01 (2000)
- [19] W. Hulsbergen, *Decay Chain Fitting with a Kalman Filter*,
<http://www.citebase.org/cgi-bin/citations?id=oai:arXiv.org:physics/0503191>, (2005)
- [20] J.S. Wenzler, S. Willocq: *Study of the photon angular resolution in the BaBar electromagnetic calorimeter*, Master Thesis, University of Massachusetts Amherst (2004)
- [21] E. Maly: *Untersuchung neutraler π -Mesonen mit dem elektromagnetischen Kalorimeter des BaBar Detektors*, PhD Thesis (2003)
- [22] R. Seitz, *Describing Energy Deposition in CsI Crystals*, BABAR Note **294** (1996)
- [23] C.F. Bolz *et al.*, *The Heidelberg Toy Monte Carlo*, private communication (Oct. 2005)
- [24] J. Marks, *Corrected γE scale for π^0 and $\mu\mu\gamma$ data*, Presentation at the BaBar Collaboration Meeting Sept. 2005
- [25] Figures by T. Schaub, private communication (Sept. 2005)
- [26] W.R. Leo, *Techniques for Nuclear and Particle Physics Experiments*, Springer Verlag (1994)
- [27] Bronstein *et al.*, *Taschenbuch der Mathematik*, Verlag Harry Deutsch (1999)
- [28] The BaBar PID webpage, http://www.slac.stanford.edu/BFROOT/www/Physics/skims/skimDoc/release14/PID_Rel14.html#BPCMuon
last access Oct. 2005
- [29] F.Fabozzi *et al.*, *Muon Identification in the BaBar Experiment*, BAD 60 (2000)
- [30] The BaBar crystals database, http://www.slac.stanford.edu/BFROOT/www/Detector/Calorimeter/crystal_dbase/uniformity/
last access Oct. 2005

- [31] G. Gratta *et al.*, *Calorimeters in Particle Physics*, Ann. Rev. Nucl. Part. Sci. 44 (1994) 453.
- [32] R. Müller Pfefferkorn, *Die Kalibration des elektromagnetischen CsI(Tl) Kalorimeters des BaBar Detektors mit Ereignissen der Bhabha-Streuung*, diploma thesis (2001)
- [33] J. Ritchie, *Muon Peaks in the EMC*, presentation in the EMC calibration meeting, Nov. 2004
- [34] J. Marks, private communication, Oct. 2005

Appendix A

Detailed Selection Criteria

Muon Pre-Selection

In order to be preselected as a event with muons, the requirements for the *BPC Muon* tag bit have to be fulfilled. A detailed description of this very loose muon selection can be found in [28]. The selection rate on all events is 5.05%.

Track Quality

A well measured track fulfills the *BABAR Good Tracks Loose* list. In detail, that means:

1. Minimum transverse momentum of 0.1 GeV,
2. at least 12 hits in the drift chamber and
3. pass within 10 cm of the beam spot in z and 1.5 cm in x-y.

Muon Selection

A well reconstructed muon fulfills the requirement of the *BABAR Mu Very Loose* list. In detail, that means [29]:

1. The calorimeter energy is $E_{cal} < 0.5$ GeV,
2. the number of IFR hit layers $N_L > 2$
3. the difference between the number of expected interaction length to the number of number of traversed interaction lengths, $\Delta\lambda > 2.5$,
4. the number of traversed interaction lengths $\lambda > 2$,
5. the continuity of the track in the IFR, $T_c > 0.1$,
6. the average multiplicity of hit strips per layer, $\bar{m} < 10$ and
7. its standard deviation $\sigma_m < 6$.

Appendix B

Distributions to Measure the Angular Resolution

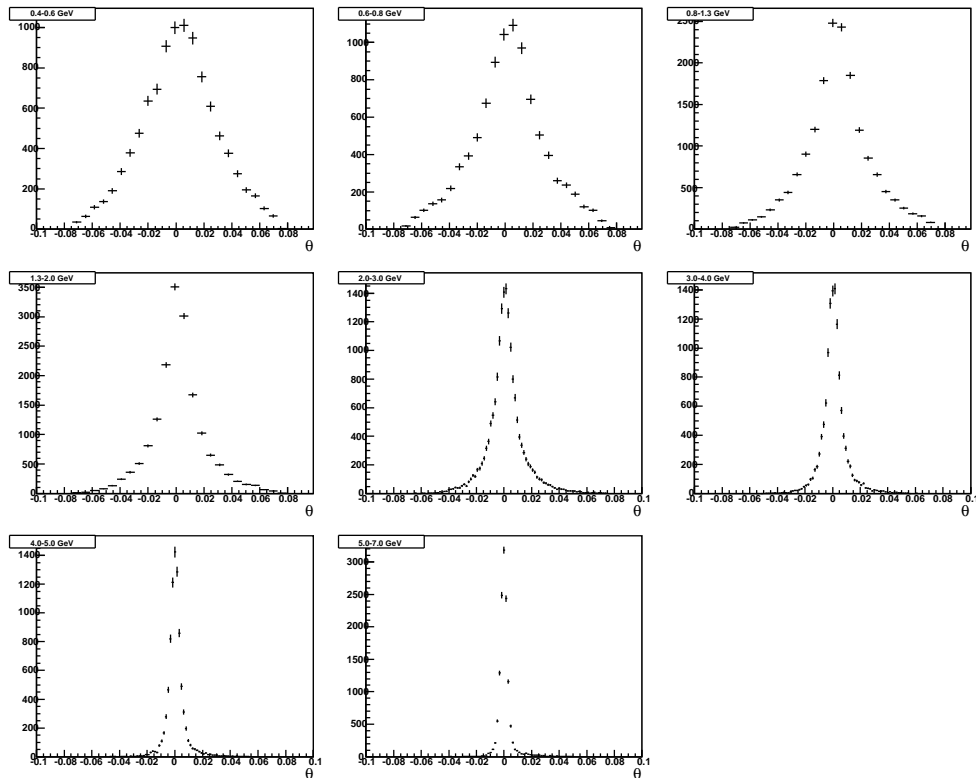


Figure B.1: *Data: Distribution of $\theta_{r,f}$ of the reconstructed minus the fitted angle in bins of the energy. The shape of the distribution can be approximated to be Gaussian.*

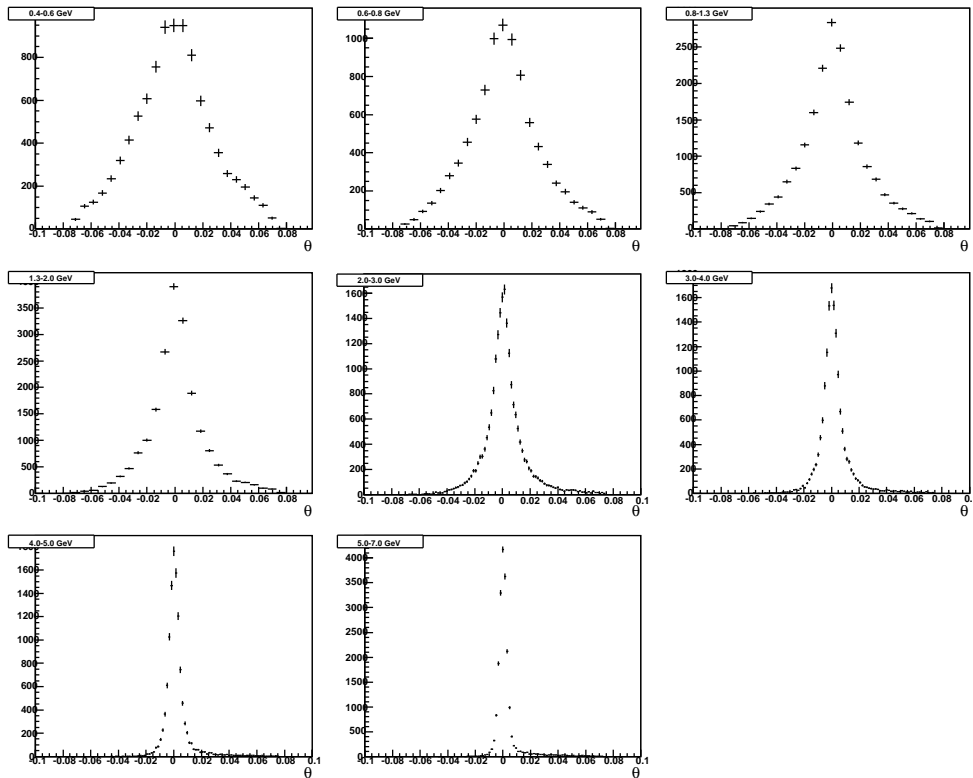


Figure B.2: $\mu\mu\gamma$ Simulation: Distribution of θ_{rf} of the reconstructed minus the fitted angle in bins of the energy. The shape of the distribution can be approximated to be Gaussian.

Appendix C

χ^2 Distributions

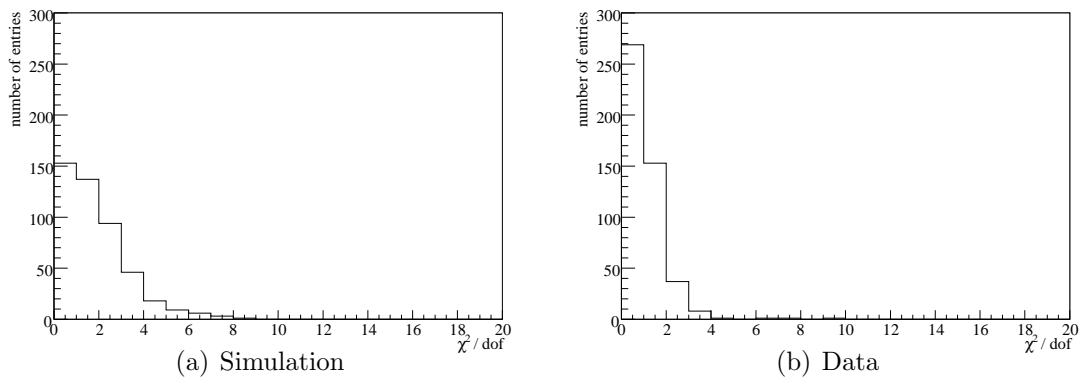


Figure C.1: *Fit quality of the 560 fits to determine the relative position (as shown as an example in Fig. 6.11) for simulation and data: In the ideal case, the χ^2 / dof should have a peak at one.*

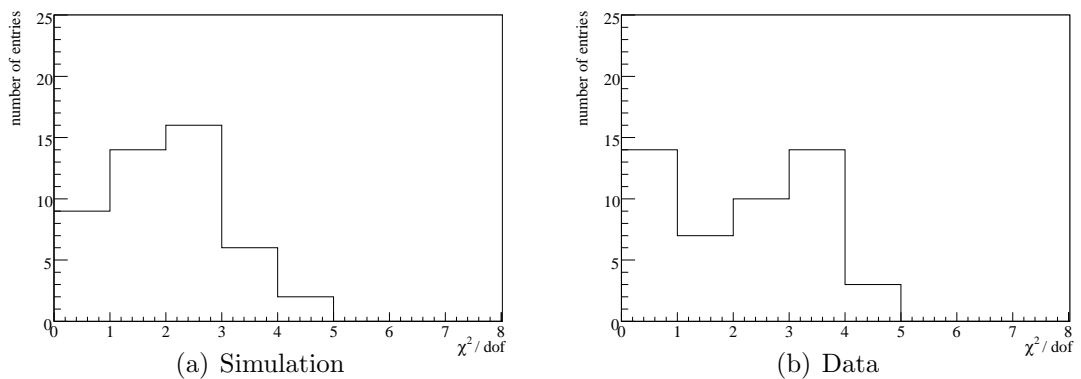


Figure C.2: *Fit quality for the 47 fits as discussed for Fig. 6.12: In the ideal case, the χ^2 / dof should have a peak at one. In the simulation, the fit describes the data slightly better than in data.*

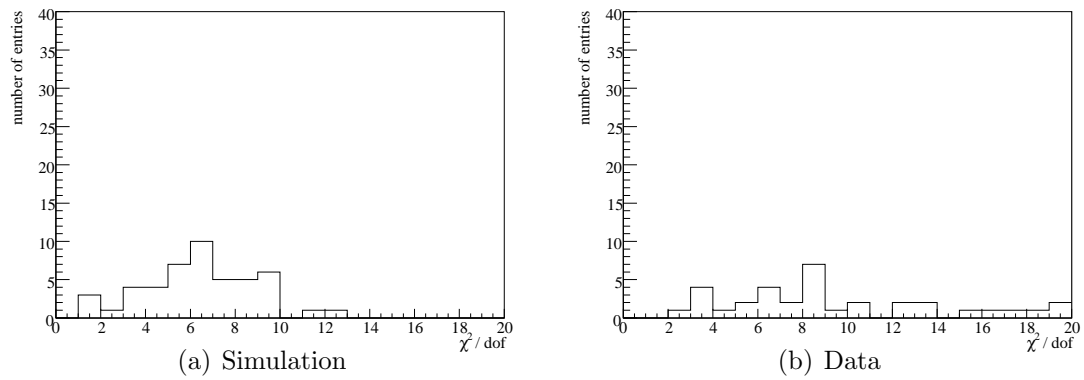


Figure C.3: *Fit quality for the 47 fits as discussed for Fig. 6.15: In the simulation, the fit describes the data reasonably well whereas in data, the fitting function does not describe the measured values properly.*

Appendix D

Crystal Light Yield

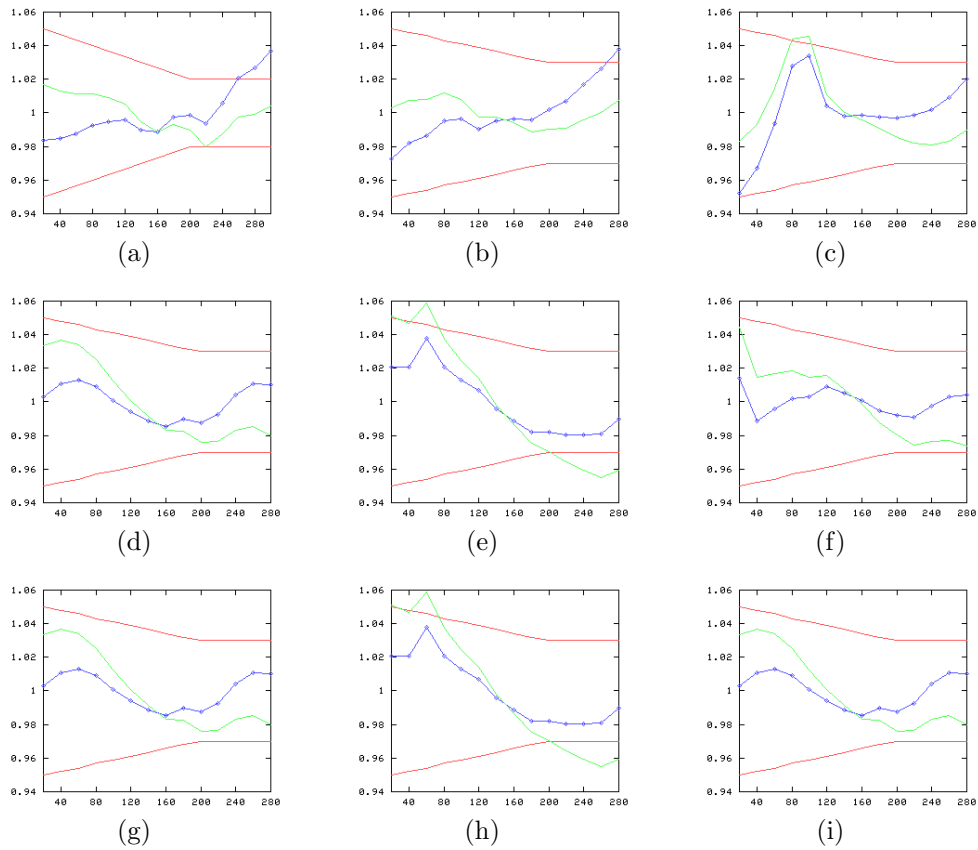


Figure D.1: *Relative light yield before assembly of the EMC for nine randomly chosen crystals. The front face is at the right hand side of each figure. The lines drawn in red are the design limitations on the uniformity, the points are measurements with a radioactive source scan [30].*

Erklärung

Ich versichere, dass ich diese Arbeit selbständig verfaßt und keine anderen als die angegebenen Quellen und Hilfsmittel benutzt habe.

Heidelberg, den 31. Oktober 2005

-
